Constraining the Petrogenesis of the Quaternary Topaz Rhyolite Lava Domes in the Bimodal Blackfoot Volcanic Field, Southeastern Idaho

By

William K. Lochridge

A thesis
submitted in partial fulfillment
of the requirements for the degree of
Masters of Science in the Department of Geosciences
Idaho State University
November, 2016

In presenting this thesis in partial fulfillment of the requirements for an advanced degree from Idaho State University, I agree that the Library shall make it freely available for inspection. I further state that permission for extensive copying of my thesis for scholarly purposes may be granted by the Dean of Graduate Studies, Dean of my academic division, or by the University Librarian. It is understood that any copying or publication of this thesis for financial gain shall not be allowed without my written permission.

Signature _____

Date _____

To the Graduate Faculty:

The members of the committee appointed to examine the thesis of William K. Lochridge find it satisfactory and recommend that it be accepted.

_____

Michael McCurry
Major advisor

_____

Shannon Kobs-Nawotniak
Committee member

_____

René Rodriguez
Graduate Faculty Representative

ACKNOWLEDGEMENTS

I would like to thank my advisors and committee members Dr. Mike McCurry, Dr. Shannon Kobs-Nawotniak, and Dr. Rene Rodriguez. Each in their own way provided much needed advice, assistance, and knowledge in researching and writing this thesis.
I would also acknowledge Paul, Dave, Carrie, and other professors in the department who showed me other ways of looking at geology instead of through a microscope or geochemical diagram. From field trips, cross-sections, basin analysis, and GIS-prepared maps, I have discovered that geology is a wide and varied profession that is worth exploring.

Other people deserving of mention are the graduate and undergraduate students, past and present in the department. To all the graduate students in geology and other departments, thank you for listening to me vent my problems, letting me learn new things in different disciplines, and hanging out in the field and here in Pocatello. I have enjoyed being a laboratory instructor, teaching undergraduate students different aspects of geology for the first time.

I would also like to acknowledge the staff in the Department of Geosciences and other departments and administrative offices at Idaho State University. Without them, my travel grants and teacher assistant salary would not have been given to me in a timely fashion. Funding for this research and travel to conferences and meetings was provided by the Graduate School of Idaho State University, the Geological Society of America, the American Geophysical Union, the National Science Foundation via the California Institute of Technology, and Dr. Wendy Bohrson of Central Washington University.

I would like to thank my family, near and far, putting up with storing parts of my life in their homes and crashing there when appropriate. And lastly, I wish to acknowledge my parents, Bill and Tina, who encouraged my lifelong desire to expand and improve my understanding of the world around me.

TABLE OF CONTENTS

List of Figures vi
List of Tables ix
Abstract x
Chapter 1: Introduction 1
1.1: Problem Statement 1
1.2: Regional Geologic Setting 2
1.3: Blackfoot Volcanic Field Geologic Setting 3
1.4: Previous Work in the Blackfoot Volcanic Field 4
Chapter 2: Methods 14
2.1: Sample Selection and Preparation 14
2.2: Petrographic Methods 14
2.3: Thermodynamic Modeling 15
2.3.1: Rhyolite-MELTS Methods and Uncertainties 15
2.3.2: Magma Chamber Simulator Methods and Uncertainties 18
Chapter 3: Results 24
3.1: Field Petrography 24
3.2: Thin Section Petrography 25
3.2.1: Phenocryst Mineral Phases and Textures 26
3.2.2: Thin Section Point Counting 32
3.3: Thermodynamic Modeling 40
3.3.1: ESRP bimodal volcanic analyses 40
3.3.2: BVF bimodal volcanic analyses 50
Chapter 4: Discussion 63
4.1: Petrographic Paragenetic Interpretation 63
4.2: Rhyolite-MELTS Modeling to Determine Crystallization Sequences and Timing of COM-Cedar Butte Trend 69
4.3: Magma Chamber Simulator Modeling to Determine Crystallization Sequences and Timing of Bimodal BVF 73
4.4: Conceptual Model of the China Hat Magma System 75
Chapter 5: Conclusions 80
References 85
Appendix 1: Data from previous workers that relates to current work 92
Appendix 2: Summary of rhyolite-MELTS model simulations of the synthetic trachybasalt composition 93
Appendix 3: Summary of Magma Chamber Simulator and rhyolite-METLS model simulations of the BVF basalts 98

FIGURES

Figure 1: Regional map of southeastern Idaho with an inset of the BVF 5
Figure 2: Map of western United States with geologic provinces and locations of topaz rhyolites 6
Figure 3: Cross-section of ESRP and southeast Idaho 8
Figure 4: Cross-section of BVF with possible location of magma reservoir 9
Figure 5: TAS diagram illustrating the similarity of whole-rock major element chemistry between the mafic and felsic rocks of the BVF and coeval ESRP 10
Figure 6: Variation chart of Nd- vs. Sr-isotopic ratios with fields of SRP rhyolites and basalts and BVF rhyolites 11
Figure 7: Simple one-stage mixing models using isotope ratios of the most primitive basalt of the SRP and crustal xenoliths from the SRP 12
Figure 8: Summary of heat flow data in the BVF and surrounding lava fields 13
Figure 9: Magmatic phenocryst cargo explanation and textures 16
Figure 10: Diagrammatic cartoon of a magma reservoir for rhyolite-MELTS 19
Figure 11: Diagrammatic cartoon of a magma reservoir for MCS 23
Figure 12: Map of sample locations on the China Hat lava dome field 27
Figure 13: Euhedral sanidine phenocryst 28
Figure 14: Embayed plagioclase mantled by embayed sanidine 28
Figure 15: Euhedral sanidine phenocryst with embayment 29
Figure 16: Extremely embayed sanidine phenocryst 29
Figure 17: Euhedral quartz phenocryst 29
Figure 18: Glomerocryst of granophyric quartz and sanidine with biotite and plagioclase 33
Figure 19: Strongly embayed quartz phenocryst 34
Figure 20: Embayed quartz phenocryst 34
Figure 21: Euhedral plagioclase phenocryst with twinning 34
Figure 22: Euhedral plagioclase phenocryst with thinning out twinning 35
Figure 23: Sanidine and plagioclase glomerocryst 35
Figure 24: Euhedral plagioclase mantled by embayed sanidine with hornblende and plagioclase 35
Figure 25: Glomerocryst of plagioclase and hornblende 36
Figure 26: Glomerocryst of plagioclase in felsic magmatic enclave with spongy cellular texture 36
Figure 27: Euhedral hornblende with internal embayment 36
Figure 28: Euhedral biotite with zircon 37
Figure 29: Euhedral magnetite 37
Figure 30: Resorbed quartz antecryst in felsic magmatic enclave 37
Figure 31: Felsic magmatic enclave microlites 38
Figure 32: Felsic magmatic enclave with quartz and plagioclase antecrysts 38

Figure 33: Resorbed quartz phenocryst with plagioclase microlites 38
Figure 34: Sanidine phenocryst with resorbed surfaces with microlites 39
Figure 35: Mafic magmatic enclave with olivine and plagioclase xenocrysts 39
Figure 36: Mafic magmatic enclave with sharp boundaries 39
Figure 37: Variation diagram TAS 43
Figure 38: Variation diagram SiO2 vs. TiO2 44
Figure 39: Variation diagram SiO2 vs. Al2O3 44
Figure 40: Variation diagram SiO2 vs. FeOtot 45
Figure 41: Variation diagram SiO2 vs. MgO 45
Figure 42: Variation diagram SiO2 vs. CaO 46
Figure 43: Variation diagram SiO2 vs. Na2O 46
Figure 44: Variation diagram SiO2 vs. K2O 47
Figure 45: Variation diagram SiO2 vs. P2O5 47
Figure 46: Chart of mineral phase precipitation vs. magma temperature for synthetic trachybasalt crystallization experiments 48
Figure 47: Chart of mineral phase precipitation vs. magma temperature for synthetic trachybasalt rhyolite-MELTS simulation for equilibrium crystallization 48
Figure 48: Chart of mineral phase precipitation vs. magma temperature for synthetic trachybasalt rhyolite-MELTS simulation for fractional crystallization 49
Figure 49: QUILF projections of olivine and pyroxene compositions from synthetic trachybasalt experiments 49
Figure 50: Clinopyroxene quadrilateral diagram from rhyolite-MELTS modeling of synthetic trachybasalts 50
Figure 51: Variation diagram TAS 51
Figure 52: Variation diagram SiO2 vs. TiO2 54
Figure 53: Variation diagram SiO2 vs. Al2O3 55
Figure 54: Variation diagram SiO2 vs. FeOtot 57
Figure 55: Variation diagram SiO2 vs. MgO 58
Figure 56: Variation diagram SiO2 vs. CaO 58
Figure 57: Variation diagram SiO2 vs. Na2O 59
Figure 58: Variation diagram SiO2 vs. K2O 60
Figure 59: Variation diagram SiO2 vs. P2O5 60
Figure 60: Chart of mineral phase precipitation vs. magma temperature for MCS-rhyolite-MELTS simulations of BVF-CHDF 61
Figure 61: Chart of mineral phase precipitation vs. magma temperature for rhyolite-MELTS simulation of BVF-CHDF 62
Figure 62: Paragenetic interpretation of the phenocryst cargo of the BVF rhyolites 68
Figure 63: Density vs. depth chart of Paleozoic to Cenozoic sedimentary and volcanic rock units of the Soda Springs-China Hat graben 77
Figure 64: Cross-section A-A’ of the BVF showing structure in the Soda Springs-

China Hat Graben down to UC-LC boundary 78
Figure 65: Conceptual diagram of the China Hat magma supply system 79

TABLES

Table 1: Adjustable constraints and inputs for rhyolite-MELTS. 18
Table 2: Input parameters for rhyolite-MELTS. 18
Table 3: Initial conditions and subsystem parameters required for MCS. 21
Table 4: Input parameters for MCS. 22
Table 5: Sample locations for thin sections 25
Table 6: Enclave definitions 32
Table 7: Point counting data from thin sections of CHDF 40
Table 8: MCS simulations with magma and wallrock starting and ending parameters 51
Table 8: Densities and depths of rock units in the Soda Springs-China Hat Graben 78

Abstract

The China Hat lava dome field, a set of three coeval topaz rhyolite lava domes, erupted at 57 ka near the center of the Blackfoot Volcanic Field (BVF), SE Idaho. Bimodal volcanic rocks of BVF closely resemble coeval Quaternary rocks erupted to the north along the eastern Snake River Plain (ESRP) segment of the Yellowstone-Snake River Plain volcanic track. However rhyolites in BVF are distinguished by more crustal isotopic ratios, as well as having a more complex assemblage of phenocrysts that includes hydrous phases (biotite and hornblende), thorite, and vapor-phase topaz.

This study seeks to improve our understanding of the unique conditions of magma evolution that led to these differences via integrated field, petrographic, and numerical modeling methods. The robust phenocryst assemblages of the rhyolites have the potential for well constraining magma evolution via quantitative thermodynamic modeling, but there is currently not enough information for assessing which were in equilibrium with their glass matrix prior to eruption (autocrysts), and which may have inherited from older cycles of magmatism (antecrysts). I focus on thin sections from the three lava domes of the China Hat lava dome field (CHDF). Results indicate three populations of phenocrysts in the rhyolites of the CHDF. The first population of phenocrysts are autocrysts that are in equilibrium with the surrounding melt and euhedral or skeletal textures because of oversaturation of the melt during magma ascent. The second population are antecrysts that come from other high melt zones or border zone mush within the magma reservoir and underwent resorption events during magma transport and magma mixing that resulted in felsic magmatic enclaves in the erupted melt. The third population are xenocrysts that are from mafic compositions from magma recharge event(s) in which

olivine, plagioclase, and pyroxene underwent resorbtion and resulted in mafic magmatic enclaves in the final erupted melt.

In addition, I conduct quantitative hypothesis testing of selected mafic parental magma compositions of the ESRP and CHDF rhyolite magma systems using thermodynamic modeling to a more felsic composition similar to those of the Craters of the Moon-Cedar Butte (COM-CB) trend and the topaz rhyolites of the CHDF. Hypotheses include equilibrium and fractional crystallization of parental magmas and wallrock assimilation of felsic Archean upper crust along with fractional crystallization of parental magmas. Evaluation of phase equilibria, major element oxides, and chemical evolution pathways is included. Best fit for the China Hat magma system is further constrained by heavy isotope ratios. While the modeling does not fully follow the fractional crystallization trends of COM-CB or CHDF with respect to major oxides and mineral phase precipitation events and amounts, similar mineral phases are produced by modeling and therefore aides in the hypothesis that between 15-30% assimilation of felsic Archean upper crust along with fractional crystallization is required to produce felsic magmas from a mafic parental basalt based on the most primitive olivine tholeiite of the BVF.

Chapter 1

INTRODUCTION

1.1 Problem Statement and Objective

The purpose of this study is to constrain the petrogenesis of the Quaternary topaz rhyolite lava domes of the bimodal basalt-rhyolite Blackfoot Volcanic Field (BVF), southeastern Idaho (Fig. 1). This is done by building upon previous work on the paragenetic history of the phenocrysts found in the rhyolite and determining plausible paths of parental mafic magma evolution using new and updated versions of thermodynamic models used by previous workers (Ford, 2005 and Pickett, 2004). I will examine the possible genetic association with adjacent and coeval rhyolites of the eastern Snake River Plain (ESRP), bimodal volcanic suites of the Basin and Range, or a hybrid of both provinces (Christiansen and McCurry, 2008 and McCurry et al., 2008). The overlying, geological question is: how are rhyolites created in bimodal volcanic systems? Previous workers have hypothesized that the following can create rhyolites: extreme fractional crystallization of parental magma; fractional crystallization of parental magma with limited crustal wallrock assimilation; equilibrium crystallization of parental magma along with mixing and hybridization of olivine tholeiite basalts with the parental magma; and partial melting of crustal wallrock or crystallized magma body from intruding magma producing eruptible amounts of rhyolitic magma (Christiansen and McCurry, 2008 and McCurry et al., 2008). I test the following petrological hypotheses on the China Hat lava dome field:

1. Evolution of the topaz rhyolites from a parental basaltic melt occurred via extreme fractional crystallization. The Quaternary rhyolites of Cedar Butte on the ESRP are

similar to the topaz rhyolites of the BVF and evolved from parent basalts via fractional crystallization with little or no crustal assimilation (McCurry et al., 2008).

2. The topaz rhyolites evolved via assimilation of surrounding Archean upper crust and fractional crystallization of a parental basaltic melt. Previous work by Ford (2005) suggests that fractional crystallization from the most evolved BVF basalt with 20-35% wallrock assimilation or fractional crystallization from the most primitive BVF basalt and 30- 45% wallrock assimilation are the most plausible evolutionary paths for the rhyolites of the CHDF as determined by $^{143}Nd/^{144}Nd$ and $^{87}Sr/^{86}Sr$ isotopic ratios from the parent basalts, end-member rhyolites, and Archean upper crustal xenoliths from the ESRP (McCurry et al., 2015).
3. The topaz rhyolites evolved via an equilibrium crystallization process with magma mixing. The Quaternary rhyolites of Unnamed Butte evolved along linear patterns in the whole-rock geochemistry with associated disequilibrium phenocryst assemblages and magmatic enclaves and are similar to mafic magmatic enclaves in the CHDF rhyolites (Goldsby et al., 2015 and McCurry et al., 2008).
4. Evolution of the topaz rhyolites occurred via partial melting of a crystallized magma body or crustal wallrock surrounding an intruding magma body or crystallized magma body with the extracted melt partially or fully erupted (Colon et al., 2015).

1.2 Regional Geologic Setting

The study area is located southeast of the ESRP in the northern Basin and Range Province (Fig. 2). The Basin and Range Province is an extensional structure in the western United States that consist of normal faults with extension in the east-west or northeast-southwest direction that overprints the Wyoming Salient of the Sevier fold and

thrust belt (Dixon, 1982). The felsic Archean basement is overlain by Neoproterzoic to Mesozoic quartzites and carbonates (Royse et al., 1975 and Rudnick and Gao, 2003).

Recent volcanism in the Basin and Range Province began in the Oligocene with subduction slab-sourced calc-alkaline volcanism that is intermediate to felsic in composition (Christiansen and McCurry, 2008). The Basin and Range Province's most recent volcanism consists of bimodal basalt-rhyolite suites that are presumed to be sourced from mantle-derived primitive magmas that intrude into the thinned extensional crust and either erupt directly as basalts or undergo fractional crystallization and/or wallrock assimilation or partially melt surrounding crust and erupt as rhyolites in the form of lava domes or flows (Christiansen et al., 1986 and Leeman and Harry, 1993).

The ESRP is an area dominated by voluminous rhyolitic ignimbrites forming calderas and then overlain by olivine tholeiite, more evolved basalts, and rhyolite lava domes (Pierce and Morgan, 2009). The petrogenesis of the bimodal basalt-rhyolite suites in the ESRP are believed to have come from "primitive" olivine tholeiites of mantle origin that erupted or underwent fractional crystallization to produce eruptible rhyolitic compositions in a mid-crustal mafic sill that is the source of the caldera-forming ignimbrites (Christiansen and McCurry, 2008 and references cited therin) (Fig. 3).

1.3 Blackfoot Volcanic Field Geologic Setting

The BVF is located in a graben flanked/bounded by the Aspen Range to the east and the Chesterfield Range to the west (Fig. 7). The west-dipping northern-segment Bear River Range normal fault continues to the northwest into the graben just south of the China Hat dome field (CHDF) while the east-dipping western-segment Bear River Range normal fault is not expressed in the Chesterfield Range. The Paris-Willard thrust fault of

the Sevier thrust belt below in the graben (Breckenridge et al., 2003 and Oriel and Platt, 1980). Mansfield (1927) identified the valley-filling basalts and the rhyolite domes during his reconnaissance of southeastern Idaho in the early part of the 20th Century. Oriel and Platt (1980) mapped the presence of Brigham Group Neoproterozoic-Cambrian quartzites and Paleozoic limestones and quartzites to the southwest of the BVF in the Bear River Range and Mesozoic calcareous rocks to the east and northeast in the Aspen Range. Directly west of the BVF, in the Chesterfield Range, there are Paleozoic units in the south and Mesozoic units in the north with an overall cover of Tertiary Salt Lake Formation conglomerates, sandstones, and limestones (Oriel and Platt, 1980). On the edges of both the Aspen and Chesterfield Ranges travertine deposits are found from hydrothermal activity and imply a hidden heat source beneath the graben (Welhan et al., 2014).

1.4 Previous Work in the Blackfoot Volcanic Field

Mansfield (1927) performed a reconnaissance of the southeast Idaho area and identified the basalts and rhyolites of the BVF and postulated that the rhyolites and surface basalts are coeval and that there possible are rhyolitic lava flows interpolated with the surface basalt flows around the bases of the rhyolite lava domes. Fiesinger et al. (1982) analyzed the basalts of the BVF and surrounding lava fields and identified the basalts are olivine tholeiites similar in composition to the olivine tholeiite basalts of the ESRP. Dayvault et al. (1984) identified the rhyolite domes as compositionally topaz rhyolites, high in U, Th, F, Be, and Li, similar to other topaz rhyolites (Christiansen et al., 1983).

In more recent work, Heumann (1999) found nearly homogeneous geochemistry

between the three rhyolite lava domes of the CHDF similar to results described by Dayvault et al. (1984) and $^{40}Ar/^{39}Ar$ dating of bulk sanidine that resulted in dates of 57±8 ka for China Hat and North Cone and 75±6 ka for China Cap. Heumann (1999) interpreted the above data to indicate the lava domes were emplaced at different times or that sanidine phenocrysts in China Hat and North Cone formed at 57±8 ka and the sanidine phenocrysts in China Cap formed at 75±6 ka.

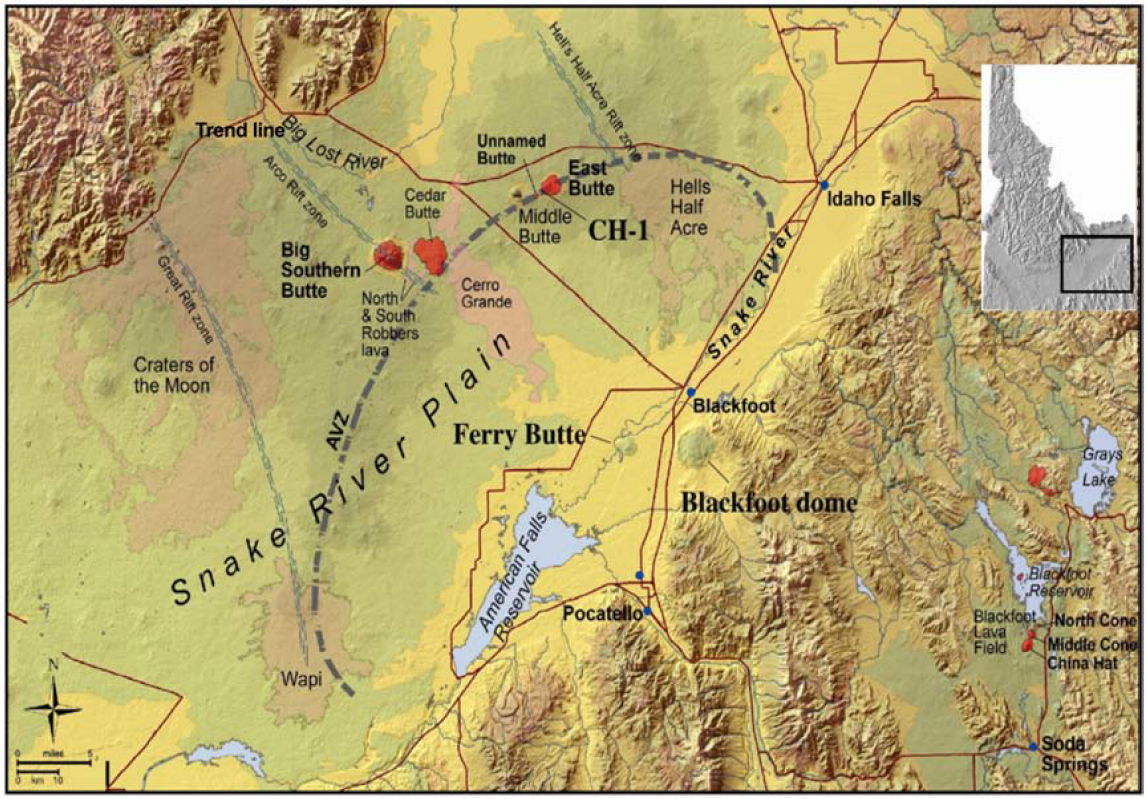

Figure 1. Regional hillshade DEM of southeast Idaho and the ESRP. Basin and Range Province is to the southeast and northwest of the ESRP. Basalt lava flows are in olive green and light brown on the ESRP and in the grabens surrounding the Blackfoot Reservoir in the lower right corner of the map. The light brown-colored basalts are the youngest Quaternary basalts on the ESRP. The red indicates the Quaternary rhyolites of the ESRP (e.g. Big Southern Butte, Cedar Butte, Unnamed Butte, and East Butte), the possible cryptodomes of the ESRP (e.g. Middle Butte, Buckskin Butte, and Ferry Butte), the BVF (China Hat, China Cap (Middle Cone), North Cone), and the North lava dome field north of the Blackfoot Reservoir. From Ganske (2006) Fig 1.

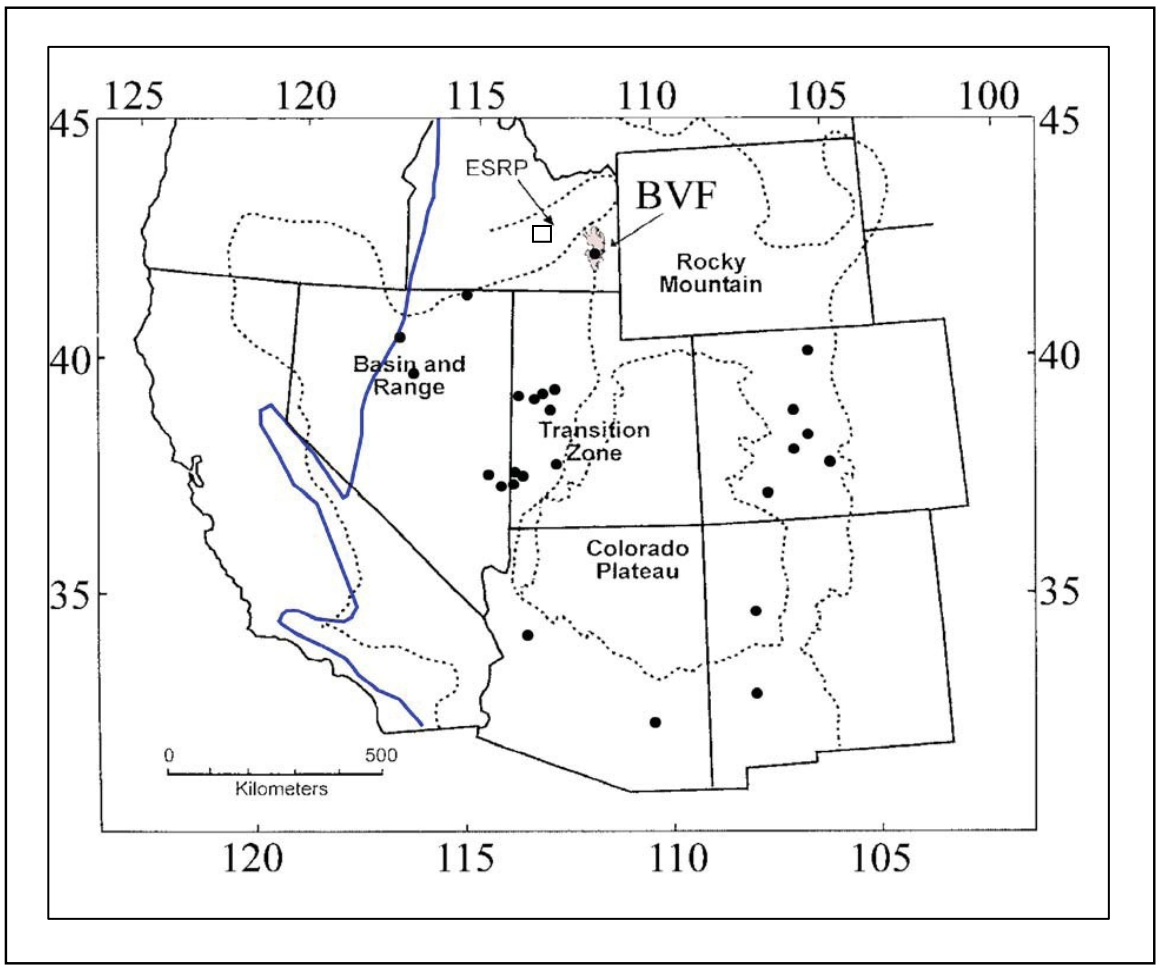

Figure 2. Map of western United States with geologic provinces identified. Black filled-in circles are the locations of topaz rhyolite lava domes and general physiographic provinces are the dotted lines. The BVF is shaded and Big Southern Butte is the open box on the ESRP. The blue line represents the 0.706 $^{87}Sr/^{86}Sr$ ratio isotopic line (inferred to separate accreted terranes from continental terranes with Proterozoic or Archean basement). Note that all the plotted topaz rhyolites are within the continental terranes. From Ford (2005) Fig. 4.

Ford (2005) hypothesized that the petrogenesis of the lava domes of the CHDF occurred along a fractional crystallization track similar to the Quaternary Craters of the Moon-Cedar Butte (COM-CB) trend in the ESRP (Fig. 5) but accommodated more crustal assimilation due to higher $^{87}Sr/^{86}Sr$ isotopic ratios (Fig. 6). Evidence presented by Ford (2005) are the near homogeneous bulk geochemistry between the three lava domes of the CHDF, the similar phenocryst textures that the lava domes, and physical features

of the domes themselves such as tephra deposits at the north base of China Hat, no evidence of interpolated basalt and rhyolite lava flows, and the same trend for the three lava domes and associated maars between China Cap and North Cone.

Dayvault et al. (1984) and Ford (2005) determined that quartz phenocrysts of the CHDF rhyolites were the most embayed, due to localized resorption during degassing and magma ascent. Textures observed in other mineral phases were not discussed by Dayvault et al. (1984), and Ford (2005) argues that the embayed textures of mineral phases other than quartz is also due to localized resorption during degassing and magma ascent.

Thermodynamic modeling of parental basaltic melt evolving into evolved basaltic and rhyolite melts using MELTS and EC-RAFC (Energy- Constrained Recharge, Assimilation and Fractional Crystallization) models of Bohrson and Spera (2003) do not adequately constrain the petrogenesis of the BVF topaz rhyolites (Fig. 7; Ford, 2005). The thermodynamic model MELTS tracks the evolution of mineral and liquid phases through various evolutionary paths but does not model high-silica rhyolite compositions due to the sensitivity of the quartz-feldspar eutectic (Ghiorso and Sack, 1995). The EC-RAFC model is a formulated set of coupled nonlinear ordinary differential equations where trace elements and radiogenic and stable isotope ratios are simultaneously modeled (Spera and Bohrson, 2001). Partial melting of wallrock, modeled as fractional melting, is incorporated along with recharge of fresh, hotter magma and fractional crystallization of existing magma as it cools using thermodynamic differential equations that calculates mass fractions and temperatures of the magma, cumulate, and wallrock variables until the desired temperature or equilibrium is reached (Bohrson and Spera, 2003). EC-RAFC

does not track mineral or liquid phase compositions and can only be used to calculate probable proportions of recharge and assimilation during fractional crystallization evolution (Bohrson and Spera, 2003).

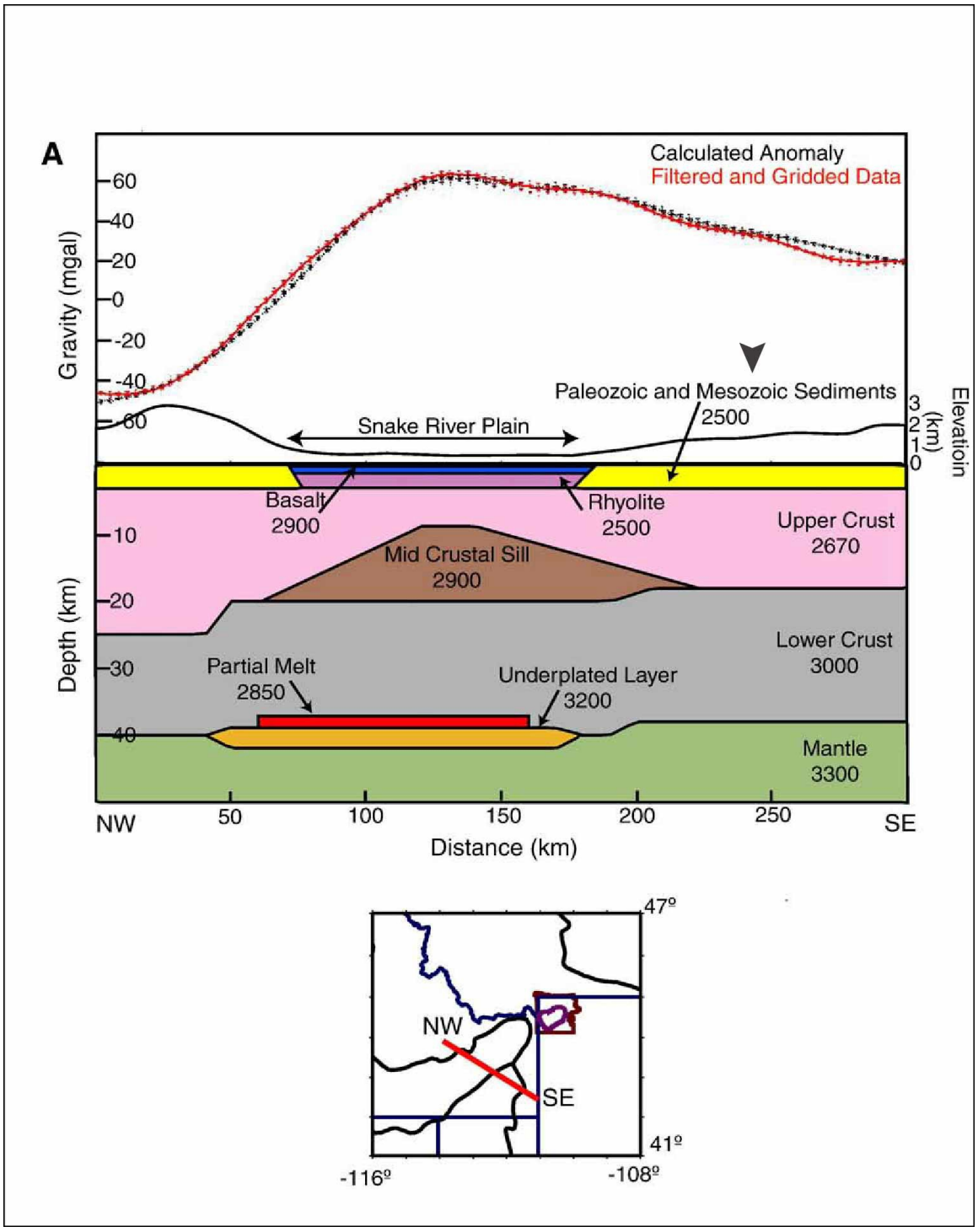

Figure 3. Cross-section of ESRP and southeast Idaho showing structure of ESRP, Mid-Crustal Sill, and Partial Melt Zone at the Moho along the red line in the inset map. Layers and densities are identified. The China Hat lava dome field is located to the east of the ESRP, its position indicated by the black arrow. From DeNosaquo et al. (2009) Fig 4.

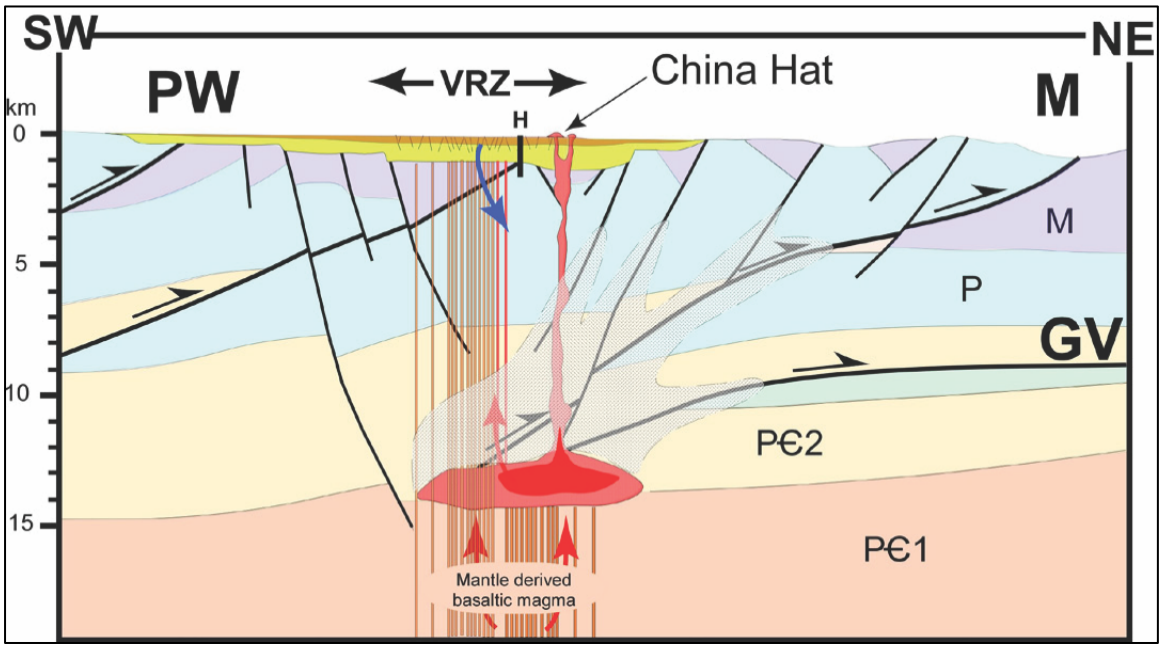

Figure 4. Cross-section of BVF showing possible location of magma reservoir, Sevier thrust faults, Basin and Range normal faults, and rift faults from dike intrusions. Shaded areas moving up from the magma reservoir are possible pathways of hot magmatic water interacting with meteoric groundwater along fault lines. This may explain why geothermal activity is found along faults and away from the CHDF. From Autenrieth et al. (2011) Fig 2.

Recent geologic and petrologic work done in the BVF area has focused on possible connections between volcanic systems and the "blind" geothermal potential of southeast Idaho (Autenrieth et al., 2011, McCurry and Welhan, 2012, McCurry et al., 2015, and Welhan et al., 2014). A deep core hole proximal to the rhyolite lava domes of the BVF (Hubbard #1) reveal a lack of geothermal heat and hydrothermal alteration in the sediments directly under the basalt lava flows in the BVF graben (Autenrieth et al., 2011; Fig. 4). Other workers interpret evidence of geothermal activity to the east and northeast of BVF that are due to deep boreholes with higher heat flow and geothermal temperature

gradients than is evident around the BVF (McCurry and Welhan, 2012, McCurry et al., 2015, and Welhan et al., 2014; Fig. 8). The lack of shallow high heat flow or other evidence of geothermal potential in the BVF may be explained by the proximity of the rhyolitic magma reservoir at the base of the thrust faults of the Sevier fold and thrust belt which directs magmatic water along thrust faults away from the magma reservoir that then interact with meteoric groundwater distally to the northeast of the BVF (Welhan et al., 2014).

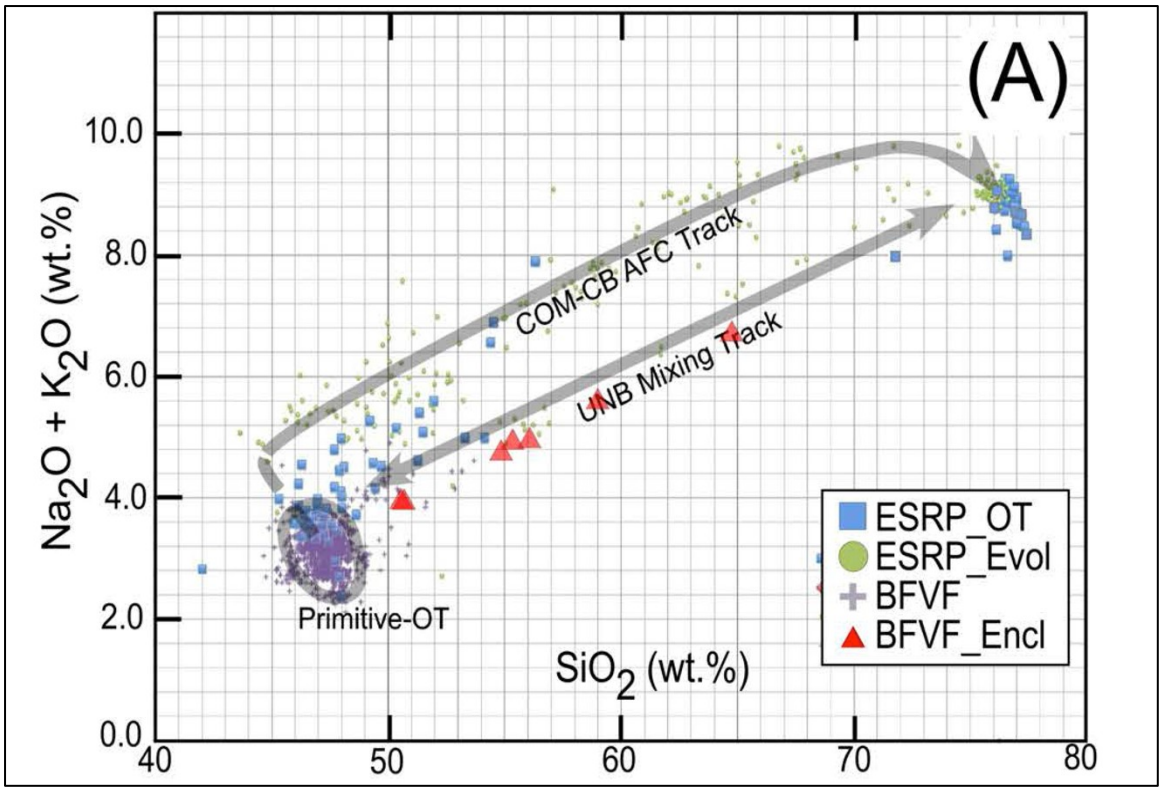

Figure 5. TAS diagram illustrating the similarity in whole-rock major element chemistry between the mafic and felsic rocks of the BVF and coeval rocks erupted on the ESRP (Christiansen and McCurry, 2008). ESRP_OT = olivine tholeiite basalt of the ESRP; ESRP_Evol = Quaternary evolved rocks of the ESRP; BFVF = Blackfoot volcanic field; BFVF_Encl = mafic enclaves from China Hat and China Cap (part of the CHDF) (Goldsby, personal communication, 2015). COM-CB AFC track and UNB mixing track are magma evolution pathways for Quaternary evolved rocks of the ESRP (McCurry et al., 2008). From McCurry et al. (2015) Fig. 6.

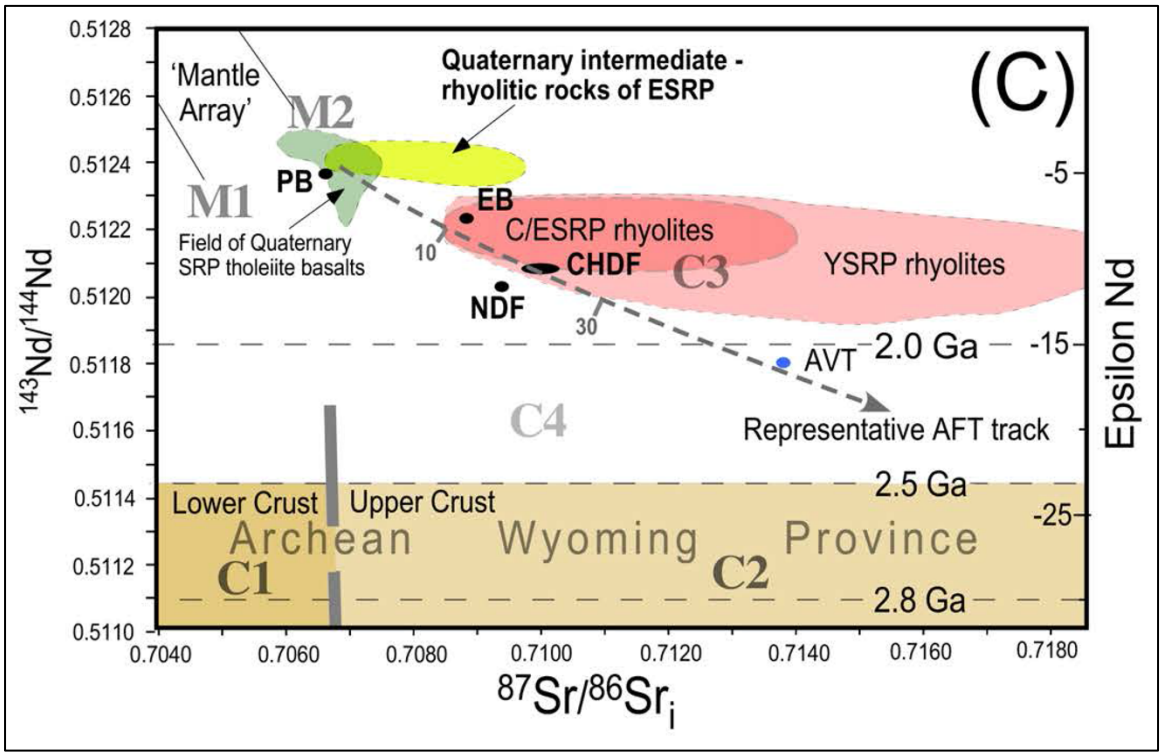

Figure 6. Variation chart of Nd- vs. Sr-isotopes showing fields for Tertiary SRP-rhyolites, Quaternary SRP-basalts and rhyolites, Quaternary BVF-basalts and rhyolites, crustal xenoliths of SRP. The dashed line represents the amount of crustal assimilation during magma evolution. For the NDF (North Dome Field) and CHDF, more than 15% upper crustal assimilation is required to achieve the requisite Sr- and Nd-isotopic ratios. From McCurry et al. (2015) Fig. 6.

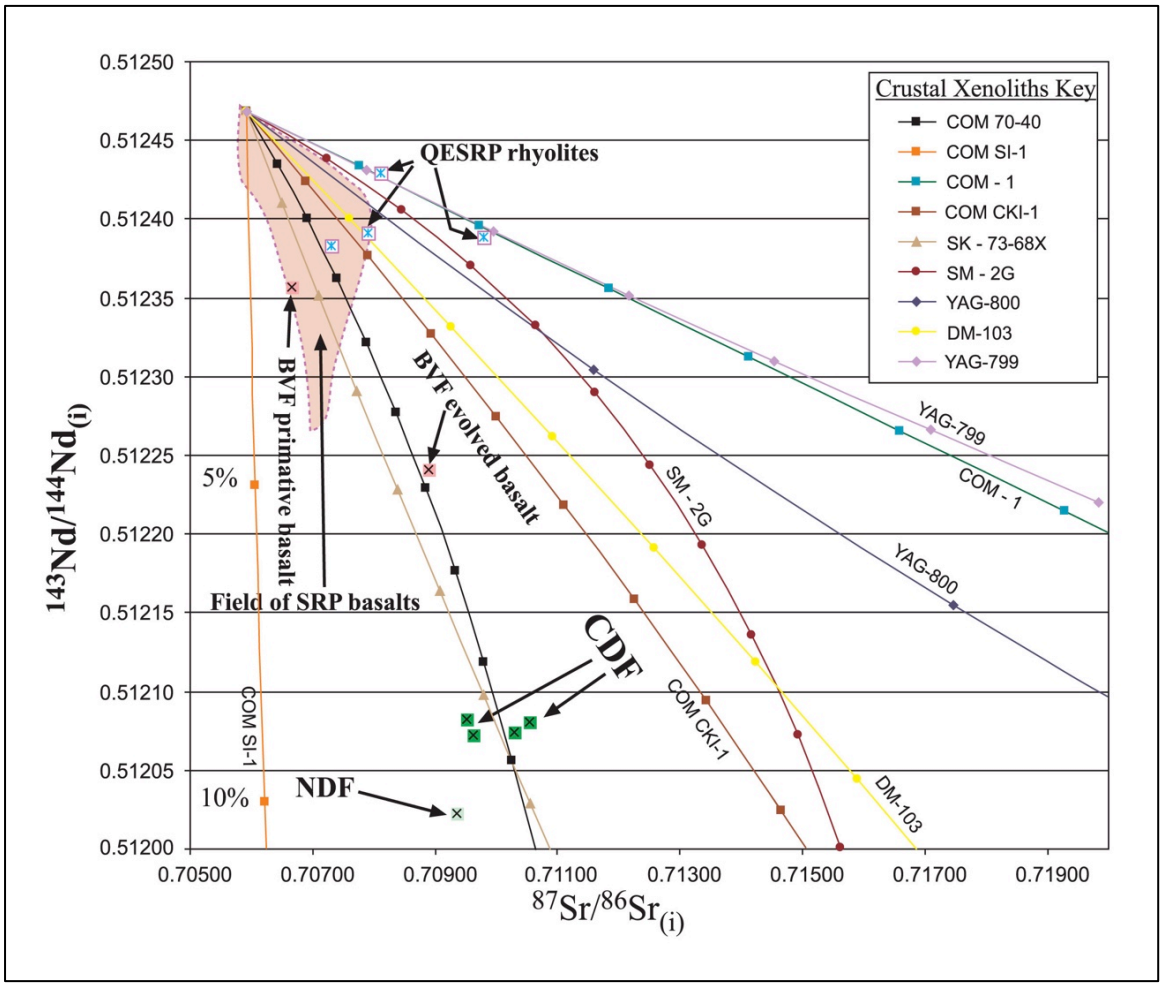

Figure 7. Simple one-stage mixing models using isotope ratios of the most primitive basalt from the SRP (Hughes et al., 2002) and crustal xenoliths from Leeman et al. (1985) (Table 1). Each tick mark represents an additional five percent bulk assimilation of crustal rocks to the hypothetical basaltic parent magma. Pickett (2004) established an isotopic and chemical link between the BVF basalts and those of the SRP. Quaternary rhyolites of the ESRP plot in or very near the SRP basalt field and contain less than five percent crustal component (McCurry et al., 1999). The CDF (CHDF) data points lie along lines represented by crustal xenoliths COM 70-40 and SK-73-68X. Between 30 and 45 percent assimilation of crustal rocks with these isotopic signatures in to the most primitive SRP basalt is required to produce the isotopic signatures of the CHDF rhyolites while only 20 to 35 percent crustal assimilation is needed if the parent magma has the isotopic composition of the most primitive BVF basalt. From Ford (2005) Fig. 6.

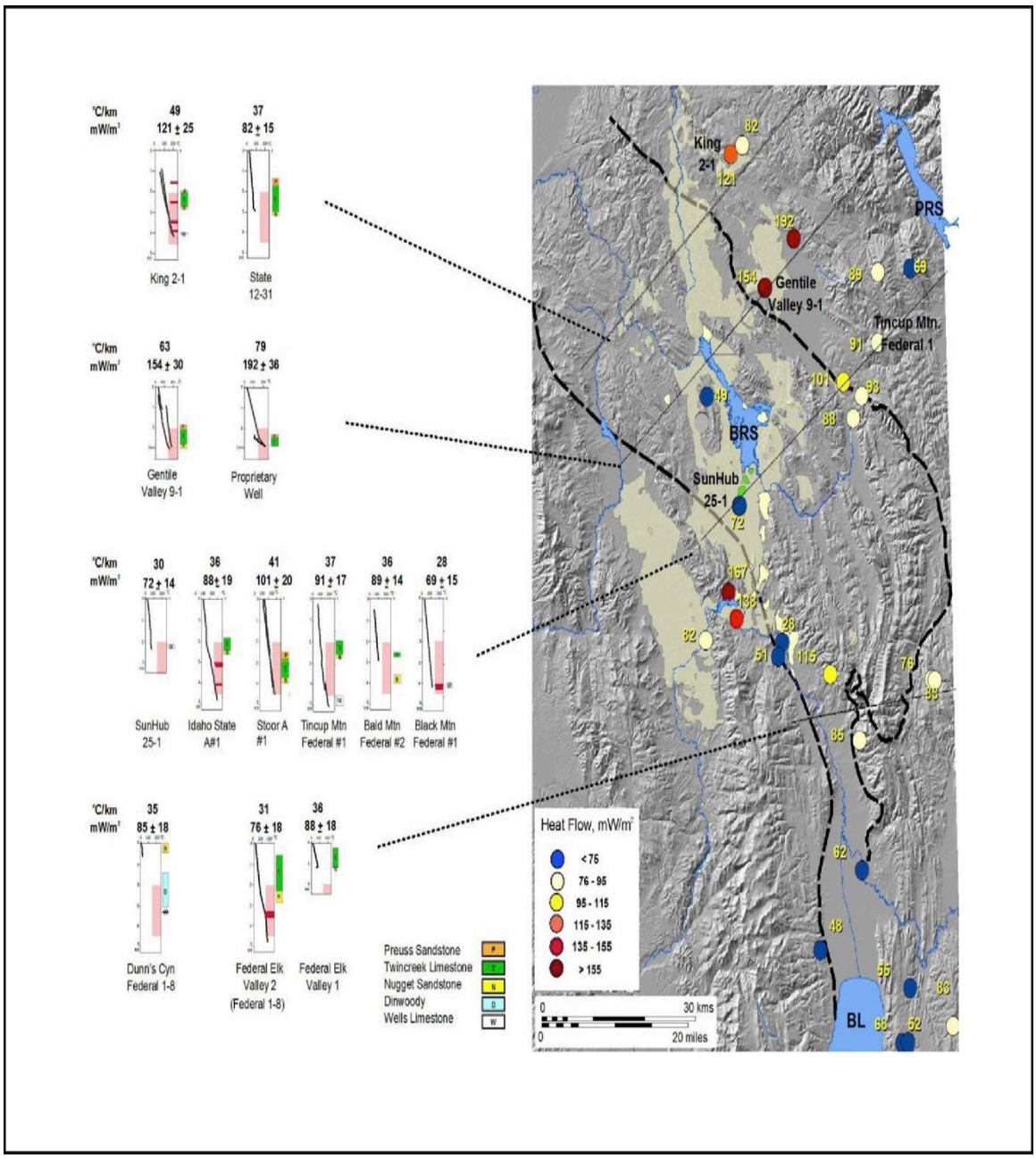

Figure 8. Summary of all heat flow data in the BVF and surrounding basalt lava fields with information of selected deep boreholes along cross sections from Dixon (1982). All thermal gradient plot scales are 0-200°C; corected thermal gradients are indicated above each plot and heat flows are shown in yellow text on the map as well as over each thermal gradient plot. BRV = Blackfoot Reservoir; BL = Bear Lake; PRS = Palisades Reservoir. Tan shaded areas are basalt lava fields; cream shaded areas are surface travertine deposits; and green shaded areas are the rhyolite lava domes of the CHDF. The dashed lines represent the Paris thrust falt (left) and the Meade thrust fault (right). From Welhan et al. (2014) Fig. 6.

Chapter 2

METHODS

2.1 Sample Selection and Preparation

Samples were selected for thin section preparation based on low levels of devitrification of the glassy groundmass and lack of mafic enclaves. Samples were broken up with a rock hammer in the field or in the rock lab on a steel plate that was prepared with dust from a crushed piece of the same or similar sample. Selected samples were broken into pieces that would fit in a rock saw and thin section blanks were cut with dimensions of approximately 46 mm by 27 mm. The thin section blanks were then heated in a convection oven at temperatures between 50°-75°C for 12 hours using standard operating procedures at the Idaho State University Laboratory for Environmental Geochemistry (ISU-LEG).

2.2 Petrographic Methods

Ten 27 mm by 46 mm blanks were prepared using standard operating procedures of the ISU-LEG and sent to Wagner Petrographic (Linden, Utah) for standard unpolished thin section preparation. Four standard thin (30 μm) sections are samples collected from China Cap lava dome (3) and China Hat lava dome tephra deposit (1). Six standard thin sections are of samples collected previously by Ford (2005) from China Hat lava dome (3) and North Cone lava dome (3) (Table 5).

Using techniques from Jerram and Martin (2008), thin sections were examined using a Nikon Eclipse E400 POL microscope with a Leica DFC290 digital camera to determine: 1) phenocryst identification; 2) comagmatic phenocryst populations; 3) textural relationships; 4) mafic and felsic magmatic enclave properties and their

relationship to the surrounding rhyolite groundmass and phenocrysts; and 5) paragenesis. Different populations of phenocrysts are identified as: 1) autocrysts that are euhedral with unzoned to zoned cores; 2) xenocrysts that are unzoned or have reaction cores that may show no overgrowths, simple overgrowths, or multiple overgrowths; 3) antecrysts that are unzoned or have reaction cores and overgrowths; and 4) microlites that represent rapid nucleation and growth of mineral phases during degassing and eruption or in the formation of magmatic enclaves during magma mixing (Jeram and Martin, 2008; Fig. 9).

Seven thin sections underwent detailed point counting using a Nikon Optiphot POL microscope with a Hacker Instruments Swift Model F point counter using standard operating procedures from the ISU-LEG (Table 7). The thin sections were point counted to 1000 counts (± 50 counts). This is to ensure a 1-3% 2σ standard deviation with regards to 1-4% relative counts for each mineral phase (Van der Plas and Tobi, 1965, Fig. 1).

2.3 Thermodynamic Modeling

Thermodynamic modeling of parent and daughter melt compositions in a variety of evolutionary scenarios was performed to construct plausible petrogenetic pathways of the evolution from a parental mafic magma to the observed topaz rhyolite composition of the lava domes of the BVF. The modeling software used are rhyolite-MELTS and the Magma Chamber Simulator (MCS).

2.3.1 Rhyolite-MELTS Methods and Uncertainties

Rhyolite-MELTS, an equilibration thermodynamic calculation program, models mineral and liquid phases with the evolution of a parental magma composition to a high-silica evolved composition through various pathways (Ghiorso and Gualda, 2015). The evolutionary paths include equilibrium crystallization, fractional crystallization,

assimilation and fractional or equilibrium crystallization, and melt extraction through

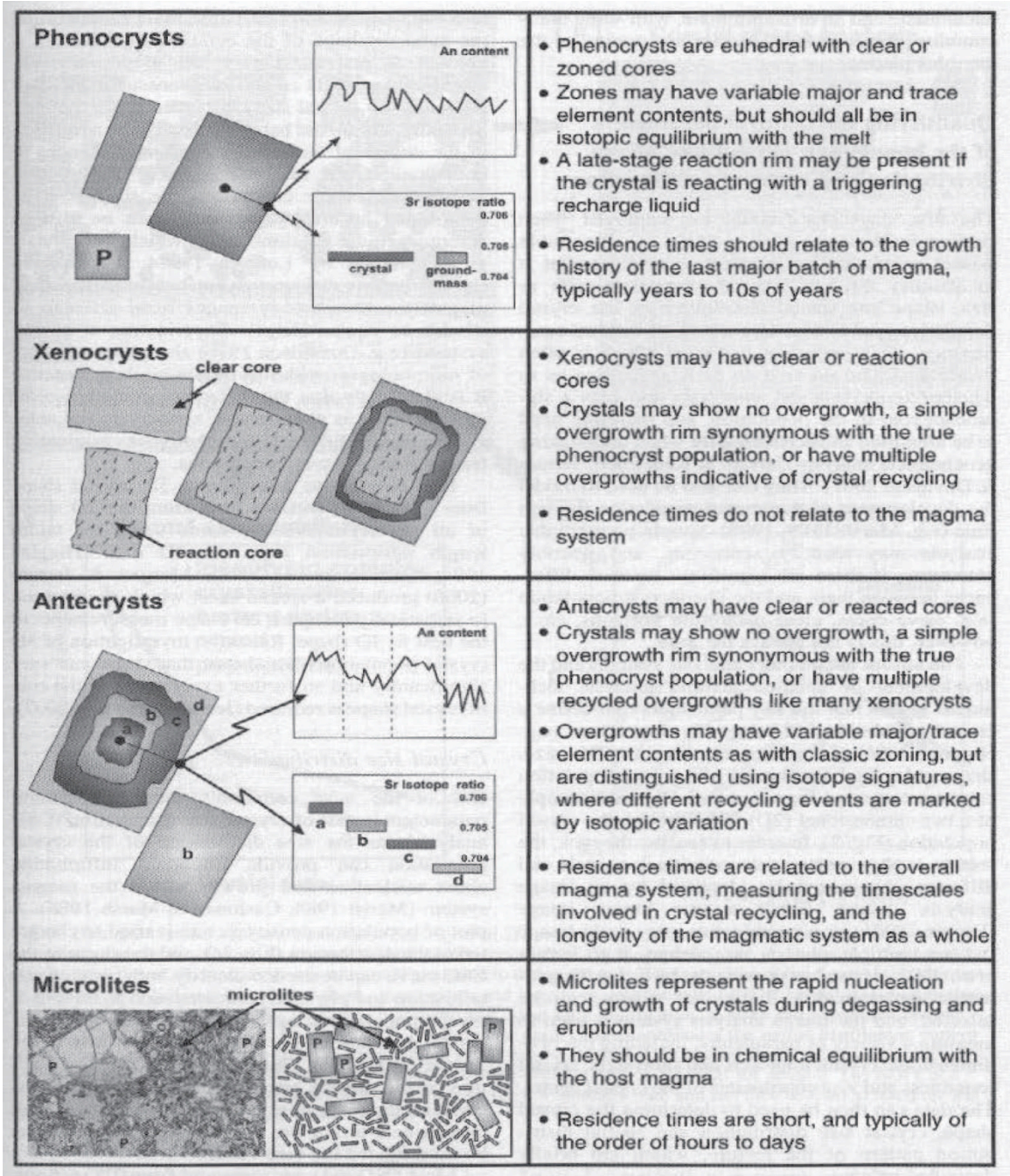

Figure 9. Magmatic phenocryst cargo with key components of crystal populations in volcanic systems. 'P' indicates phenocrysts. Phenocryst populations are divided into four groups: 1) phenocrysts or autocrysts that are in equilibrium with surrounding melt; 2) xenocrysts from other magma reservoirs or from wallrock; 3) antecrysts from other parts of the magma reservoir that are in disequilibrium with surrounding melt; and 4) microlites that form in surrounding melt during degassing and magma ascent to eruption. From Jerram and Martin (2008) Fig. 1.

partial melting of solid phases (Gualda et al., 2012). Trace elements in mineral phases and vapor phases (except H_2O and CO_2) however, cannot be modeled with the current version of rhyolite-MELTS (Ghiorso and Gualda, 2015). The current version of rhyolite-MELTS (v1.2.0) uses improved quartz and potassic-feldspar stability fields so that the program improves the calculation on the quartz + feldspar saturation surface (Ghiorso and Gualda, 2015).

I use rhyolite-MELTS in this paper is to simulate the crystallization experiments of Whitaker et al. (2008) and simulate a fractional crystallization path using the most primitive olivine tholeiite basalt of the BVF (Pickett, 2004). Whitaker et al. (2008) used the most primitive of the olivine tholeiites of the ESRP for experimental crystallization studies and used synthetic melt composition derived from the olivine tholeiite at 80% crystallization of the sample. The synthetic composition was then used to find the 80% crystallization temperature by lowering the 100% melt experiment temperature further to try to reproduce the COM-Cedar Butte trend from a basaltic composition to a high-silica rhyolitic composition with intermediate compositions also present in the trend (Whitaker et al., 2008). I use rhyolite-MELTS v. 1.2.0 for low-silica rhyolitic end-members to model the evolution of the synthetic trachybasalt composition from Whitaker et al. (2008) to determine if the model can reproduce the mineral phases seen in the experimental data.

Rhyolite-MELTS uses inputs from bulk composition in major oxides, intensive thermodynamic variables such as temperature and pressure ranges, fO_2 constraints, and model evolution pathways (Table 1) demonstrated in the cartoon of Figure 10. The system being acted upon is the bulk composition of the magma in major oxides in wt.%. Prior to executing a simulation, rhyolite-MELTS calculates the redox state (since FeO_{tot} is usually the data entered for iron-oxides), promts the user to select the evolutionary path

to execute for the simulation, and determines the liquidus temperature of the magma. The evolution paths used for model runs in this project are equilibration crystallization (default setting), fractional crystallization of solids, and fractional crystallization of liquids.

Table 1. Adjustable constraints and inputs for rhyolite-MELTS simulations used for synthetic trachybasalt composition of Whitaker et al. (2008) for COM-Cedar Butte trend analysis.

Bulk Composition	Major oxides in wt.%	SiO_2, TiO_2, Al_2O_3, FeO_{tot}, MnO, MgO, CaO, Na_2O, K_2O, P_2O_5, and H_2O
Intensive Variables	Temperature	Starting and ending temperatures and temperature increment
	Pressure	Starting and ending pressures and pressure increment
	fO_2 constraint	QFM buffer
Options	Model path	Equilibrium crystallization – default setting Fractional crystallization of solids Fractional crystallization of liquids
	Assimilant	Batch add of wallrock
	Solid phases	Olivine, clinopyroxene, orthopyroxene, amphibole, biotite, feldspar, quartz, spinel, rhombohedral-oxides, apatite, water, melt

Table 2. Input parameters for rhyolite-MELTS simulations of synthetic trachybasalt used for COM-Cedar Butte trend analysis. Bulk major oxide compositions are from Whitaker et al. (2008) and Pickett (2004). MnO is not computed for MCS and therefore is included with FeO after redox calculations are performed.

Composition	100D3	KEP-004	Composition	100D3	KEP-004
SiO_2	49.26	48.61	Pressure	4300 bars	4730 and 3900 bars
TiO_2	4.17	2.07	fO_2 constraint	QFM-2 buffer off	QFM buffer off
Al_2O_3	14.46	15.46	Magma evolution path	Fractional crystallization	Fractional crystallization
FeO_{tot}	13.31	10.82		Equilibrium crystallization	
MnO	0.23	0.18			
MgO	4.00	8.55			
CaO	8.94	10.08			
Na_2O	3.01	2.33	Mineral phases selected for both 100D3 and KEP-004	Olivine, orthopyroxene, clinopyroxene, biotite, hornblende, feldspar, quartz, rhombohedral-oxide, spinel, apatite, fluid, melt	
K_2O	1.57	1.39			
P_2O_5	1.05	0.50			
H_2O	1.80	0.50			

2.3.2 Magma Chamber Simulator Methods and Uncertainties

Magma Chamber Simulator (MCS) is a thermodynamic model that tracks the geochemical and petrological evolution of a composite system composed of a set of subsystems that include the magma body (resident magma melt ± crystals ± fluid),

cumulate reservoir, wallrock, and a set of recharge reservoirs, that is linked to the temperature evolution of hotter magma and cooler wallrock as the two approach and achieve thermal equilibrium (Bohrson et al., 2014, Figure 1). MCS incorporates mineral and liquid phase equilibria from rhyolite-MELTS which allows for the computation of internal states of equilibrium in each subsystem in parallel (Fig. 11). Any MCS solution provides a continuous record of output as a function of magma temperature that includes the composition, masses and temperatures of all relevant phases (melt + solids ± fluid) within the various subsystems (Bohrson et al., 2014).

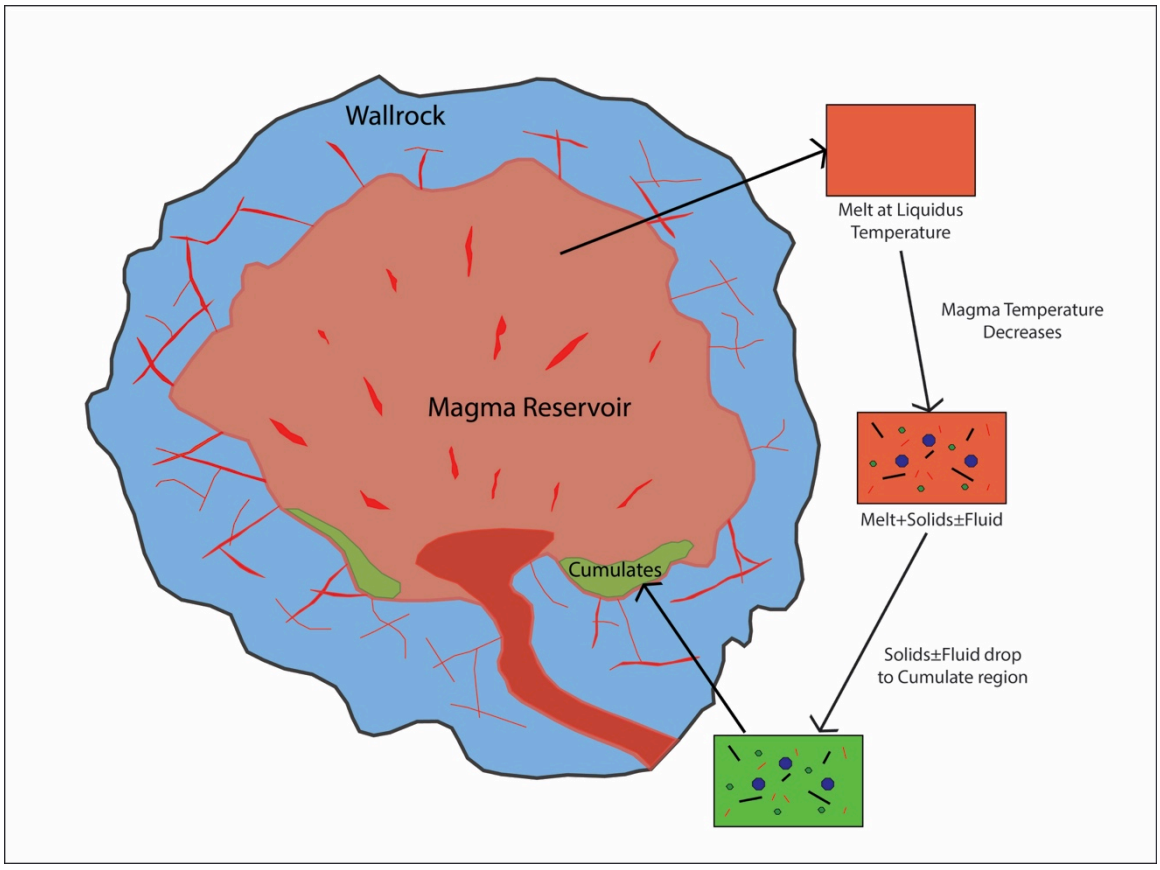

Figure 10. Diagrammatic cartoon of a magma reservoir undergoing fractional crystallization in the rhyolite-MELTS model. Melt at liquidus temperature cools and becomes oversaturated and precipitates mineral phases. These phases settle out of the melt and form cumulate layers in the reservoir. Then the model lowers temperature to repeat the process until thermodynamic quadratic equations cannot be calculated. From Spera and Bohrson (2001) Fig. 1.

The MCS subsystems uses parameters that are fixed by the model and input by the user. Table 3 lists the fixed and adjustable parameters used by MCS. Fixed parameters include magma initial mass (M^M = 100%) and fO_2 buffer (set to zero) for the magma, wallrock, and recharge subsystems. The other parameters from Table 3 are adjustable except for the ones concerning trace elements, which are not used for our MCS modeling. Wallrock initial mass (M^{WR}) can be adjusted from the default of 100% to 1000%, which is used in the ratio of wallrock mass vs. magma mass, $\Lambda = M^{WR}/M^{M}$. Λ will vary depending on what the user wants for assimilation of wallrock. The default 1:1 ratio has the entire wallrock mass equilibrate with the magma mass to a thermodynamic equilibrium and a 10:1 ratio will have the magma subsystem perform fractional crystallization only with no wallrock assimilation. Recharge initial mass (M^R) can vary from 0-100% and represents the amount of batch recharge intruded into the magma.

The bulk compositions for magma, wallrock, and recharge subsystems (X^M, X^{WR}, and X^R) that include all the major oxides (except for MnO) and H_2O are initial condition inputs by the user. Other user inputs are initial temperatures for the magma, wallrock, and recharge subsystems (used for finding liquidus temperatures of the subsystems), magma and wallrock composite system pressure, and recharge trigger temperature (magma temperature at which recharge occurs). FmZero is the amount of anatectic melt present in the wallrock before it can be transferred to the magma and is set to between 0.04 and 0.12 with a default setting of 0.08 (Borhson et al., 2014). The last parameters are wallrock preliminary start and end temperatures and magma and wallrock temperature increments. The preliminary start and end temperatures are for MCS to constrain the wallrock liquidus and solidus. The temperature increments are used by MCS in thermodynamic

calculations with smaller increments more closely simulating ideal fractional crystallization of mineral phases and larger increments simulating equilibrium crystallization (Bohrson et al., 2014).

The bulk compositions we are using for MCS and rhyolite-MELTS modeling are the most primitive of the olivine tholeiite basalts (OTB) of the BVF basalts, KEP-004 from Pickett (2004) and a synthetic trachybasalt from Whitaker et al. (2008), 100D3 (Table 4). I use the synthetic trachybasalt with rhyolite-MELTS to replicate the trend that produced 100D3 in Whitaker et al. (2008) and follows the COM-Cedar Butte trend (McCurry et al., 2008). Then, MCS and rhyolite-MELTS will be used to determine an assimilation-fractional crystallization (AFC) path for the evolution of KEP-004 to produce a Cedar Butte-trend seen in the Quaternary bimodal olivine tholeiite basalt-topaz rhyolites of the BVF.

Table 3. Initial conditions and subsystem parameters required for an MCS simulation. Major oxides in wt.% used in MCS: SiO_2, TiO_2, Al_2O_3 , Fe_2O_3, FeO, MgO, CaO, Na_2O, K_2O, P_2O_5, and H_2O. FeOtot is the bulk rock Fe-oxide and is split into Fe_2O_3 and FeO by QFM buffer from rhyolite-MELTS or calculation using a Fe^{2+}/Fe^{3+} initial ratio. MnO is combined with FeO after redox state determined. From Bohrson et al. (2014) Table 1.

Pressure, P, for composite system Ratio of initial WR mass to initial M mass, $\Lambda = M^{WR}_i / M^{M}_i$ Critical melt fraction in WR, FmZero = 0.08 (default), works from 0.04 – 0.12 (Bohrson et al., 2014) Temperature decrement to subsystem M during approach to thermal equilibrium of WR and M, ΔT M subsystem melt temperature for *j*th recharge event, T^{M}_{1}, etc. Ratio of mass of *j*th recharge event to initial mass of M, $\Phi = M^{R}_j / M^{M}_i$				
Magma body, wallrock and recharge magma subsystem input for MCS simulation:				
Subsystem	Initial bulk major oxide composition (for *i* oxide components)	Temperature	fO_2 constraint	Mass
Magma body (M)	$X^{M}_{i,j}$	Initial temperature of subsystem T^{M}_i	Buffer (e.g. QFM or Fe^{2+}/Fe^{3+} ratio)	Initial mass of subsystem (100% melt), M^{M}_i
Wallrock (WR)	$X^{WR}_{i,j}$	Initial temperature of subsystem T^{WR}_i	Buffer (e.g. QFM or Fe^{2+}/Fe^{3+} ratio)	Initial mass of subsystem, M^{WR}_i
Recharge, *j* events (R_j)	X^{R}_j	T^{R}_j	Buffer (e.g. QFM or Fe^{2+}/Fe^{3+} ratio)	Mass of *j*th recharge increment, M^{R}_j

Table 4. Input parameters used for MCS simulations of anhydrous bulk composition KEP-004 from Pickett (2004). MnO incorporated into FeO after redox calculations. fO_2 buffer used is QFM from Mg/Mn concentrations in ilmenite and magnetite (Ford, 2005).

KEP-004		Pressure				
SiO_2	48.61	4730 bars		Magma reservoir at AFUC/AMLC boundary (18.3 km) (DeNosaquo et al. 2009)		
TiO_2	2.07	3900 bars		Bottom of pressure range of magma reservoir based on hornblende geobarometry (13.65 km) (Ford, 2005)		
Al_2O_3	15.46	Wallrock Melt Fraction		0.04 to 0.12 (0.08 default value)		
FeO_{tot}	10.82	Temperature Increments		Wallrock Temperatures*		
MnO	0.18	Magma	1°C increments	4730 bars	464°C	25°C/km + 5°C surface T (18.34 km)
MgO	8.55	Wallrock	1°C increments		647°C	35°C/km + 5°C surface T
CaO	10.08	Initial Temperatures Magma	1300°C 1300°C	3900 bars	384°C	25°C/km + 5°C surface T (16.09 km)
Na_2O	2.33	$Wallrock_{Start}$** $Wallrock_{End}$**	685°C		536°C	35°C/km + 5°C surface T
K_2O	1.39	*Based on temperature gradients of 25°C/km from Brott et al. (1980) and 35°C/km from Welhan and Gwynn (2014)				
P_2O_5	0.50	** WR temperatures used to find Wallrock Solidus and melt fraction				
H_4O	0.50					

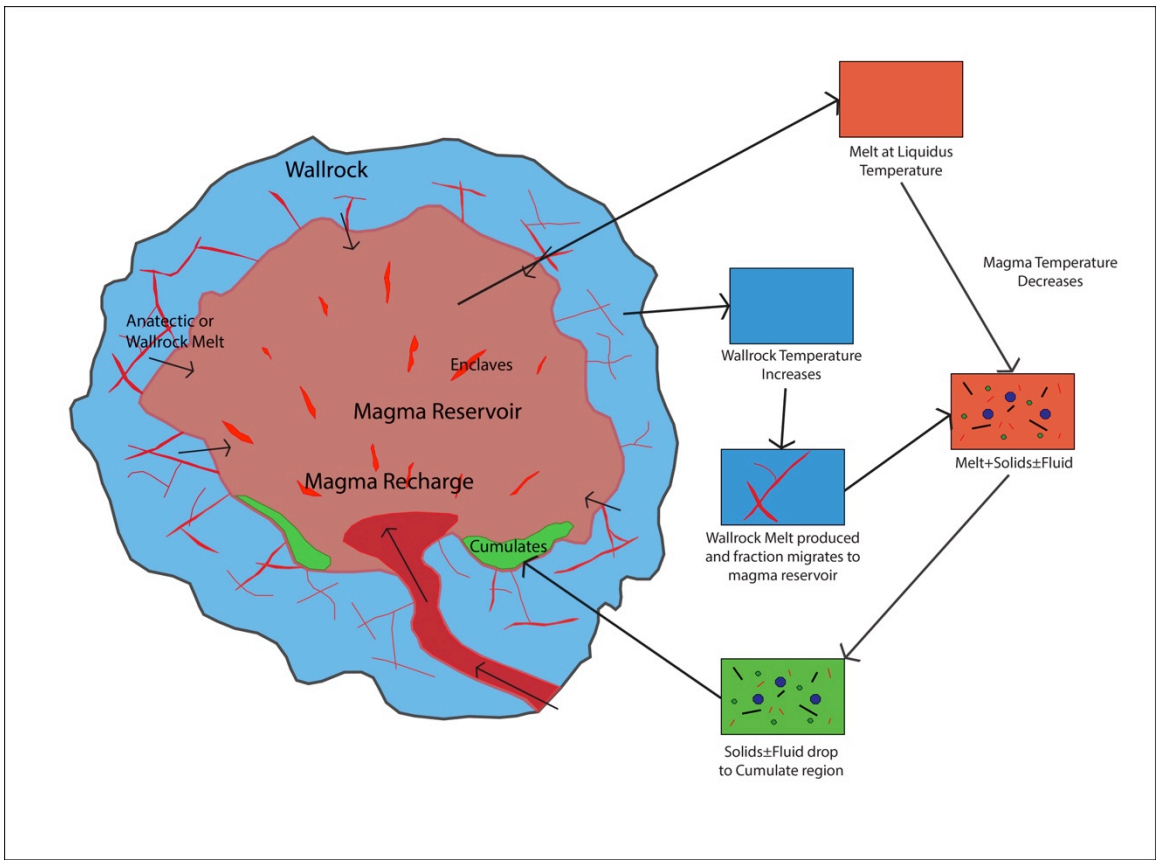

Figure 11. Diagrammatic cartoon of a magma reservoir undergoing fractional crystallization and assimilation of wallrock melt in the MCS model. Simultaneous magma melt temperature decreases with fractional crystallization occur with wallrock heating to above its solidus temperature and melt generation. Above a predefined melt threshold in the wallrock, excess melt migrates to the magma reservoir and is homogeneously mixed with the magma melt. Further fractional crystallization occurs in the new composition with all mineral phases forming cumulate layers having no further contact with the melt. From Spera and Bohrson (2001) Fig. 1.

Chapter 3

RESULTS

This chapter will discuss results from field sampling, petrology of thin sections, and thermodynamic modeling using rhyolite-MELTS and Magma Chamber Simulator. Field sampling will provide hand sample descriptions of the samples collected. Petrology will provide descriptions of phenocrysts and the surrounding matrix of thin sections from field samples and select samples from Ford (2005). Thermodynamic modeling will describe the simulations run on the synthetic trachybasalt composition of Whitaker et al. (2008) and on the most primitive olivine tholeiite basalt of the BVF (Pickett, 2004).

3.1 Field Sampling

Samples collected and used are from the China Hat lava dome field (CHDF). The samples collected from China Cap are from the northwest and northeast quadrants and on southern exposures at the top and below the crest, 2/3 the distance from the top (Fig. 12, green dots). Other samples used were from those used in Ford (2005), collected from China Hat and North Cone lava domes of the CHDF (Table 5 and Fig. 12). All samples except for WKLCH1-15 and 8220104 are from the glassy carapaces of China Hat, China Cap, and North Cone lava domes. Sample WKLCH1-15 is a devitrified sample from the tephra quarry on the north side of China Hat lava dome. Sample 8220104 is from North Cone lava dome in the collapsed section of the dome but also has a glassy matrix.

The samples with glassy matrix are leucocratic and light gray in color and contain approximately 8-10% phenocrysts which include in order of abundance quartz > sanidine > plagioclase > hornblende ≈ biotite >> magnetite ≈ ilmenite. Quartz phenocrysts are colorless and dipyramidal in shape (alpha-quartz) with the largest quartz phenocrysts up

to 1 mm in size. Sanidine phenocrysts are grayish to tannish white in tabular crystal shapes up to 1 mm in size. Some sanidine phenocrysts are observed to have exsolution lamellae (wavy lines that are shaded slightly differently than the rest of the crystal face). Plagioclase phenocrysts are usually white or grayish to colorless with equant crystal shapes up to 1 mm in size. Twinning is observed on some plagioclase phenocrysts with straight parallel lines. Hornblende phenocrysts are elongate tabular shapes up to 1 mm in length and are black in color. Biotite phenocrysts are shiny black to brownish black in color and are observed as hexagonal sheets that are up to 1 mm in size. Magnetite phenocrysts are equant in shape and black in color and are < 0.5 mm in size.

Table 5. List of sample sites with GPS coordinates referenced to Figure 12.

Sample	Latitude	Longitude	Location
WKLCC1-14	42.828500	-111.592370	China Cap
WKLCC8-14	42.830130	-111.596760	China Cap
WKLCC9-14	42.830120	-111.596660	China Cap
WKLCH1-15	42.814924	-111.603982	China Hat quarry
7160103	42.810098	-111.609511	China Hat
7210103	42.802235	-111.608186	China Hat
7210104	42.801433	-111.606429	China Hat
8220101	42.835497	-111.579268	North Cone
8220103	42.832009	-111.581670	North Cone
8220104	42.837769	-111.573416	North Cone

The devitrified sample (CH1-15) from the tephra deposits on the northern side of the China Hat lava dome is mesocratic, dark gray, and has larger observeable crystals than the other glassy samples. The crystalline matrix is hexagonal in shape with crystals between 1-2 mm in size that are dark gray. Quartz phenocrysts are hard to pick out of the glassy matrix. The only distinguishing characteristics of the quartz phenocrysts from the devitrified matrix are the dipyramidal shape of the phenocrysts and the phenocrysts are colorless instead of dark gray.

3.2 Thin Section Petrography

The following are summaries of observations made in ten standard thin sections from China Hat, China Cap, and North Cone were analyzed using a petrographic microscope (Table 5). Seven standard thin sections were point counted to 1000 ± 50 counts to determine mineral phase percentage using a petrographic microscope and point counter (Table 7).

3.2.1 Phenocryst Mineral Phases and Textures

Textural nomenclature fin this section follows from Vernon (1997) and Jerram and Martin (2008). The major mineral phases observed in thin section include quartz, > plagioclase > sanidine > biotite ≈ hornblende > Fe-Ti oxides (magnetite > ilmenite) and comprise ~ 9% phenocrysts in the rock (Table 7). Accessory phases include zircon > apatite. Ford (2005) observed thorite and allanite, but only in trace amounts in heavy mineral separates and were not observed in my thin sections. Microlites are sparse in the glassy matrix and include plagioclase > hornblende > Fe-Ti oxides > zircon > apatite. No microlites were observed in the devitrified China Hat thin section.

Sanidine phenocrysts are either euhedral or subhedral in shape. Euhedral sanidine phenocrysts are observed as isolated crystals or mantling euhedral or subhedral plagioclase phenocrysts (Figs. 13 and 14). Subhedral sanidine phenocrysts have embayments, crystals mantling rounded corners, or are boxy cellular (Figs. 13, 15, and 16). Sanidine phenocrysts can be identified by their higher birefringence (δ = 0.008, white color) than that of plagioclase (δ = 0.006-0.007, grayish-white color).

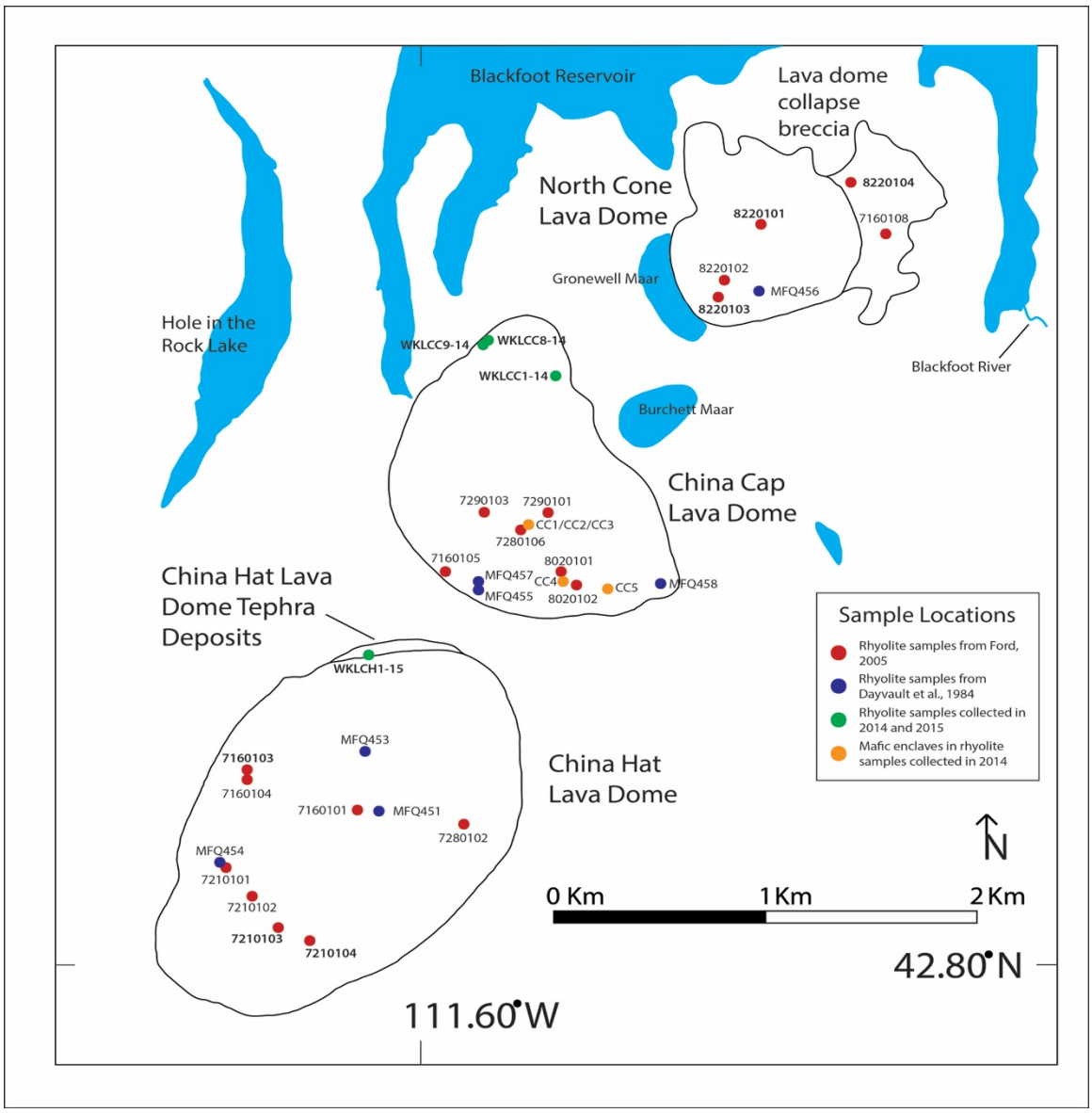

Figure 12. Map of sample locations on the rhyolite lava domes of the China Hat lava dome field. Samples in red are from Ford (2005). Samples in blue are from Dayvault et al. (1984). Sample collected by author are in green and orange. Samples used in this paper are WKLCC1-14, WKLCC8-14, WKLCC9-14. WKLCH1-15, 8220101, 8220103, 8220104, 7160103, 7210103, and 7210104 (in bold). From Ford (2005) Plate 1.

Quartz phenocrysts are either euhedral or subhedral in shape. The euhedral quartz phenocrysts are observed as isolated crystals or in glomerocrysts with plagioclase ± other mineral phases (Figs. 17 and 18). Subhedral phenocrysts have embayments, rounded corners, or are boxy cellular in shape similar to sanidine phenocrysts (Figs. 19 and 20).

Quartz phenocrysts are identified by their crystal shape and by their birefringence (δ = 0.009, yellowish-white color).

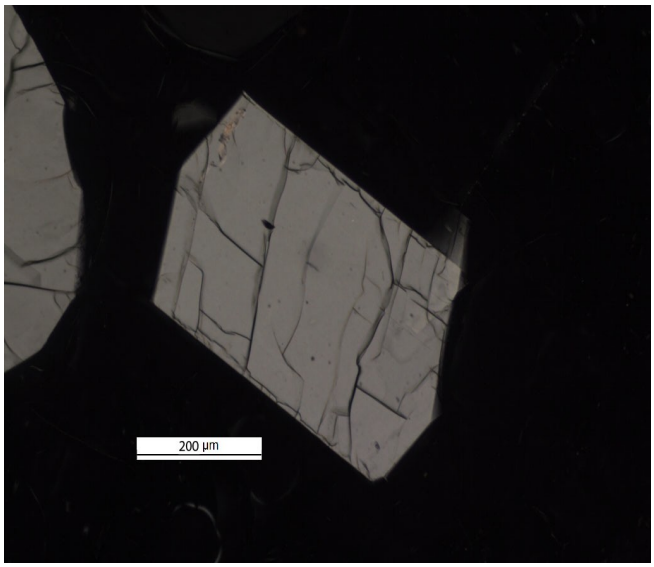

Figure 13.
Euhedral sanidine next to embayed quartz. 10x magnification, cross-polarized light.

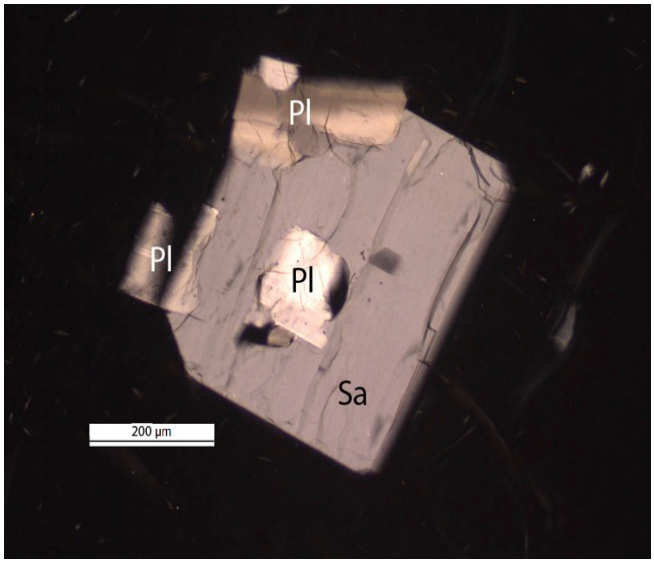

Figure 14.
Embayed plagioclase mantled by embayed sanidine. The sanidine has plagioclase growth from the embayments. 10x magnification, cross-polarized light.

Plagioclase phenocrysts are euhedral or subhedral in shape. Euhedral plagioclase phenocrysts are isolated crystals, mantled by sanidine, or are in glomerocrysts with other plagioclase phenocrysts ± other mineral phases (quartz, hornblende, biotite, and accessory phases) (Figs. 21, 22, 23, and 24). Subhedral phenocrysts are also mantled by sanidine phenocrysts or are in glomerocrysts (Figs. 23 and 25) and are only found in such groupings and not alone in the matrix.

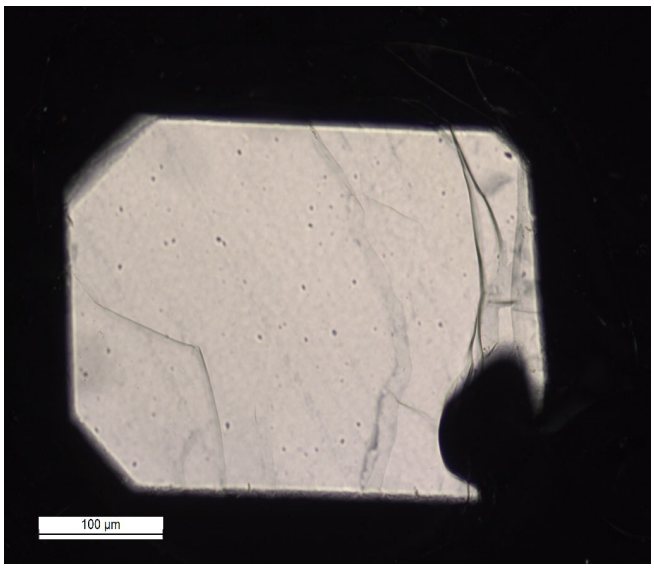

Figure 15.
Euhedral sanidine with embayment on one corner. 20x magnification, cross-polarized light.

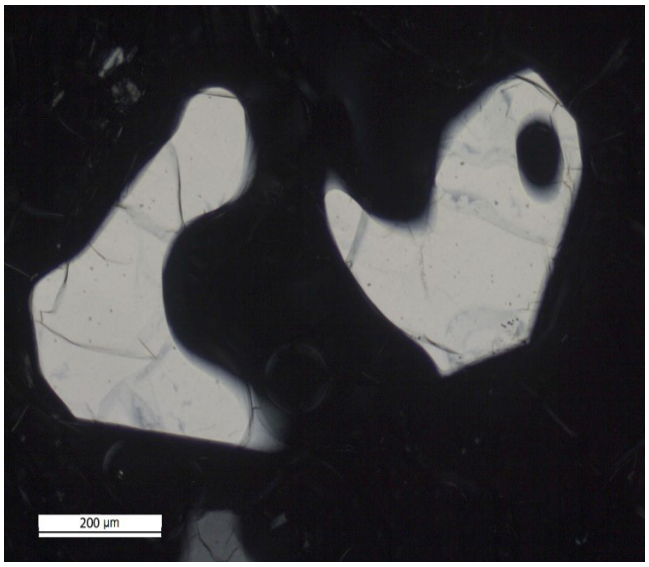

Figure 16.
Extremely embayed sanidine that has is in separate sections in thin section that are in the same crystallographic orientation. 10x magnification, cross-polarized light.

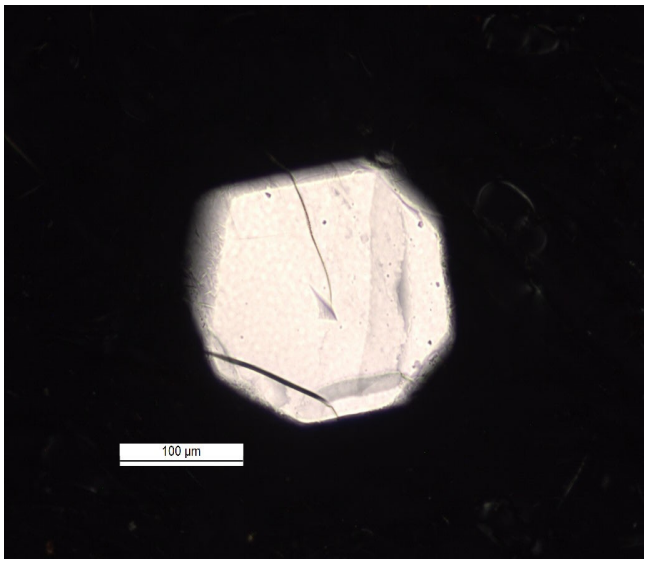

Figure 17.
Euhedral quartz phenocryst. 20x magnification, cross-polarized light.

Plagioclase phenocrysts are also found with spongy cellular textures in glomerocrysts (Fig. 26). These spongy cellular phenocrysts are only found in glomerocrysts that are in magmatic enclaves. Plagioclase phenocrysts are usually distinguished from sanidine phenocrysts by albite twinning, chemical zoning, and birefringence (δ = 0.006- 0.007, grayish-white color instead of δ = 0.008, white color). Plagioclase is also found as one of the microlite mineral phases. Plagioclase microlites are elongate or acicular in shape and are white to grayish-white in color with some showing twinning on the long axis.

Hornblende phenocrysts are euhedral to subhedral in shape. Euhedral phenocrysts can be isolated crystals or in glomerocrysts with plagioclase and other mineral phases (Figs. 25 and 27). Subhedral phenocrysts are found as isolated crystals or in glomerocrysts (Fig. 24). Hornblende is distinguished by their brown to greenish-brown color in plain polarized light, their birefringence in cross-polarized light, and by the 60°-120° cleavage (Fig. 25). Mafic microlites are identified as hornblende based on their elongated shape and lower birefringence than biotite.

Biotite phenocrysts are euhedral and subhedral in shape. Euhedral phenocrysts are isolated crystals (Fig. 28). Subhedral phenocrysts are isolated crystals or in glomerocrysts with plagioclase and other mineral phases (Fig. 18). Inclusions of zircon and apatite are observed in some biotite phenocrysts (Fig. 28).

Opaque minerals are also observed in thin section. Based on their usually boxy shape, they are mostly identified as magnetite (Fig. 29). Ilmenite is also identified in thin section if seen on edge (platy appearance) or as wedge-shaped phenocrysts in the glassy matrix.

Major mineral phases plagioclase ≈ quartz ≈ sanidine are observed within the felsic magmatic enclaves (FME) as defined from Ganske (2006) (Table 6). Accessory mineral phases include zircon > apatite. Microlites in the FME matrix include plagioclase >> hornblende > Fe-Ti oxides > zircon are abundant in the FMEs. Plagioclase phenocrysts are observed in glomerocrysts with albite twinning (Fig. 26). The innermost plagioclase of Figure 26 shows a spongy cellular texture.

Quartz phenocrysts show evidence of felty textures with rounded corners and micro-embayments (Fig. 30). Microlites of plagioclase and hornblende are observed as densely packed masses with no obvious orientation surrounding larger phenocrysts (Fig. 31). FMEs are observed as three different types: compact clusters of phenocrysts and microlites with sharply defined boundaries with surrounding matrix; compact clusters of phenocrysts and microlites with phenocrysts extending beyond the FME and FME microlites thinning out into the surrounding matrix; and loosely compacted FMEs where the FME microlites are slightly denser than the surrounding matrix and the FMEs appear to be stretched along flow banding in the surrounding matrix (Figs. 32 and 33).

Major mineral phases plagioclase > olivine and minor pyroxene are observed within the mafic magmatic enclaves (MME) as defined from Ganske (2006) (Table 6). Some olivine phenocrysts have biotite reaction rims. Microlites in the MME groundmass include plagioclase > hornblende. Phenocrysts in MMEs are usually found as glomerocrysts of plagioclase and olivine (Fig. 34) surrounded by plagioclase and mafic microlites. Microlites in MMEs are smaller than those in FMEs and have a higher mafic content with the birefringence colors of MME groundmass are 1 to 2 orders of magnitude brighter than FME groundmass birefringence. MME microlites are more closely packed

together than FME microlites and there are less observable vesicles in MME groundmass. The boundaries of MMEs are observed as three types: the first is a sharp boundary (Fig. 35); the second shows gradational zoning with surrounding melt with microlite population varies from densely packed plagioclase and hornblende to sparse plagioclase ± hornblende in the surrounding glassy matrix; and the third boundary is diffuse with MME groundmass observed to be broken up and dispersed into the surrounding groundmass (Fig. 36).

Table 6. Enclave classification based on their nature and main petrographic features. Mafic magmatic enclaves (MME) and cumulate enclaves and felsic microgranular enclaves (FME for both categories) are used in this paper. From Ganske (2006) Table 2.

Term	Nature	Contact	Shape	Ovoid
Xenoliths Enclave	Piece of country rock	Sharp	Angular	Contact-metamorphic texture and minerals
Xenocrysts Enclave	Isolated foreign crystal	Sharp	Globular	Corrosion reactional aureole
Mafic Magmatic Enclave (MME)	Blob of coeval magma	Mostly sharp	Ovoid or Ellipsoid	Fine-grained igneous texture (But not always microgranular)
Cumulate Enclave (Autolith)	Disrupted cumulate	Mostly gradual	Ovoid	Large-grained cumulate texture
Felsic Microgranular Enclave	Disrupted fine-grain margin	Sharp or granular	Ovoid or Ellipsoid	Fine-grained igneous texture
Composite Enclaves	Enclave with-in a magmatic enclaves characterized by the type of enclave that is contained in the host (See above characteristics)			

3.2.2 Thin Section Point Counting

Seven thin sections were point counted to 1000 counts each, except for WKLCC1-14 and WKLCC8-14 at 1050 and 950 counts respectively (Table 7). Quartz, sanidine, and plagioclase phenocrysts were counted as euhedral or subhedral crystals. Hornblende, biotite, magnetite, and accessory minerals were counted as separate bins.

Ilmenite is identified in thin section but is not plentiful enough to count separately. Magnetite is identified by equant octahedral shape with either straight or rounded edges, which is more readily identifiable than ilmenite or other opaque mineral phases. Hornblende and biotite are identified as only by mineral phase and not as separate euhedral or subhedral textures. Accessory phases are identified in section 3.2.1 and while counts of these mineral phases are plentiful in some thin sections, their volume are restricted to the points counted and thus their numbers are not counted in the totals for each thin section or averages in Table 7.

The phenocryst cargo of all the thin sections point counted averages 8.90±1.76%. Quartz is the most common mineral phase averaging 3.83±1.11%. Other phenocrysts in order of declining average percentage are plagioclase (2.31±0.40%), sanidine (2.22±0.70%), biotite (0.13±0.11%), hornblende (0.12±0.20%), and opaque mineral phases (0.31±0.23%).

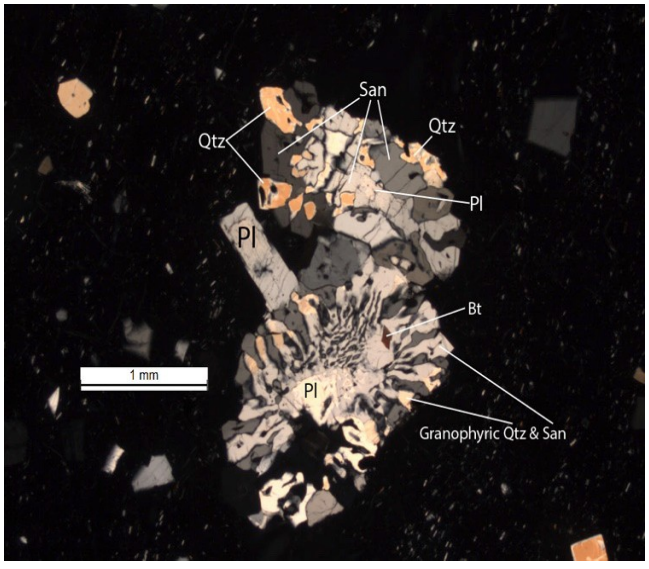

Figure 18.
Glomerocryst consisting of two plagioclase crystals mantled by sanidine with granophyric intergrowths of quartz. Another plagioclase phenocryst is attached to the lower mantled grouping.
Biotite is an inclusion in sanidine in the lower mantled grouping. 2x magnification, cross-polarized light.

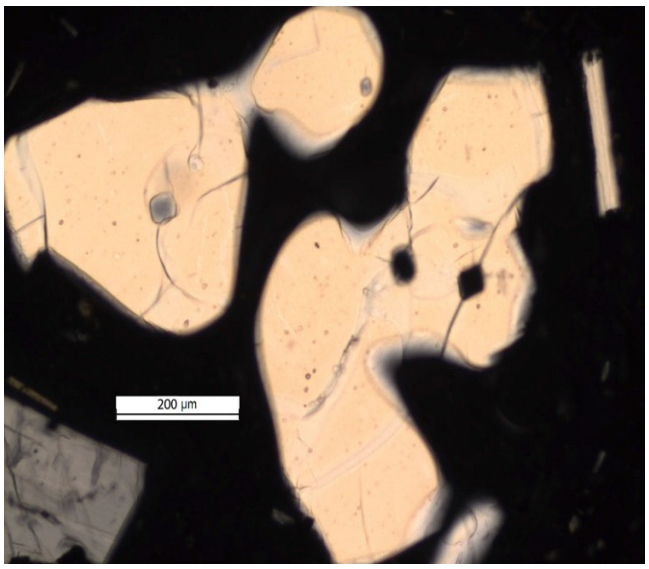

Figure 19.
Strongly embayed quartz that has separate sections that are in the same crystallographic orientation. 10x magnitude, cross-polarized light.

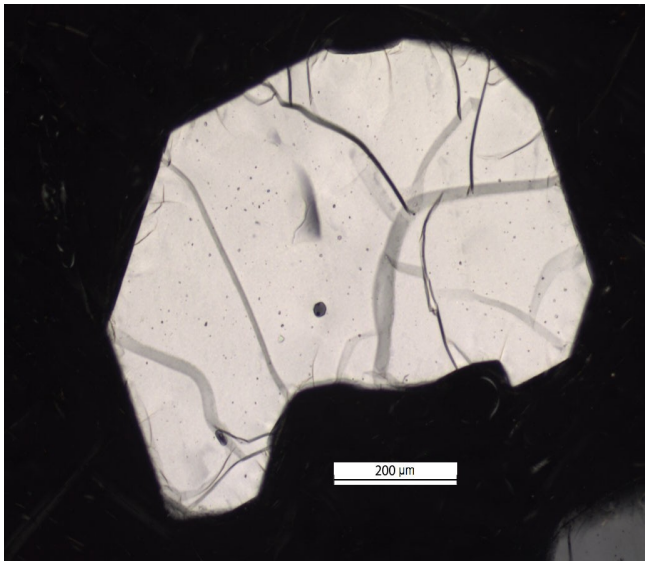

Figure 20.
Embayed quartz phenocryst with embayments at the top and bottom of the crystal, as it is orientated in the thin section. 10x magnification, cross-polarized light.

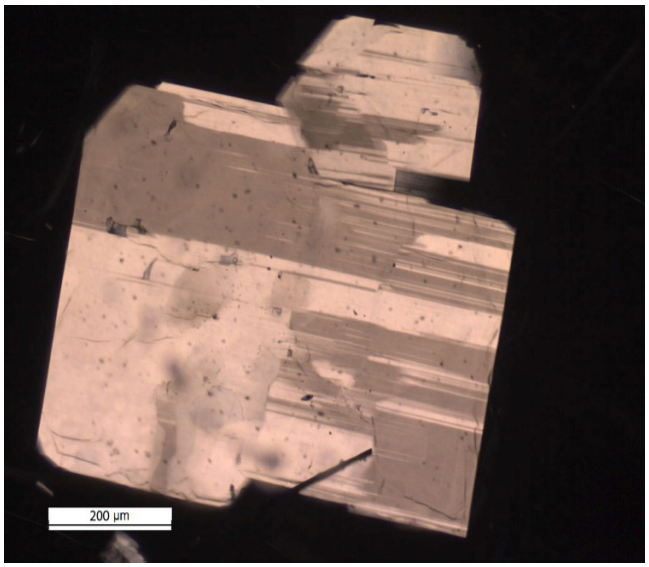

Figure 21.
Euhedral plagioclase with separate growth events with twinning occurring before and after growth. 10x magnification, cross-polarized light.

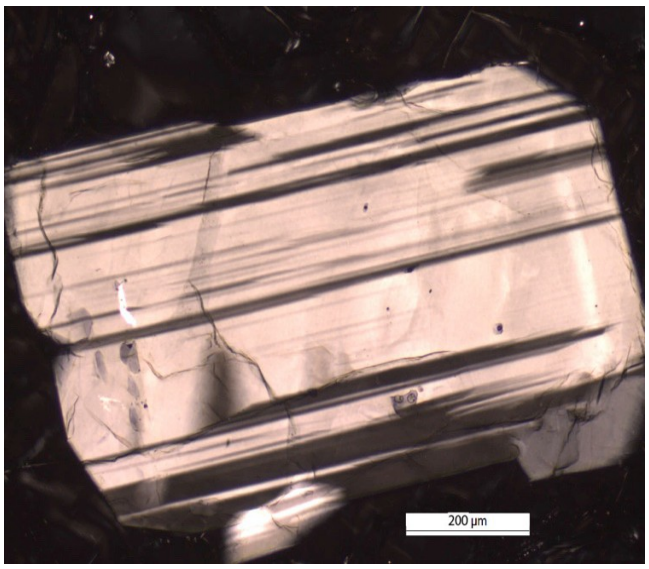

Figure 22.
Euhedral plagioclase with perthitic twinning. 10x magnification, cross-polarized light.

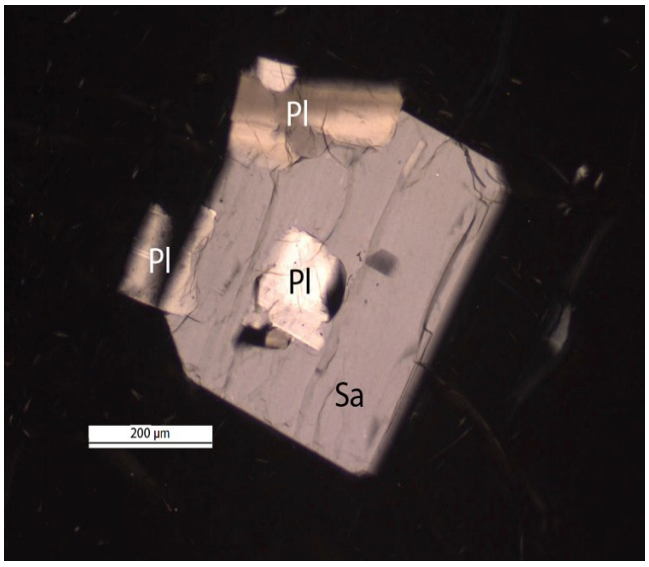

Figure 23.
Embayed plagioclase mantled by embayed sanidine. The sanidine has plagioclase growth from the embayments. 10x magnification, cross-polarized light.

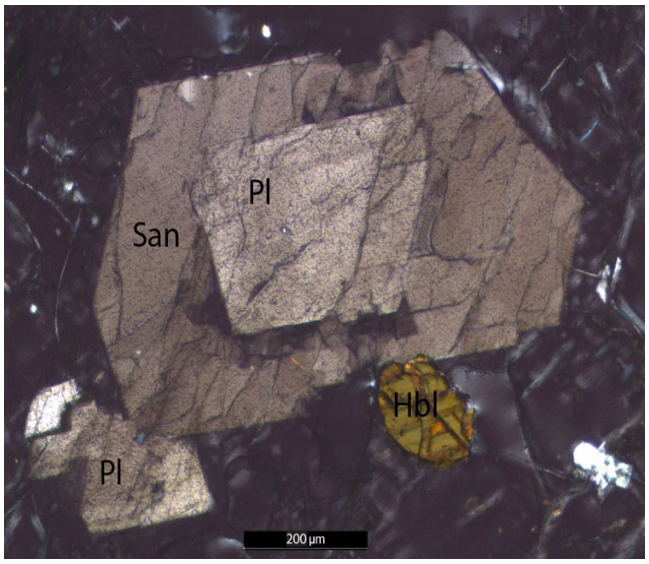

Figure 24.
Glomerocryst of euhedral plagioclase mantled by euhedral sanidine with embayed surfaces where euhedral hornblende and plagioclase are attached. 10x magnification, cross-polarized light.

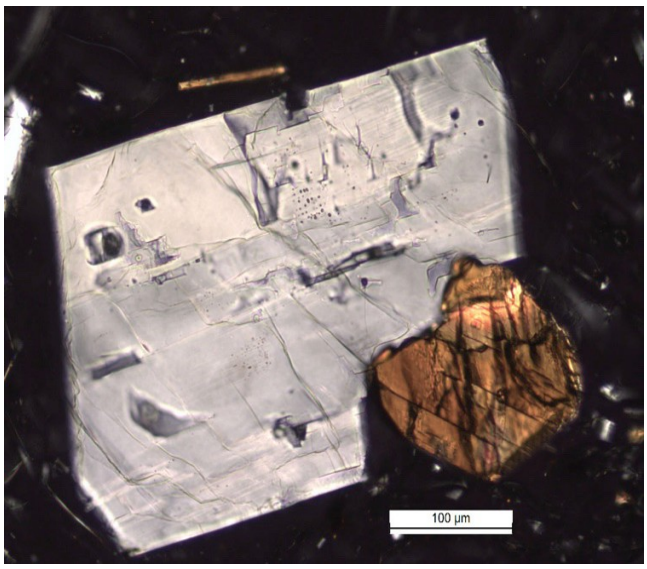

Figure 25.
Glomerocryst of plagioclase and hornblende. Note the cleavage planes in the hornblende and the perthitic twinning of the plagioclase. 20x magnification, cross-polarized light.

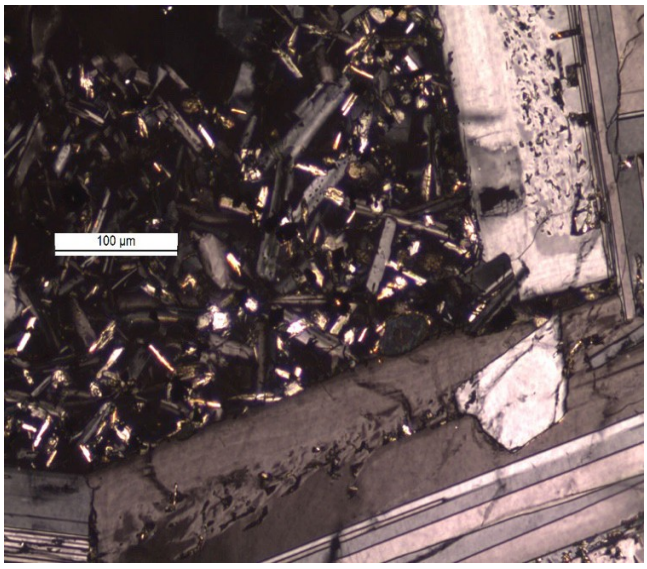

Figure 26.
Glomerocryst of plagioclase phenocrysts in felsic magmatic enclave. Note the spongy cellular texture of the plagioclase along the twinning boundary of the phenocryst. Microlites are plagioclase and hornblende. 20x magnification, cross-polarized light.

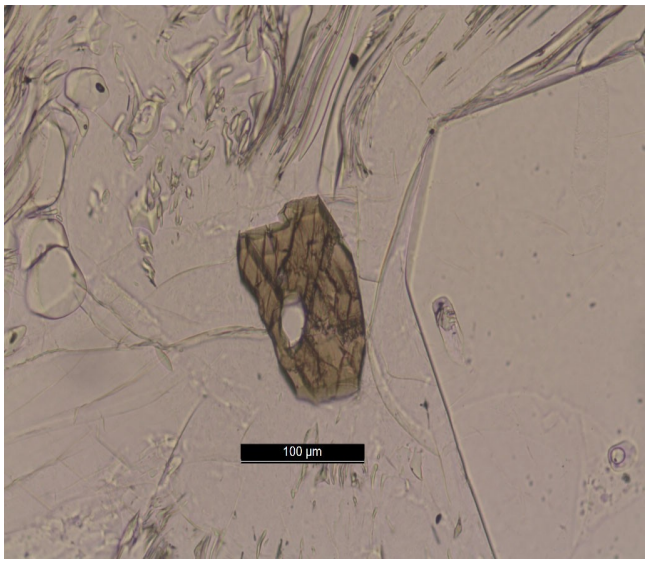

Figure 27.
Euhedral hornblende with internally exposed embayment. Note the 60°-120° cleavage planes. 20x magnification, plain polarized light.

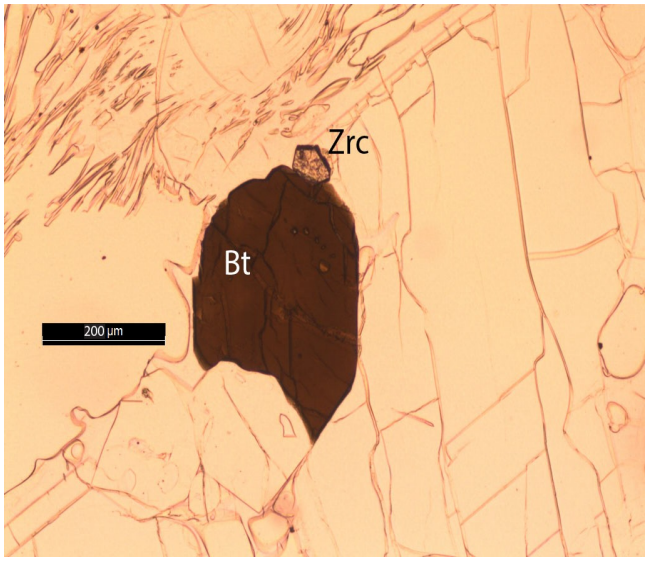

Figure 28.
Euhedral biotite with zircon phenocryst attached on "north" end the biotite crystal. Biotite does not show evidence of embayments since edges of crystal are sharp and defined. 10x magnification, plain polarized light.

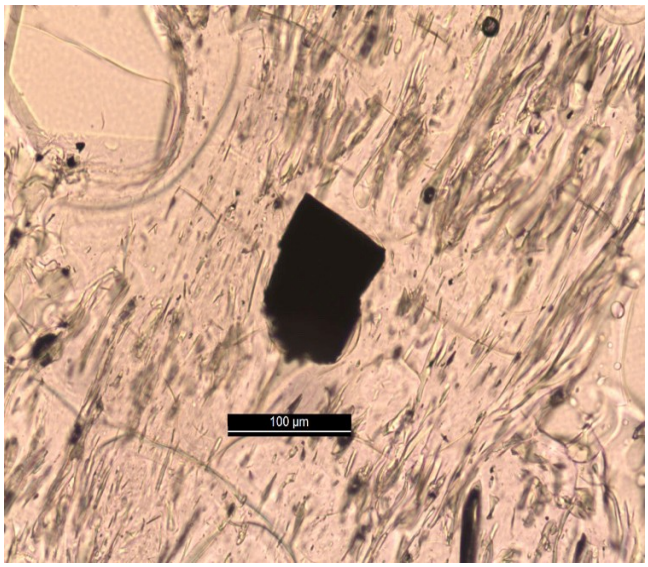

Figure 29.
Euhedral magnetite in glassy matrix. Flow banding evidenced by direction of vesicles in matrix. 20x magnification, plain polarized light.

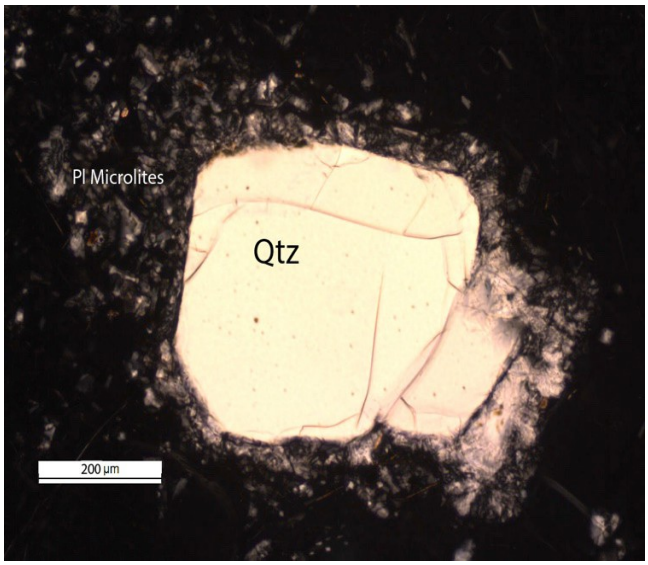

Figure 30.
Resorbed quartz antecryst in a felsic magmatic enclave surrounded by plagioclase microlites. 10x magnitude, cross- polarized light.

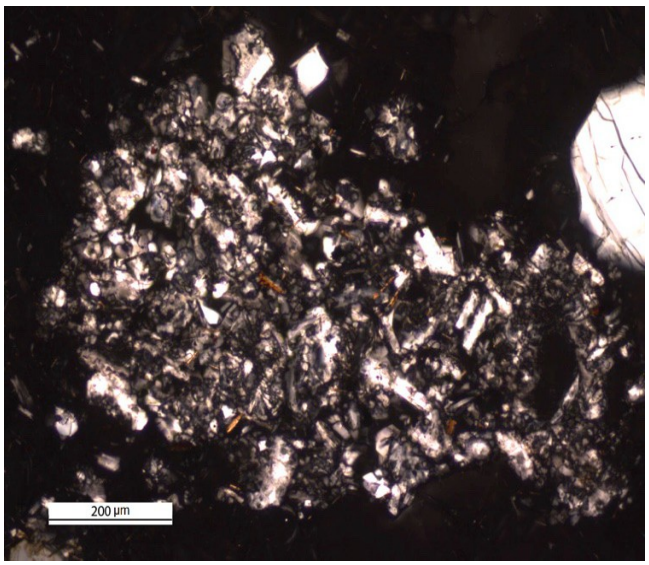

Figure 31.
Felsic magmatic enclave consisting of acicular plagioclase and hornblende microlites. 10x magnification, cross-polarized light.

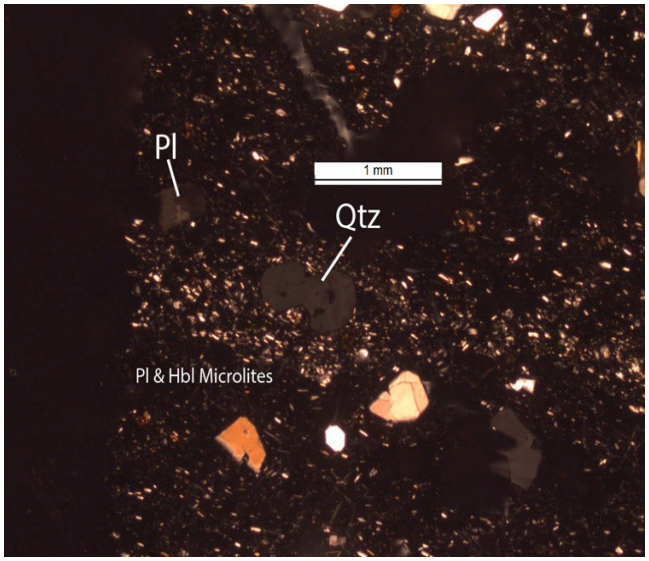

Figure 32.
Felsic magmatic enclave with plagioclase glomerocryst and embayed quartz phenocryst embedded within the enclave. Note that the enclave is stretched along the flow banding of the rhyolite matrix. 2x magnification, cross-polarized light.

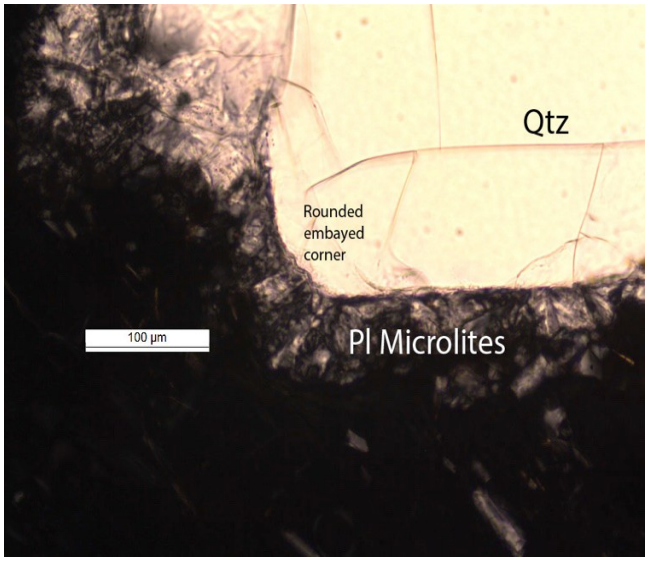

Figure 33.
Embayed quartz corner with plagioclase microlites on edges of quartz phenocryst. Located in felsic magmatic enclave. 20x magnification, cross-polarized light.

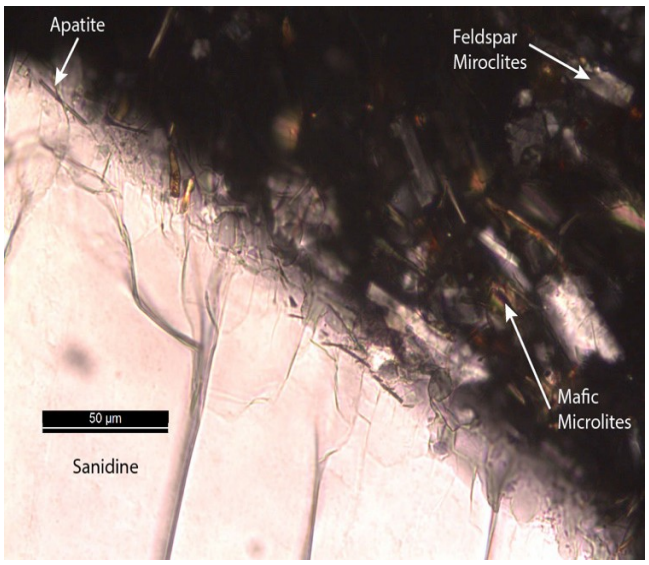

Figure 34.
Sanidine with resorption features along crystal face with apatite inclusions on crystal face. Note presence of feldspar and mafic microlites in close proximity to resorbed crystal face. 40x magnification, cross-polarized light.

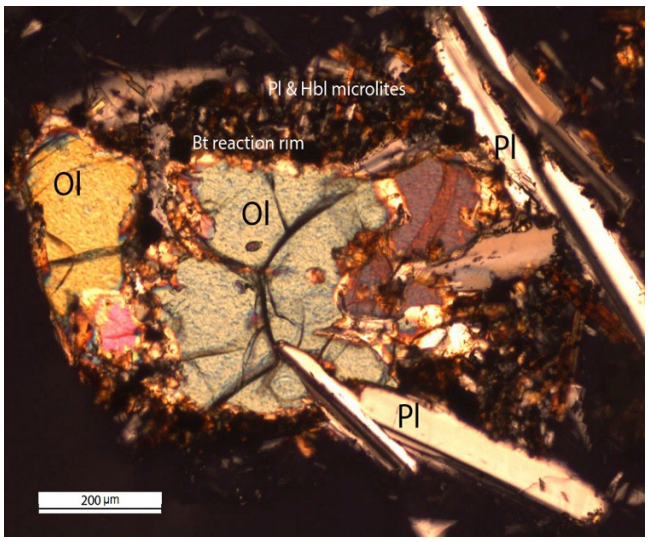

Figure 35.
Mafic magmatic enclave with olivine and plagioclase phenocrysts. Note the biotite reaction rims around the embayed olivine crystals and the embayed textures around the plagioclase crystals. The enclave has sharp boundaries and there are densely packed plagioclase and hornblende microlites. 10x magnification, cross-polarized light.

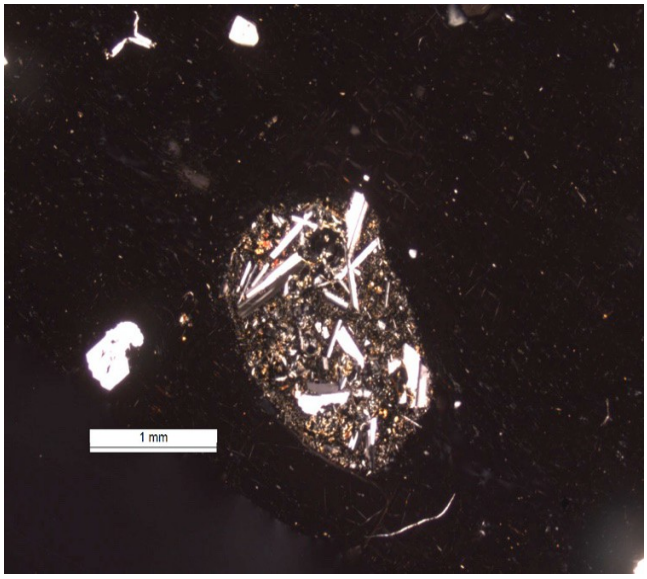

Figure 36.
Mafic magmatic enclave with plagioclase phenocrysts and plagioclase and hornblende microlites. Note the sharp boundary of the enclave. 2x magnitude, cross-polarized light.

Table 7. Point counting data from 7 standard thin sections from China Hat and China Cap lava domes. Abbreviations: Qtz = quartz; Pl = plagioclase; San = sanidine; Bt = biotite; and Hbl = hornblende. Quartz, plagioclase, and sanidine mineral phases separated into euhedral and subhedral categories. Count totals are for all mineral phases except accessory minerals which are point sources and do not constitute measureable volume.

Sample	WKLCC1-14	WKLCC8-14	WKLCC9-14	WKLCH1-15	8220101	8220103	8220104	Averages	Standard Deviation
Counts	1050	950	1000	1000	1000	1000	1000		
Euhedral Qtz	1.33	1.37	0.40	2.50	1.70	2.10	2.60	1.71	0.77
Subhedral Qtz	1.05	2.74	1.90	2.70	2.30	1.90	2.20	2.11	0.58
Total Qtz	2.38	4.11	2.30	5.20	4.00	4.00	4.80	3.83	1.11
Euhedral Pl	1.43	1.68	1.30	2.40	1.60	2.30	2.20	1.84	0.45
Subhedral Pl	1.24	0.53	0.20	0.20	0.80	0.30	0.00	0.47	0.43
Total Pl	2.67	2.21	1.50	2.60	2.40	2.60	2.20	2.31	0.40
Euhedral San	0.38	0.84	0.30	0.50	0.40	1.10	1.30	0.69	0.39
Subhedral San	1.43	1.90	0.80	2.80	1.60	1.20	1.00	1.53	0.67
Total San	1.81	2.74	1.10	3.30	2.00	2.30	2.30	2.22	0.70
Bt	0.29	0.21	0.20	0.00	0.10	0.00	0.10	0.13	0.11
Hbl	0.57	0.00	0.00	0.10	0.10	0.00	0.10	0.12	0.20
Opaque Minerals	0.10	0.21	0.50	0.00	0.40	0.70	0.10	0.31	0.25
Totals	7.82	9.48	5.60	11.20	9.00	9.60	9.60	8.90	1.76

Note: Mineral phases are in percent and rounded to nearest 0.01 percent.

3.3 Thermodynamic Modeling

The following observations are from modeling simulations of the synthetic trachybasalt of Whitaker et al. (2008) and the most primitive olivne tholeiite basalt of Pickett (2004). Data is plotted as major oxides vs. SiO_2. In Appendices 2 and 3, further data is plotted as major oxides vs. MgO. Charts of mineral phases vs. magma tempearture and pyroxene quadrilateral diagrams are presented as applicable for both the rhyolite-MELTS and MCS-rhyolite-MELTS modeling.

3.3.1 ESRP bimodal volcanics analyses (COM-Cedar Butte trend)

Bulk geochemistry results of rhyolite-MELTS modeling of synthetic trachybasalt (100D3) from Whitaker et al. (2008) are similar to experimental observations. The *f*O2 buffer determined by experimental analysis from Whitaker et al. (2008) ranged from -1.8 to -2.6 on the QFM buffer. I used QFM-2 buffer for redox reactions on total FeO (wt.%)

and then suppressed the buffer when performing the model run. I ran the simulations with rhyolite-MELTS version 1.2.0 and suppressed mineral phases except for those listed in Table 3.

Figures 37 through 45 shows total alkalis vs. SiO_2 and Harker diagrams of major oxides vs. SiO_2. The rhyolite-MELTS TAS plots along the alkaline-subalkaline trend from basalt through trachybasalts to trachydacite and follows the experimental composition of Whitaker et al. (2008) and the COM-Cedar Butte trend (Fig. 37). MgO vs. SiO_2 follows the COM-Cedar Butte trend and the experimental data from Whitaker et al. (2008) (Fig. 41) but TiO_2, FeO_{tot}, and K_2O vs. SiO_2 follows below the trend and experimental data (Figs. 38, 40, and 44). Al_2O_3 vs. SiO_2 peaks above both the experminental data and the COM-Cedar Butte trend while CaO vs. SiO_2 follows the trend and experimental data but tracks above (Figs. 40 and 42). Na_2O vs. SiO_2 starts on the trend and experimental data but moves above them when SiO_2 goes above 55 wt.% (Fig. 43). P_2O_5 vs. SiO_2 tracks lower than the experimental data but follows the trend and data between 52 and 60 wt.% SiO_2 and then tracks above the trend and data (Fig. 45).

A plot of mineral phases vs. magma temperature of 100D3 experiments of Whitaker et al. (2008) show olivine, plagioclase, augite, and ilmenite precipitating early at 1100°C with augite precipitation dominating early (Fig. 46). Plagioclase precipitation overtakes augite in later experiments (down to 940°C) and apatite starts to precipitate at 1000°C with pigeonite precipitating late in the experiments at 940°C (Fig. 46).

Rhyolite-MELTS simulations of the 100D3 composition of Whitaker et al. (2008) with equilibrium and fractional crystallization (EC and FC respectively) are also shown (Figs. 47 and 48). The EC rhyolite-MELTS simulation shows ilmenite precipitating early (1160°C) with ulvöspinel and augite precipitating at 1100°C and plagioclase precipitating

at 1040°C (Fig. 47). Augite dominates mineral phase precipitation at 1100°C with pigeonite and Ca-Al-Ti-rich clinopyroxene dominating the formation of mineral phases at 1080°C. Ulvöspinel and apatite forms at 1100°C but not in large numbers (1-3%) (Fig. 47).

The FC rhyolite-MELTS simulation has ilmenite forming at 1160°C with ulvöspinel, apatite, augite, and pigeonite forming at 1100°C (Fig. 48). These two pyroxenes form for a short temperature range (1100°C for augite and 1100°C-1040°C for pigeonite) (Fig. 48). Ca-Al-Ti-rich clinopyroxene forms at 1080°C until 1020°C and plagioclase forms at 1040°C and dominates the mineral phase production until the end of the simulation at 940°C (Fig. 48). Olivine (fayaltie-rich) forms at 1000°C and reaches 5% at 940°C (Fig. 48).

QUILF projections on the pyroxene quadrilateral diagram of olivine and pyroxene from the 100D3 synthetic trachybasalt experiments of Whitaker et al. (2008) show the evolution towards more Fe-rich olivine and pyroxene from 1040°C to 940°C (Fig. 49). Clinopyroxenes produced in the rhyolite-MELTS simulation run of the 100D3 composition from Whitaker et al. (2008) shows much the same trend with the depletion of Mg and the enrichment of Fe^{2+} (Fig. 50). There are three different clinopyroxene produced in the rhyolite-MELTS simulation compared to the two pyroxenes produced in the experiments of Whitaker et al. (2008). Augite and pigeonite are produced but not at the same time (1107°C-1088°C for augite and 1099°C-940°C for pigeonite) and a third clinopyroxene is produced: Ca-Al-Ti-rich clinopyroxene that is plotted above the diopside-hedenbergite region on the pyroxene quadrilateral diagram (Fig. 50).

Further figures of wt.% major oxides vs. wt.% MgO and their trend analysis are shown in Appendix 2.

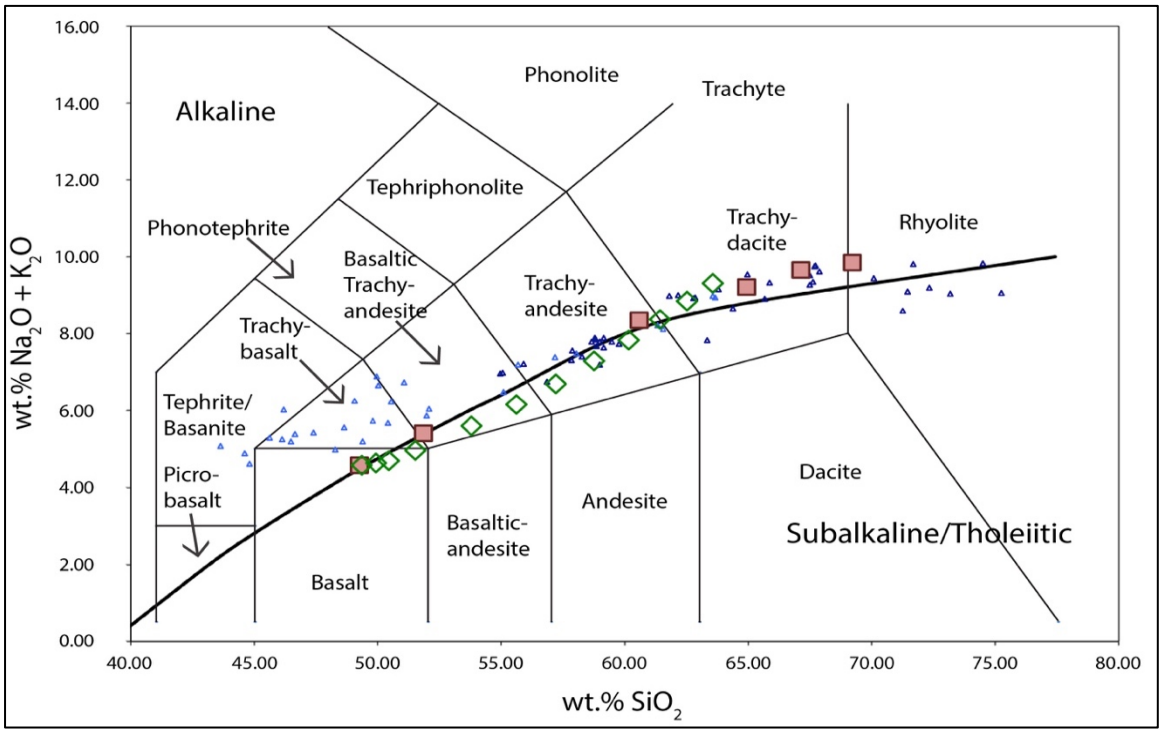

Figure 37. Total alkali vs. silica diagram. Red diamonds are the equilibrium crystallization rhyolite-MELTS model of Whitaker et al. (2008) synthetic trachybasalt (100D3) at 20°C increments. Green diamonds and squares are crystallization experiments of Whitaker et al. (2008) for ICPP123-260 and 100D3, respectively. Triangles are data from Craters of the Moon (light blue) (Kuntz, et al. 1992 and Leeman, 1982b); Cedar Butte (dark blue) (Hayden, 1992 and Spear, 1979). The simulation follows the synthetic trachybasalt experiments of Whitaker et al. (2008) and the COM-Cedar Butte trend from basalt through trachydacite fields.

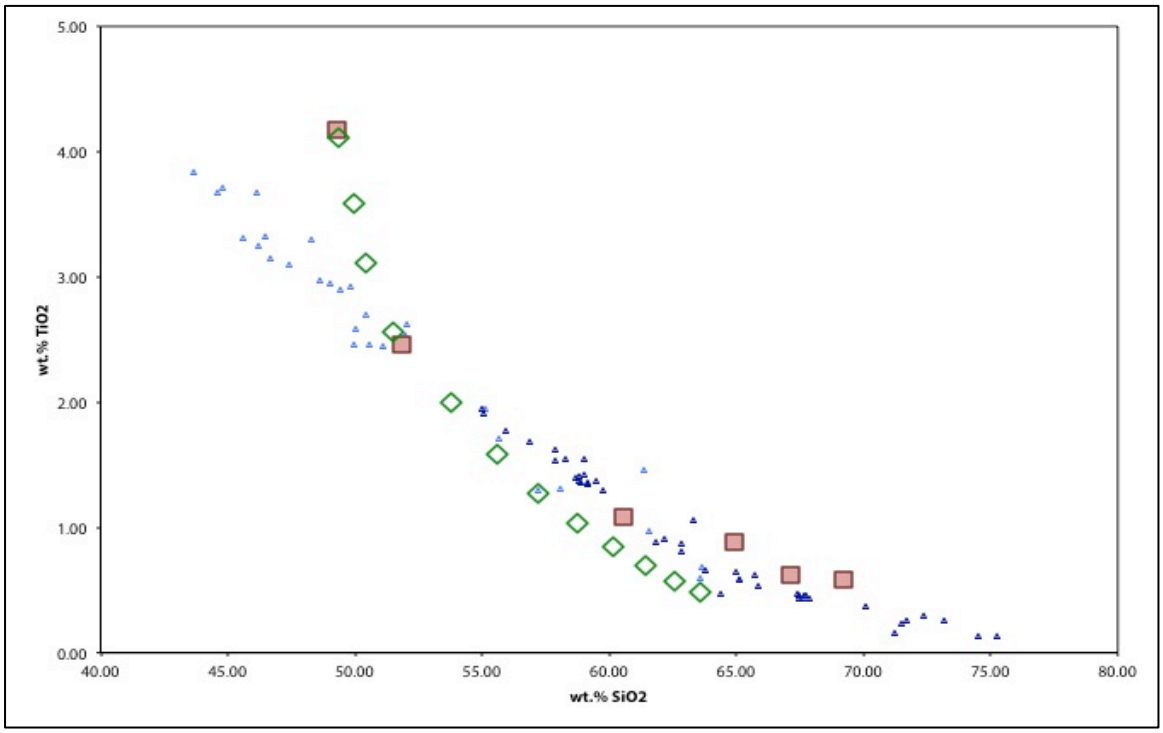

Figure 38. Harker diagram of wt.% TiO_2. Symbols are the same as described in Figure 38. TiO_2 is depleted vs. SiO_2 in a curved linear trend following experiments of synthetic trachybasalt of Whitaker et al. (2008) and the COM-Cedar Butte trend.

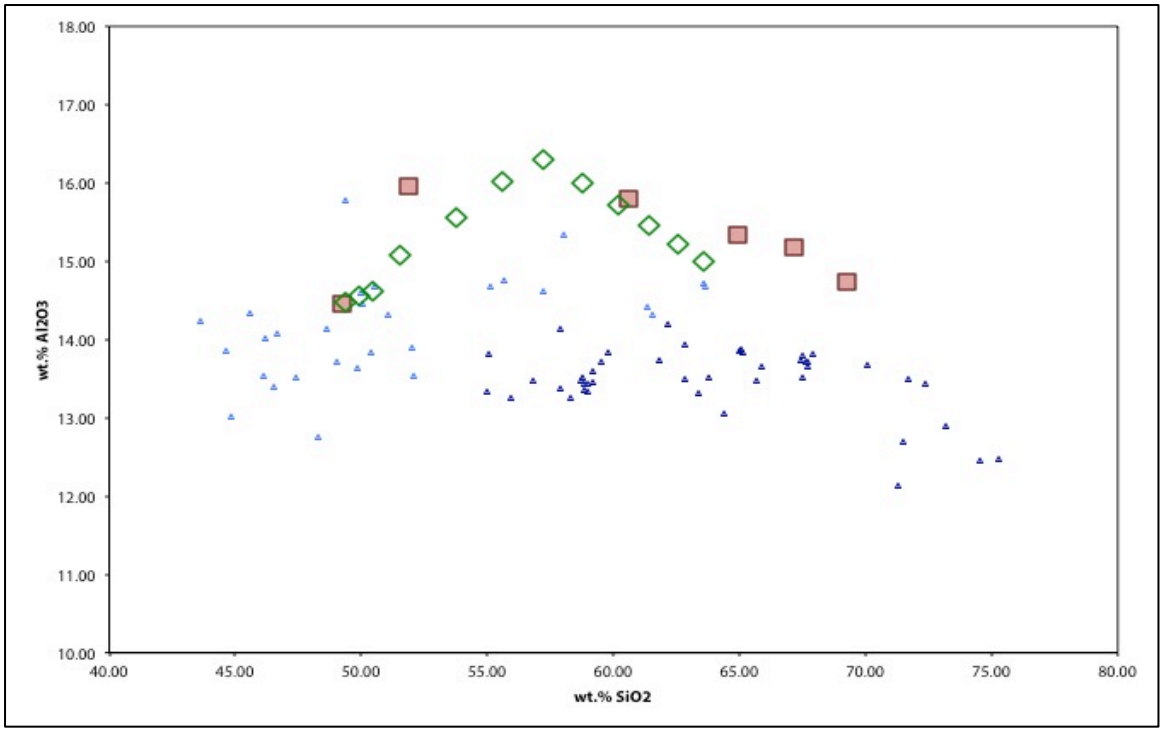

Figure 39. Harker diagram of wt.% Al_2O_3. Symbols are the same as described in Figure 38. The simulation does not follow either the experimental results of the trachybasalt composition of Whitaker et al. (2008) or the COM-Cedar Butte trend.

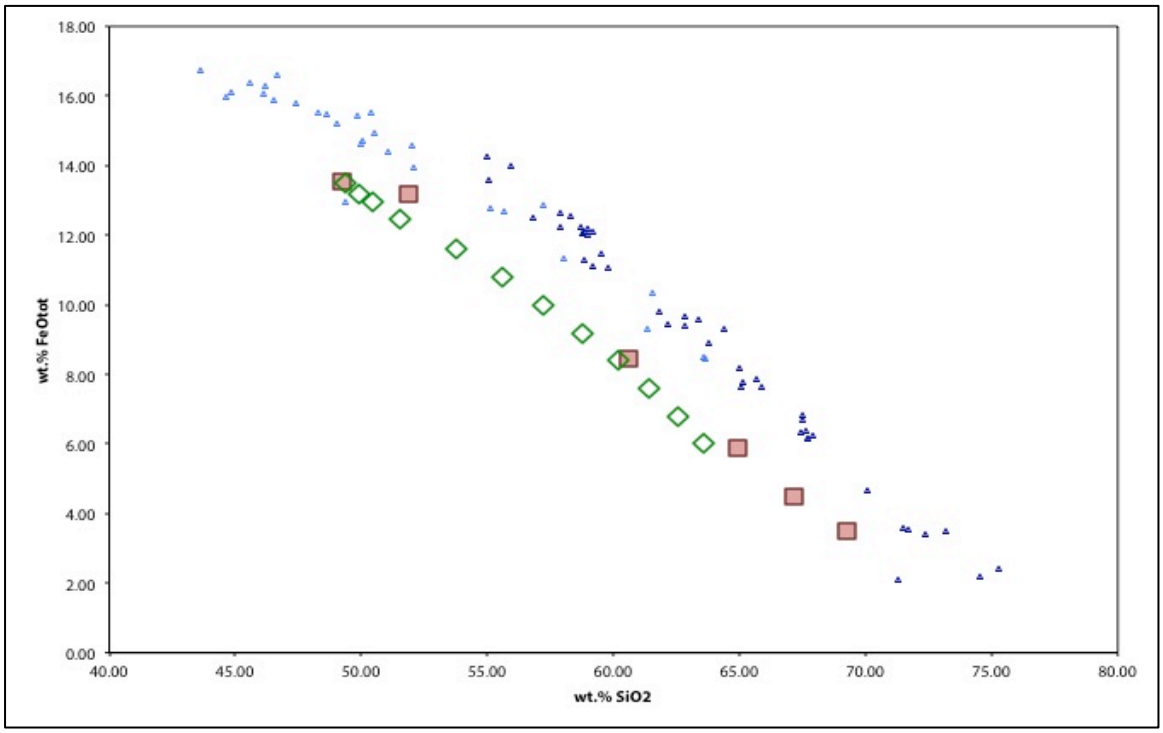

Figure 40. Harker diagram of wt.% FeO_{tot}. Symbols are the same as described in Figure 38. The simulation follows the synthetic trachybasalt trend of Whitaker et al. (2008) and parallels below the COM-Cedar Butte trend.

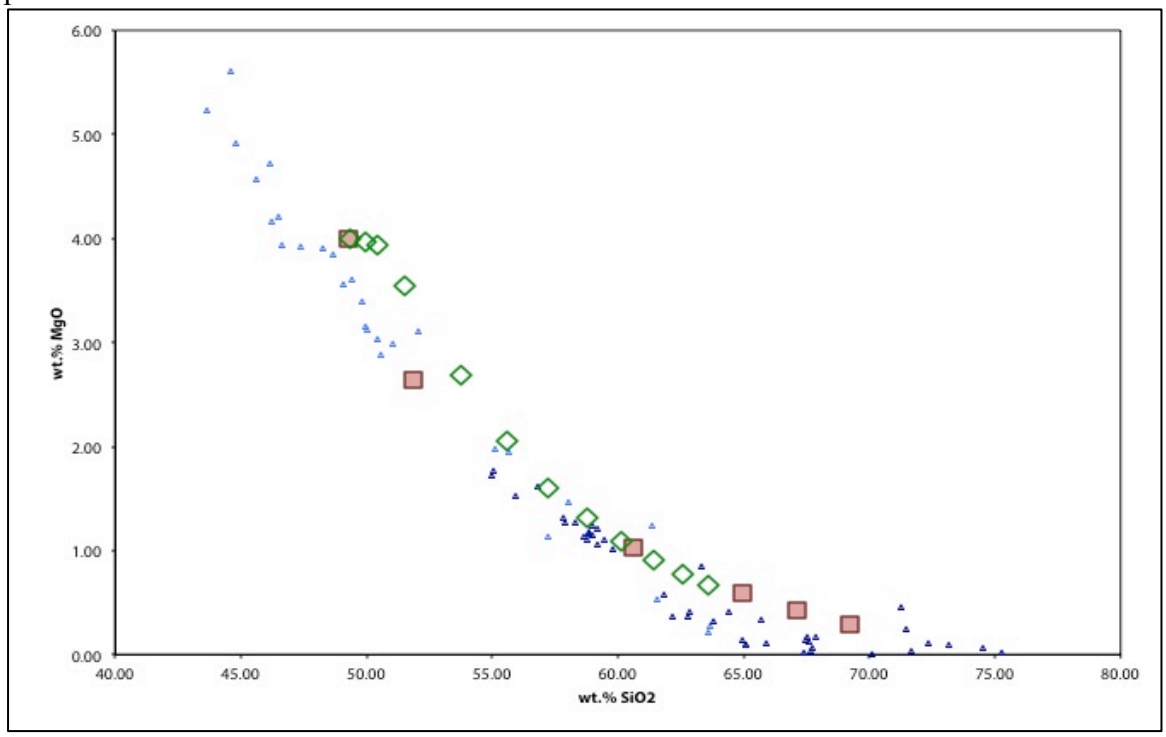

Figure 41. Harker diagram of wt.% MgO. Symbols are the same as described in Figure 38. The simulation follows the curved linear trend of the synthetic trachybasalt experiments of Whitaker et al. (2008) and the COM-Cedar Butte trend.

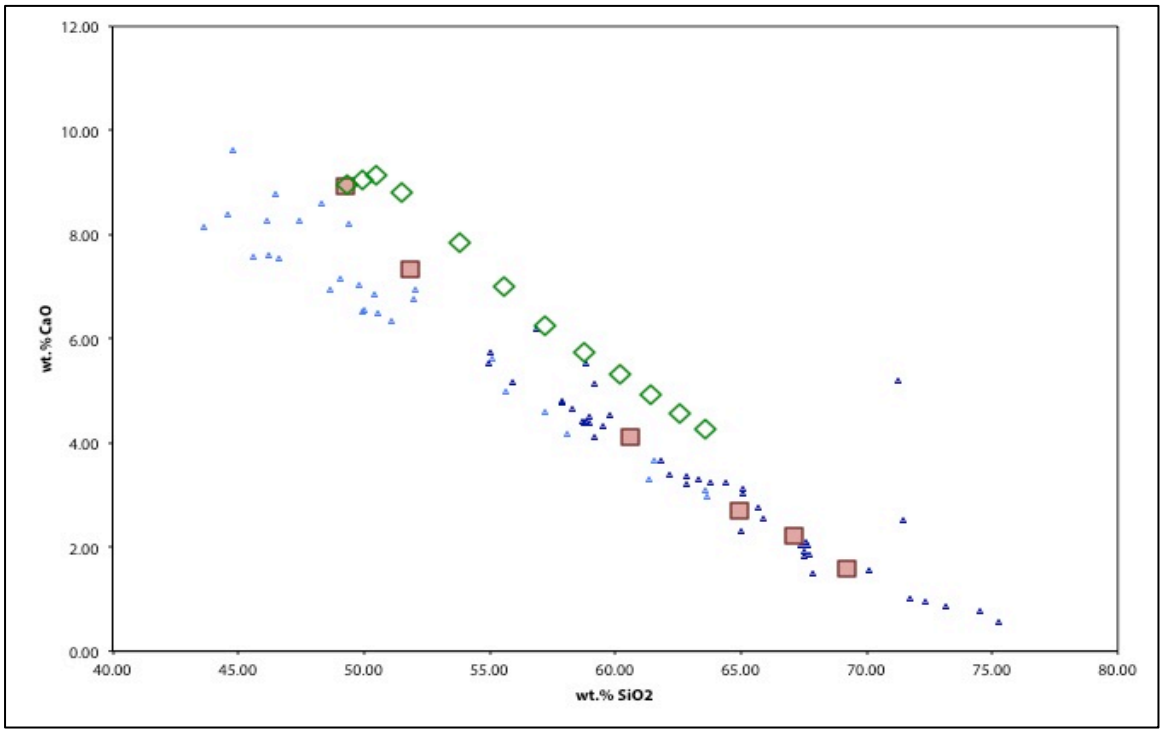

Figure 42. Harker diagram of wt.% CaO. Symbols are the same as described in Figure 38. The simulation run is parallel above the synthetic trachybasalt experiments of Whitaker et al. (2008) and the COM-Cedar Butte trend.

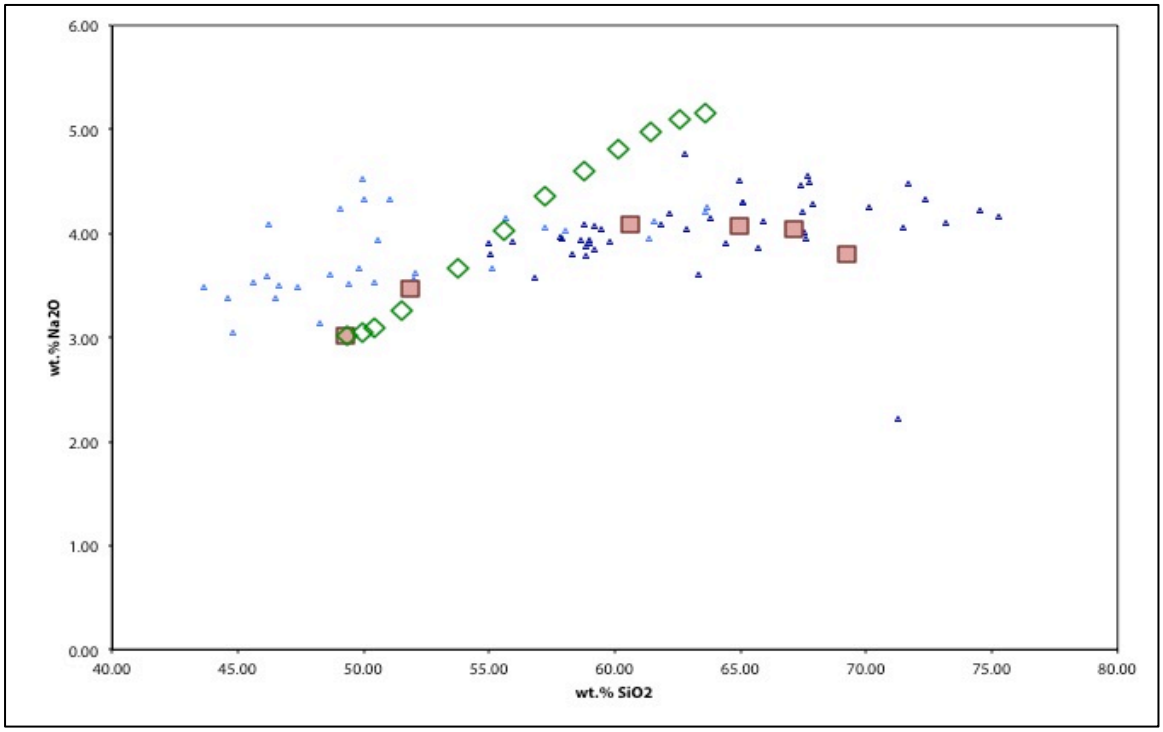

Figure 43. Harker diagram of wt.% Na_2O. Symbols are the same as described in Figure 38. The simulation does not follow the COM-Cedar Butte trend or the synthetic trachybasalt experiments of Whitaker et al. (2008).

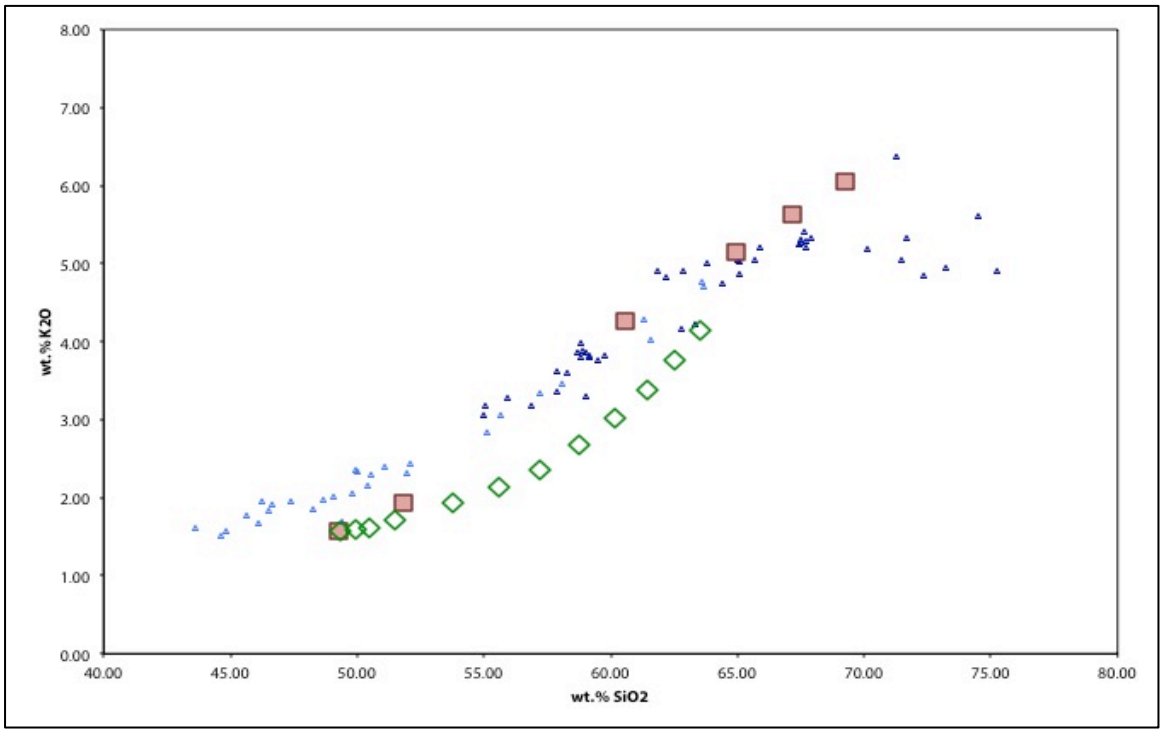

Figure 44. Harker diagram of wt.% K_2O. Symbols are the same as described in Figure 38. The simulation parallels below the curved linear trend of the COM-Cedar Butte trend and the synthetic trachybasalt experiments of Whitaker et al. (2008).

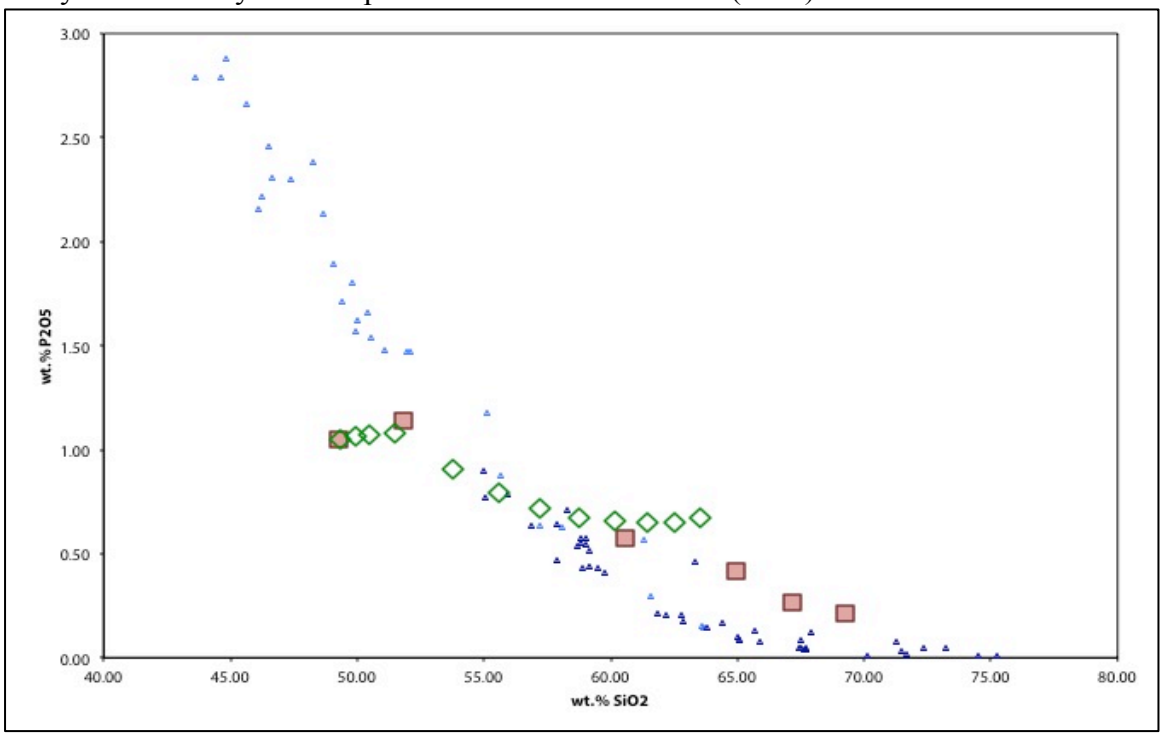

Figure 45. Harker diagram of wt.% P_2O_5. Symbols are the same as described in Figure 38. The simulation does not follow the synthetic trachybasalt experiments of Whitaker et al. (2008).

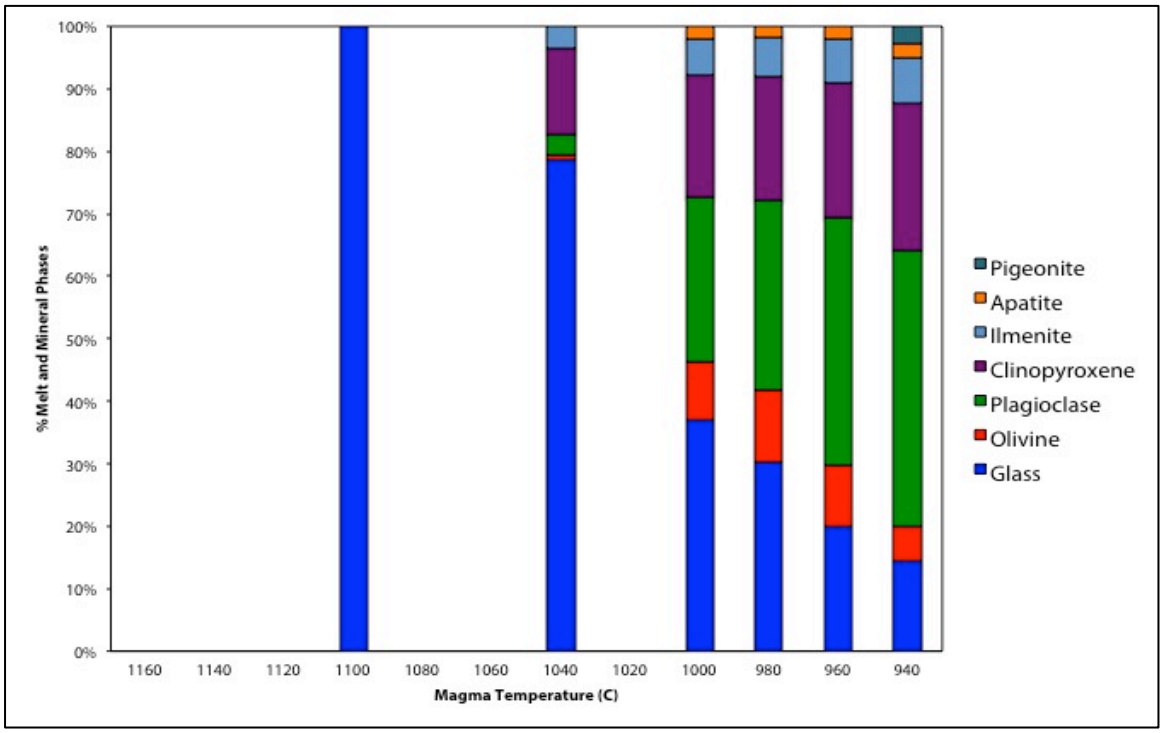

Figure 46. Chart of mineral phase precipitation vs. magma temperature of the synthetic trachybasalt composition of Whitaker et al. (2008) crystallization experiments. From Whitaker et al. (2008) Fig. 9.

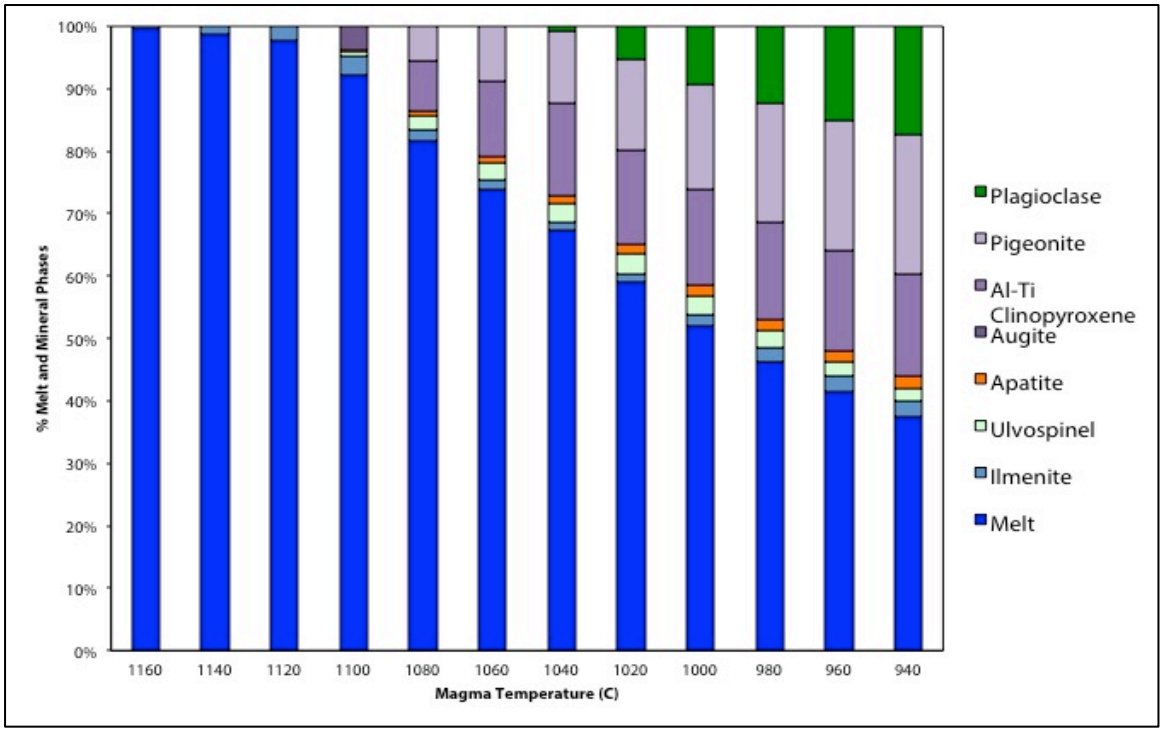

Figure 47. Chart of mineral phase precipitation vs. magma temperature of the synthetic trachybasalt composition of Whitaker et al. (2008) using rhyolite-MELTS simulation run using equilibrium crystallization evolutionary path.

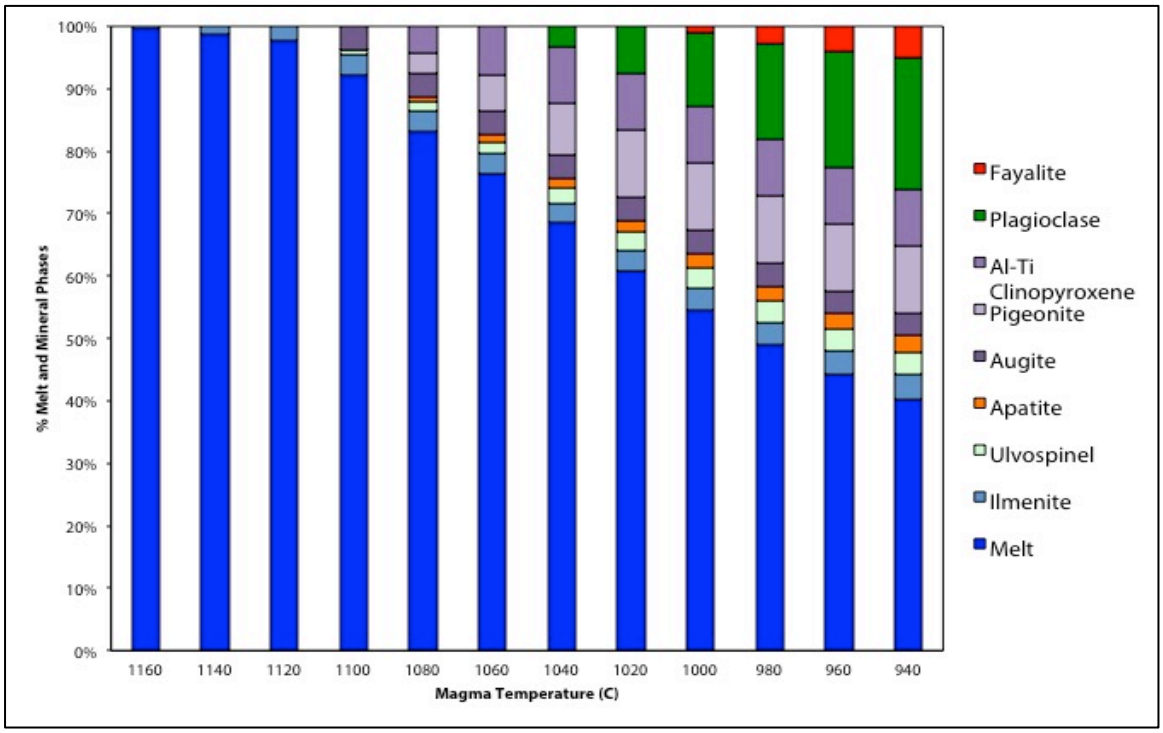

Figure 48. Chart of mineral phase precipitation vs. magma temperature of the synthetic trachybasalt composition of Whitaker et al. (2008) using rhyolite-MELTS simulation run using fractional crystallization evolutionary path.

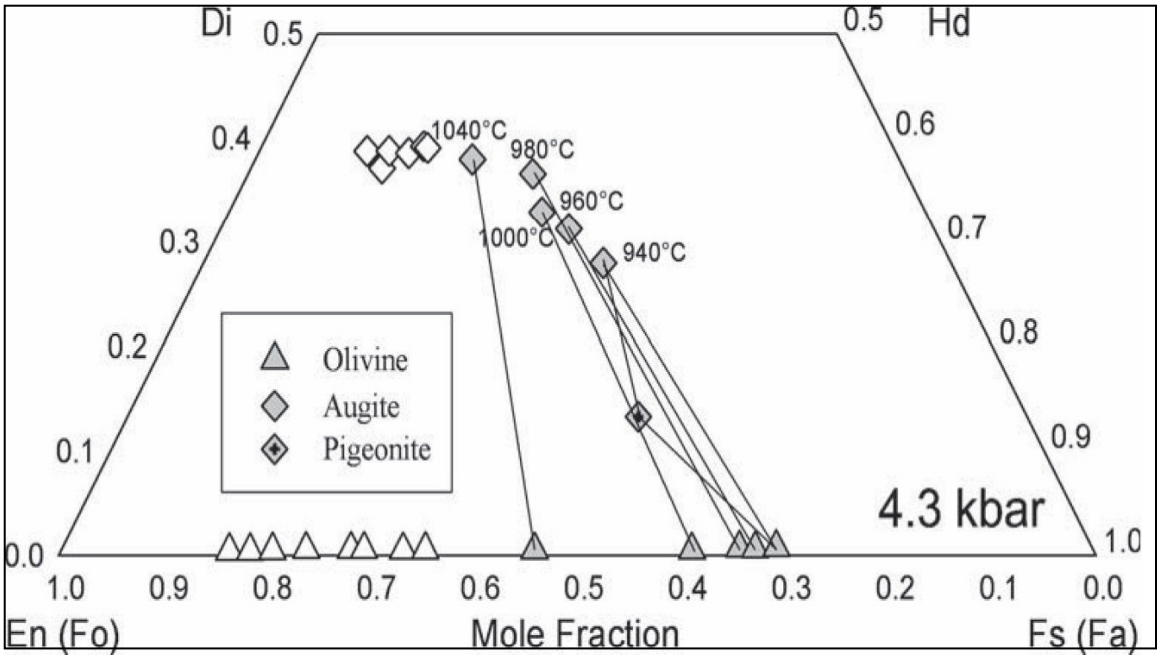

Figure 49. QUILF projections of olivine and pyroxene compositions from experimental run products of 100D3 at 4.3 kbar and 1.8 wt% bulk water content (gray symbols). Tie-lines connect coexisting phases. Open symbols are QUILF projections of olivine and pyroxene compositions of experiments on ICPP123-260 “primitive” olivine tholeiite at 4.3 kbar and 0.4 wt% bulk water content. From Whitaker et al. (2008) Fig. 10.

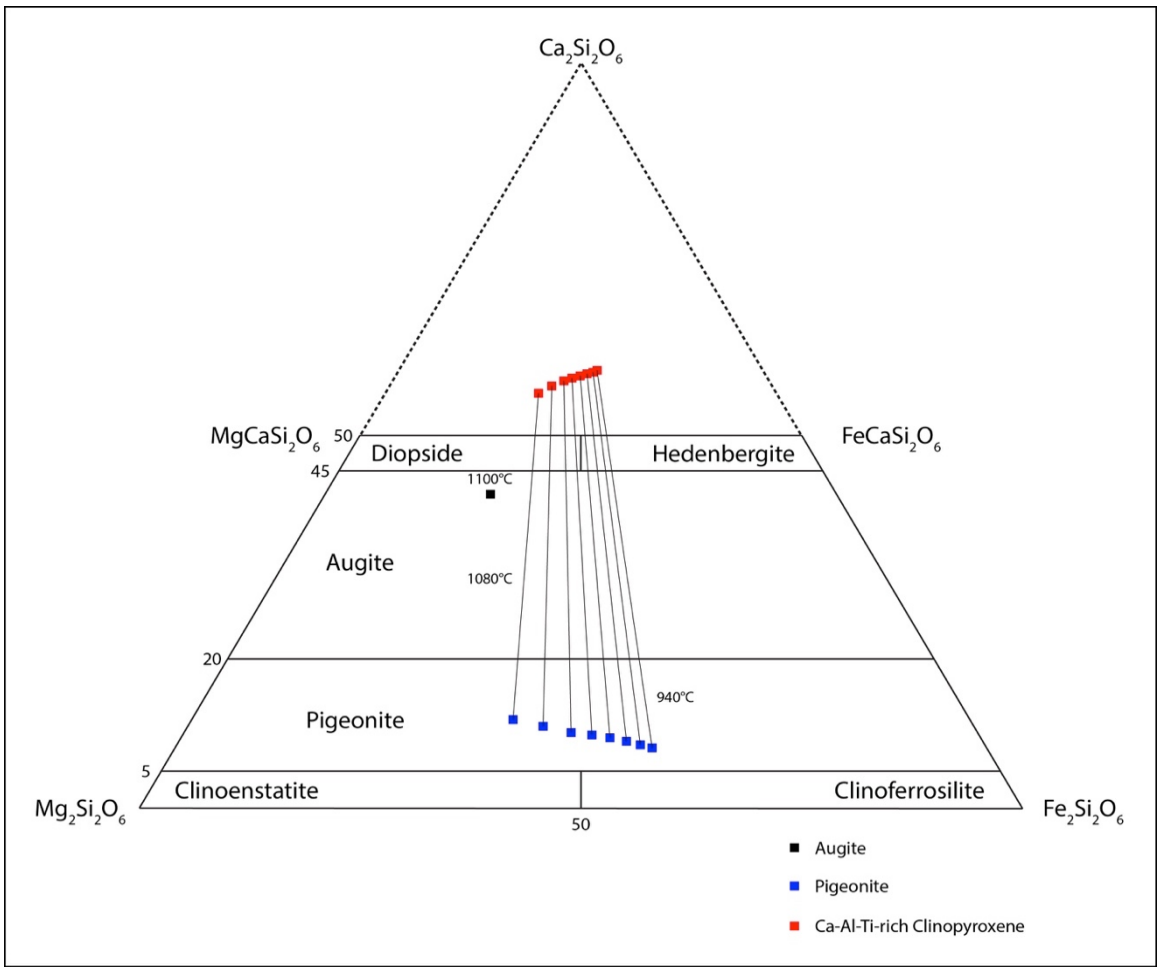

Figure 50. Clinopyroxene quadrilateral diagram from rhyolite-MELTS modeling of 100D3 composition of Whitaker et al. (2008). Three clinopyroxene mineral phases produced during the simulation. Augite precipitated first at 1107°C followed by pigeonite and Ca-Al-Ti clinopryoxene at 1099°C and 1097°C respectively. Tie lines between pigeonite and Ca-Al-Ti clinopyroxene are for every 20°C starting at 1080°C and ending at 940°C. No tie lines connect augite to the other pyroxene phases since the data point for augite is at 1100°C and no other pyroxene is produced at that temperature.

3.3.2 BVF bimodal volcanic analyses

Magma Chamber Simulator (MCS) and rhyolite-MELTS simulations were conducted using the most primitive of the Blackfoot Volcanic Field (BVF) basalts (KEP-004) of Pickett (2004). MCS simulations were used to equilibrate the magma composition with Archean felsic upper crust composition at various depths to ascertain how much wallrock assimilation could occur and what changes to magma composition

would result. Rhyolite-MELTS simulations were run on the KEP-004 composition with fractional crystallization from the liquidus temperature as a control. Rhyolite-MELTS simulations with fractional crystallization were also run on the magma compositions at the end of the completed MCS simulations until and ending temperature of 700°C was reached or the thermodynamic quadratic equations failed to converge.

Table 8. MCS simulations magma and wallrock starting and ending parameters. Temperatures are in °C and H_2O is in wt.%. Magma temperatures are the liquidus and equilibrium temperatures as well as the magma temperature when wallrock assimilation begins. Wallrock temperatures are the solidus, initial, wallrock assimilation temperatures, and equilibrium temperature. FmZero is the portion of wallrock melt before anatectic melt of the wallrock migrates to the magma melt. Wt.% H_2O is for both the starting wallrock and magma compositions.

ID	Pressure (bars)	M Tliq	M Teq	M Tafc	WR Tsol	WR Tinitial	WR Tafc	WR Teq	% Assimilation	Fm Zero	WR H_2O	M H_2O
13Octa.464.11.09.05	4730	1254	926	1113	689	464	755	926	21.26	0.11	0.09	0.05
12Octe.464.09.09.05	4730	1254	928	1119	689	464	748	928	20.39	0.09	0.09	0.05
01Octd.464.08.09.05	4730	1254	930	1123	689	464	740	929	19.75	0.08	0.09	0.05
18Octd.536.10.12.05	3900	1244	970	1152	718	536	722	970	14.29	0.10	0.12	0.05
18Octb.536.09.12.05	3900	1244	970	1156	718	536	719	970	14.42	0.09	0.12	0.05
18Octa.536.08.12.05	3900	1244	970	1156	718	536	719	970	14.61	0.08	0.12	0.05
01Octa.647.11.09.05	4730	1254	1008	1193	689	647	755	1008	29.66	0.11	0.09	0.05
06Octc.647.10.09.05	4730	1254	1009	1195	689	647	752	1009	28.95	0.10	0.09	0.05
06Octa.647.09.09.05	4730	1254	1010	1198	689	647	748	1010	28.59	0.09	0.09	0.05
27Sepe.647.08.09.05	4730	1254	1011	1203	689	647	739	1012	28.10	0.08	0.09	0.05

MCS simulations resulted in wallrock assimilation between 28.10% to 29.66% ascending at 4730 bars and the 35°C/km geothermal gradient with anatectic melt starting from 8% to 11% wallrock melt. At 4730 bars and the 25°C/km geothermal gradient MCS shows wallrock assimilation between 14.29% to 14.61% descending with FmZero increasing from 0.08 to 0.10. At 3900 bars, MCS shows wallrock assimilation between 19.75% to 21.26% ascending at the 35°C/km geothermal gradient with FmZero increasing from 0.08 to 0.11. Continuing the fractional crystallization process, MCS simulation results were used as input into rhyolite-MELTS using the same version as

MCS (v1.0.2) and using the mineral phase settings as used in Table 3 for the synthetic trachybasalt of Whitaker et al. (2008) comparison to COM-Cedar Butte trend.

The TAS diagram shows the fractional crystallization-only case plotting the compostional evolution from basalt and increasing sharply in total alkalis through the trachy-compositions to bordering trachyte and phonolite (Fig. 51). The MCS and rhyolite-MELTS simulations at 4730 bars and wallrock temperature starting at 647°C plots from basalt through the trachy-compositions above the alkaline-subalkaline line and becoming subalkaline in the trachydacite into the rhyolite field following the COM-Cedar Butte trend and Whitaker et al. (2008) experimental data until 65 wt.% SiO_2 where the model composition drops below them (Fig. 51).

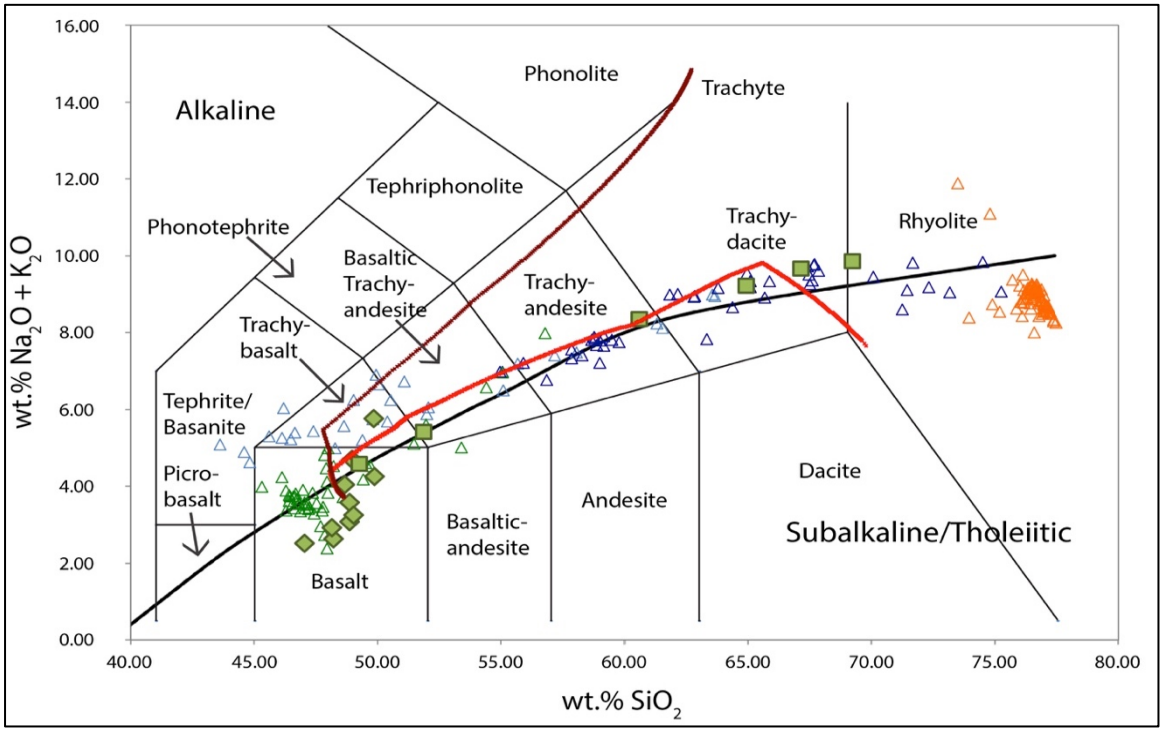

Figure 51. TAS diagram for MCS and rhyolite-MELTS modeling of BVF/China Hat magma system. The dark red line is the FC rhyolite- MELTS simulation of the KEP-004 OTB composition of Pickett (2004). The red line is the AFC MCS-FC rhyolite-MELTS simulation of the KEP-004 olivine tholeiite composition of Pickett (2004). Green diamonds and squares are the crystallization experiments of Whitaker et al. (2008) for ICPP123-260 and 100D3, respectively. Open triangles are data from Craters of the Moon

(light blue) (Kuntz, et al. 1992 and Leeman, 1982b); Cedar Butte (dark blue) (Hayden, 1992 and Spear, 1979); BVF basalts (green); and BVF rhyolites (orange) (Dayvault et al., 1984, Fiesinger et al., 1982, Ford, 2005, and Pickett, 2004). Differences between FC-only (dark red) and AFC and FC (red) simulations are from the 28.10% wallrock assimilation occurring during the MCS modeling that reaches equilibrium between wallrock and magma temperatures. The rhyolite-MELTS fractional crystallization (FC) simulation does not follow the COM-Cedar Butte trend or the synthetic trachybasalt experiments of Whitaker et al. (2008) and moves from basalt through trachybasalt to trachyte. The MCS-rhyolite-MELTS assimilation-fractional crystallization (AFC) simulation does follow the COM-Cedar Butte trend and the synthetic trachybasalt experiments of Whitaker et al. (2008) except when SiO_2 > ~65.00 wt.% and moves from basalt through the trachybasalt-dacite fields to rhyolite near 70.00 wt.% SiO_2

Harker diagrams of major oxides vs. wt.% SiO_2 plot both the rhyolite-MELTS fractional crystallization-only simulation (RM_FC) and MCS and rholite-MELTS assimilation and fractional crystallization simulaiton (MCS_RM_AFC) (Figs. 52 through 59). TiO_2 vs. SiO_2 of RM_FC following the ICCP123-260 crystallization experiments of Whitaker et al. (2008) initially and then dropping below the COM-Cedar Butte trend and synthetic trachybasalt experiments of Whitaker et al. (2008) (Fig. 52). For MCS_RM_AFC, the trend starts the same as the RM_FC plot but moves over to and follows the synthetic trachybasalt data and the COM-Cedar Butte trend (Fig. 52).

The Al_2O_3 vs. SiO_2 of RM_FC and MCS_RM_AFC both initially increase along the OTB trend of ICPP123-260 experimental data but then continue to increase above it and both peak above the COM portion of the COM-Cedar Butte trend above 18 wt.% Al_2O_3 and then slowly decreases with increasing SiO_2, ending above the COM-Cedar Butte trend and the synthetic trachybasalt experimental data (Fig. 53). The FeO_{tot} vs. SiO_2 of RM_FC and MCS_RM_AFC both plot below and follows parallel to the COM-Cedar Butte trend and synthetic trachybasalt experimental data of Whitaker et al. (2008) (Fig. 54). The MgO and CaO vs. SiO_2 of RM_FC and MCS_RM_AFC both follow the COM-

Cedar Butte trend and experimental data of Whitaker et al. (2008) with the RM_FC trending lower than the MCS_RM_AFC plot (Figs. 55 and 56).

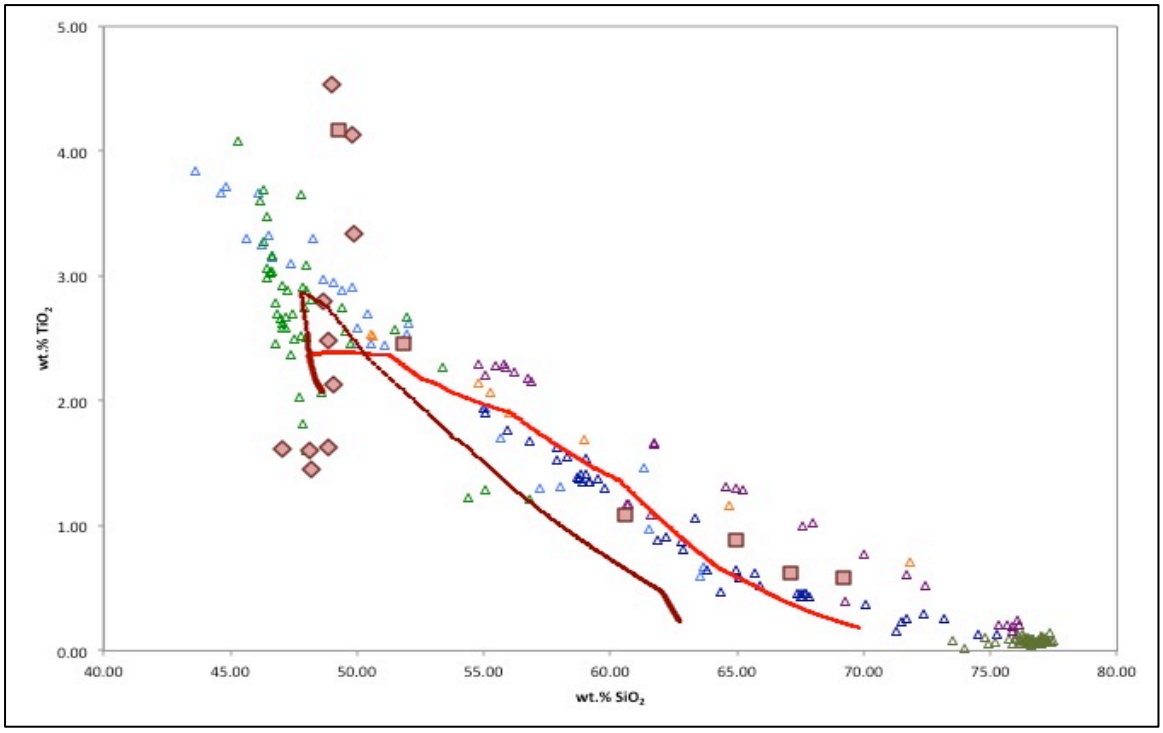

Figure 52. Harker diagram of TiO_2 vs. SiO_2 for MCS and rhyolite-MELTS modeling of BVF/China Hat magma system. Symbols are the same as Figure 52. The rhyolite-MELTS FC simulation does not follow COM-Cedar Butte trend or the synthetic trachybasalt experiments of Whitaker et al. (2008).

The Na_2O vs. SiO_2 of RM_FC initally follows the OTB trend but then continues to increase vs. SiO_2 above the COM-Cedar Butte trend and synthetic trachybasalt data of Whitaker et al. (2008) (Fig. 57). The MCS_RM_AFC plot of Na_2O vs. SiO_2 initally follows the OTB track but trends lower than the COM-Cedar Butte trend and synthetic trachybasalt data with SiO_2 greater than 50 wt.% (Fig 57). The K_2O vs. SIO_2 of RM_FC and MCS_RM_AFC are similar to the TAS diagram but have higher slopes vs. SiO_2 without the lower Na_2O component (Fig. 58). The RM_AFC K_2O vs. SiO_2 plot increases to above 9 wt.% with three data points from the COM trend along the plot (Fig. 58). The MCS_RM_AFC K_2O plot is above the COM-Cedar Butte trend and synthetic

trachybasalt data from Whitaker et al. (2008) and drops to the experimental data at the end of the rhyolite-MELTS simulation above 69 wt.% SiO_2 (Fig. 58). The P_2O_5 vs. SiO_2 plots of RM_FC and MCS_RM_AFC are similar to the 100D3 rhyolite-MELTS simulation (Fig. 59). For RM_FC, P_2O_5 follows the OTB and synthetic trachybasalt data of Whitaker et al. (2008) but increases sharply above 62 wt.% SiO_2 (Fig. 59). The MCS_RM_AFC plot of P_2O_5 has a shallow increasing slope vs. SiO_2 until 54 wt.% SiO_2 then slowly decreases not following the COM-Cedar Butte trend until 65 wt.% SiO_2 when P_2O_5 increase sharply (Fig. 59).

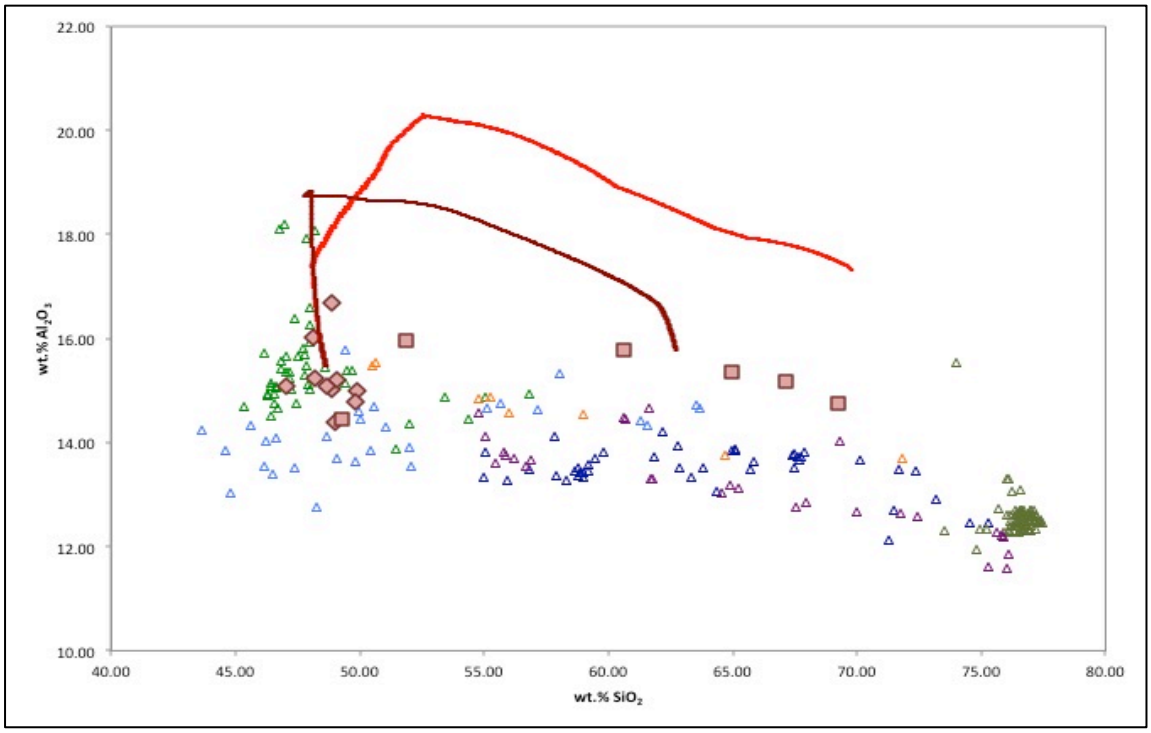

Figure 53. Harker diagram of Al_2O_3 vs. SiO_2 for MCS and rhyolite-MELTS modeling of BVF/China Hat magma system. Symbols are the same as Figure 52. Neither the rhyolite-MELTS FC simulation or the MCS-rhyolite-METLS AFC simulation follow the COM-Cedar Butte trend or the synthetic trachybasalt experiments of Whitker et al. (2008).

Major mineral phases are precipitated in the MCS_RM_AFC and RM_FC simulations and plotted vs. magma temperature (Figs. 60 and 61). In the MCS_RM_AFC simulations orthopyroxene (entstatite) is precipitated first at 1240°C and then stops above

1200°C with two clinopyroxenes, augite and pigeonite precipitating next at 1200°C and 1160°C, respectively (Fig. 60). Pigeonite stops forming above 1040°C but augite continues to precipitate until 920°C (Fig. 60). Ulvöspinel, plagioclase, and apatite appear to 1080°C with plagioclase increasing in its percentage of the total throughout the rest of the simulation (Fig. 60). Ulvöspinel transitions to magnetite at temperatures less than 1040°C after ilmenite starts to form (Fig. 60). Olivine precipitates at 880°C along with alkali feldspar which increases to greater than 10% of the total melt-mineral phases assemblage by the end of the rhyolite-MELTS simulation at 762°C (Fig. 60).

In the RM_FC simulation, mineral phases are similar to the MCS_RM_AFC simulations but are in different proportions and precipitation temperatures (Fig. 61). Orthopyroxene precipitates at 1240°C and stops at 1200°C when clinopyroxene precipitates (Fig. 61). The low-Ca clinopyroxene (pigeonite) precipitates then augite forms (Fig. 61). Pigeonite is formed in lower amounts than augite from 1200°C to 1120°C when augite stops formation and pigeonite continues to 1040°C (Fig. 61). Plagioclase forms at 1160°C and increases in percentage until the end of the simulation at 847°C (Fig. 61). Spinel and Ca-Al-Ti-rich clinopyroxene forms at 1120°C with the clinopyroxene ending formation at 1040°C and spinel formation transforms into ulvöspinel until the end of the simulation (Fig. 61). Apatite forms at 1080°C and increases its percentage more than in the MCS-RM_AFC simulations (Fig. 61). Olivine forms at 1040°C and also forms more than in the MCS_RM_AFC simulations with 4.4% by the end of the simulation (Fig. 61). Ilmenite forms at 960°C and precipitates slowly with 1.2% formed by 847°C (Fig. 61). Alkali feldspar is the last mineral precipitated, first observed at 880°C with 4.2% formed by 847°C (Fig. 61).

Further figures of wt.% major oxides vs. wt.% MgO and their trend analysis are shown in Appendix 3.

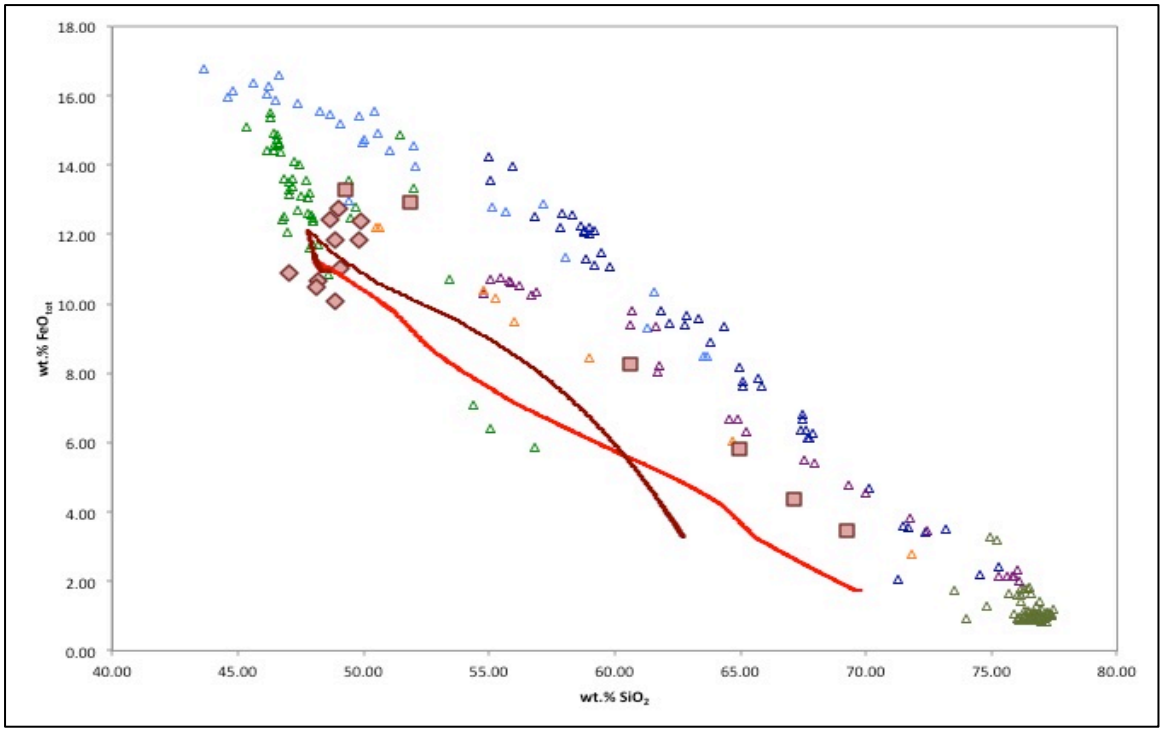

Figure 54. Harker diagram of FeO_{tot} vs. SiO_2 for MCS and rhyolite-MELTS modeling of BVF/China Hat magma system. Symbols are the same as Figure 52. Both the rhyolite-METLS FC simulation and the MCS-rhyolite-MELTS AFC simulation parallels below the COM-Cedar Butte trend and the synthetic trachybasalt experiments of Whitaker et al. (2008).

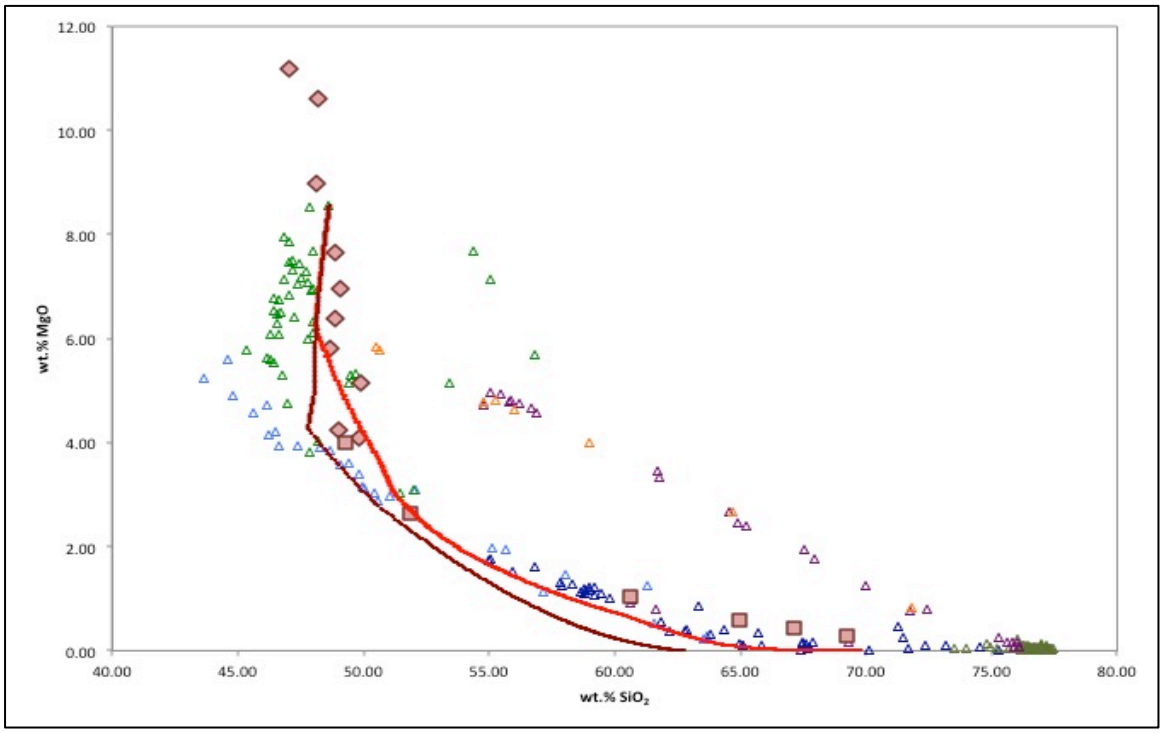

Figure 55. Harker diagram of MgO vs. SiO_2 for MCS and rhyolite-MELTS modeling of BVF/China Hat magma system. Symbols are the same as Figure 52. Both the rhyolite-MELTS FC simulation and the MCS-rhyolite-MELTS AFC simulation follows the COM-Cedar Butte trend and the synthetic trachybasalt experiments of Whitaker et al. (2008) with the FC simulation lower than the AFC simulation.

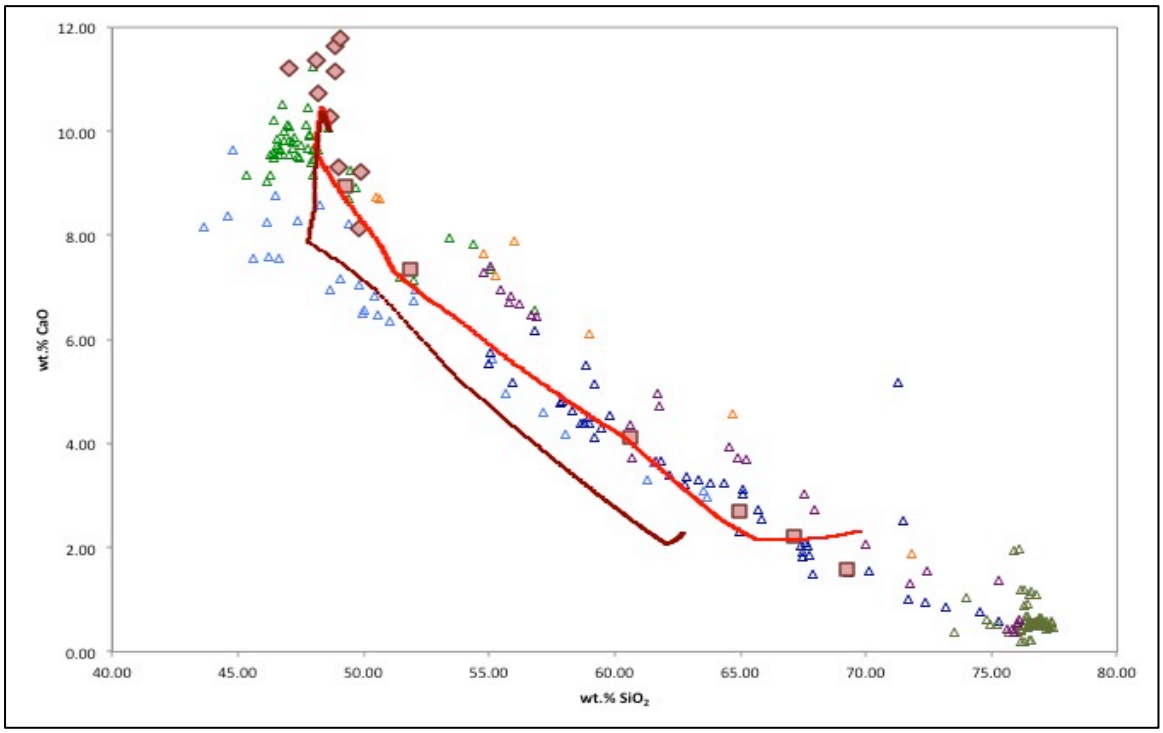

Figure 56. Harker diagram of CaO vs. SiO_2 for MCS and rhyolite-MELTS modeling of BVF/China Hat magma system. Symbols are the same as Figure 52. The rhyolite-METLS FC simulation parallels below the COM-Cedar Butte trend and the synthetic trachybasalt experiments of Whitaker et al. (2008). The MCS-rhyolite-MELTS AFC simulation follows the COM-Cedar Butte trend and the synthetic trachybasalt experiments of Whitaker et al. (2008).

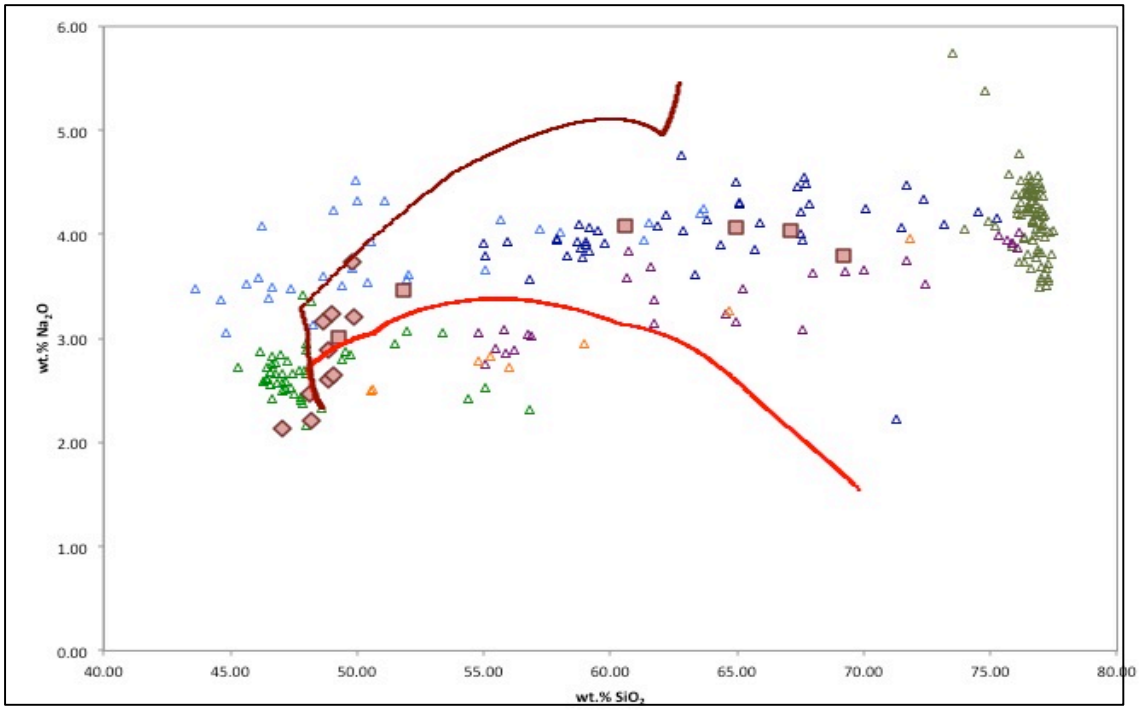

Figure 57. Harker diagram of Na_2O vs. SiO_2 for MCS and rhyolite-MELTS modeling of BVF/China Hat magma system. Symbols are the same as Figure 52. Neither the rhyolite-MELTS FC simulation or the MCS-rhyolite-METLS AFC simulation follows the COM-Cedar Butte trend or the synthetic trachybasalt experiments of Whitaker et al. (2008) with the FC simulation higher and the AFC simulation lower than the plotted data.

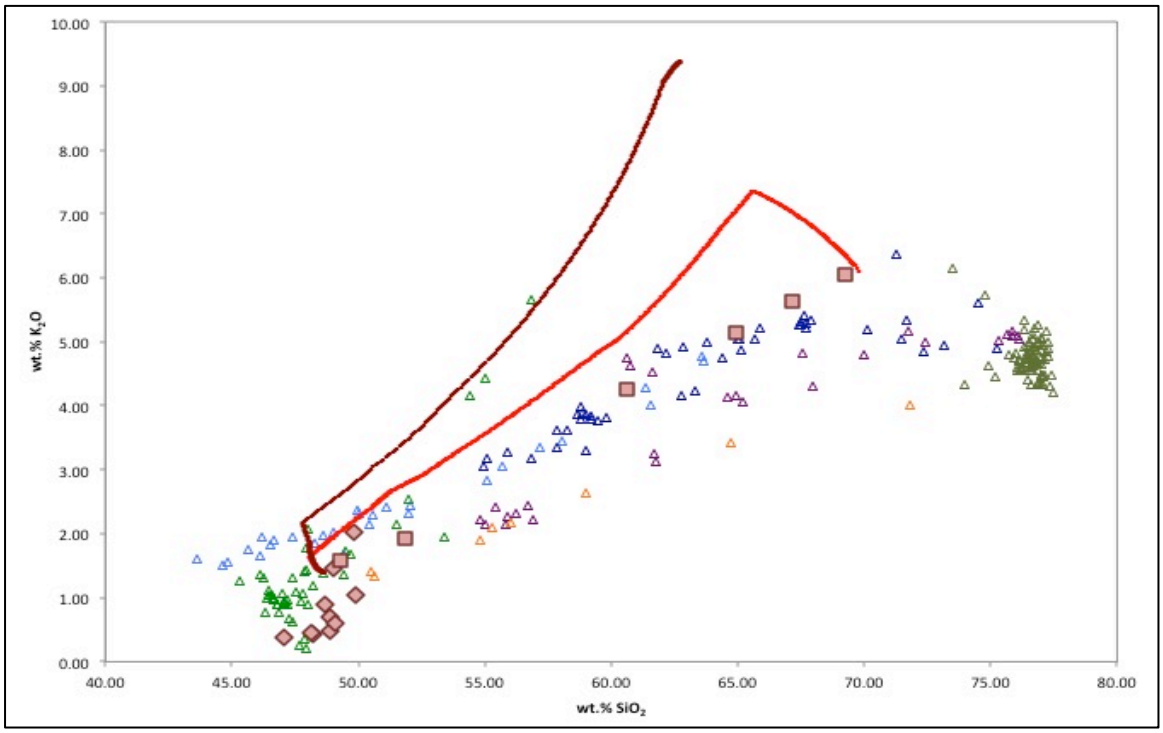

Figure 58. Harker diagram of K_2O vs. SiO_2 for MCS and rhyolite-MELTS modeling of BVF/China Hat magma system. Symbols are the same as Figure 52. The rhyolite-MELTS FC simulation does not follow the COM-Cedar Butte trend or the synthetic trachybasalt experiements of Whitaker et al. (2008). The MCS-rhyolite-MELTS AFC simulation parallels above the COM-Cedar Butte trend and the synthetic trachybasalt experiements of Whitaker et al. (2008).

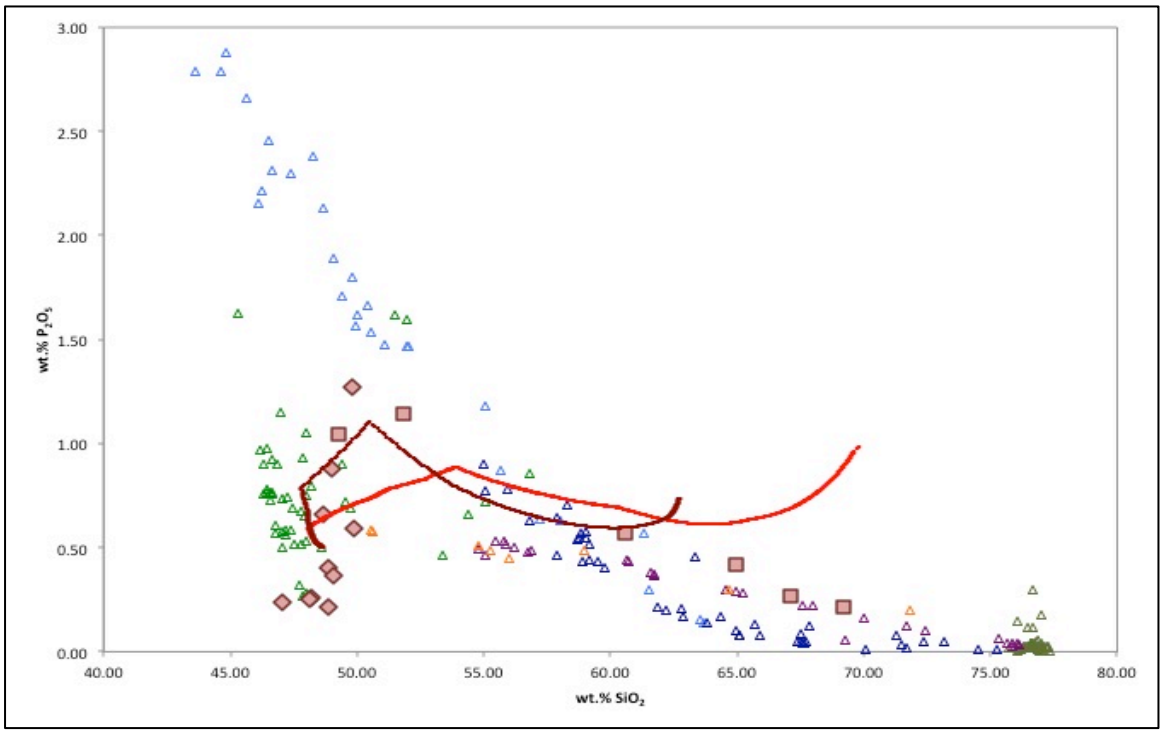

Figure 59. Harker diagram of P_2O_5 vs. SiO_2 for MCS and rhyolite-MELTS modeling of BVF/China Hat magma system. Symbols are the same as Figure 52. Both the rhyolite-MELTS FC simulation run and the MCS-rhyolite-MELTS AFC simulation run do not follow the COM-Cedar Butte trend or the synthetic trachybasalt experiments of Whitaker et al. (2008).

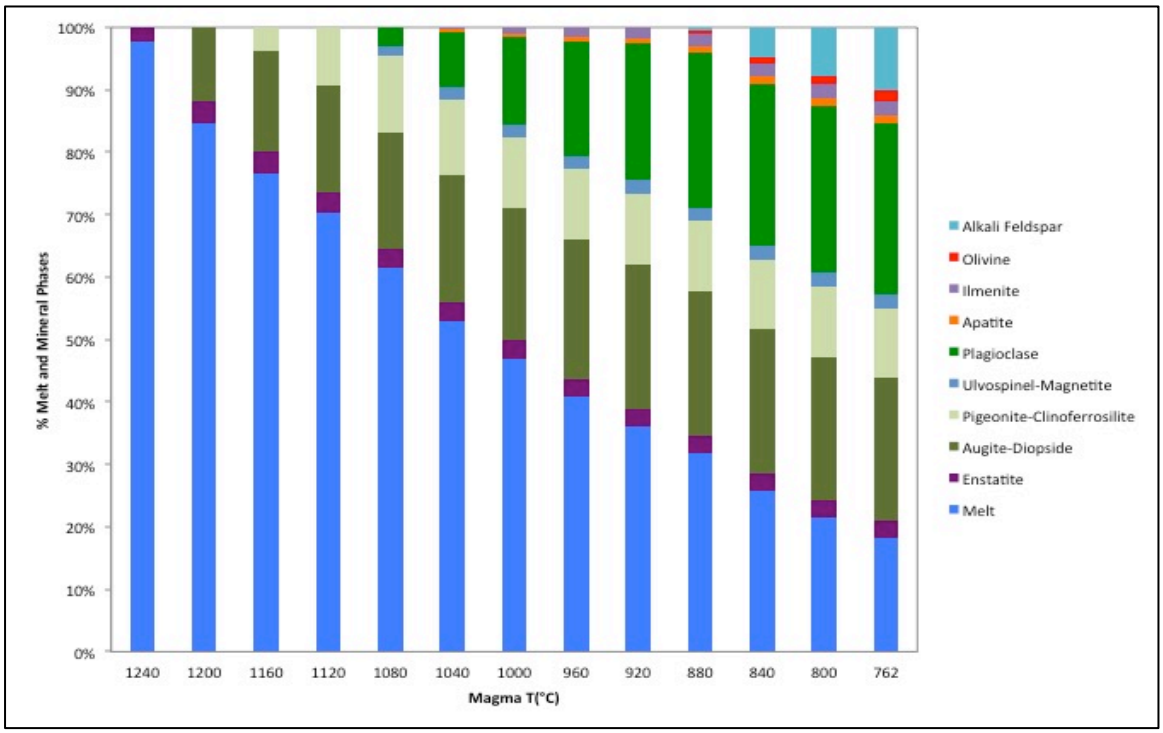

Figure 60. Chart of mineral phase precipitation vs. magma temperature for MCS-rhyolite-MELTS model of BVF OTB (KEP-004) from Pickett (2004). Parameters are pressure = 4730 bars, Archean felsic upper crust wallrock composition, 0.9 wt.% H_2O wallrock content, 0.5 wt.% H_2O magma content, wallrock melt threshold = 0.08, and 28.10% wallrock assimilation with the magma. Temperature increments are every 40°C.

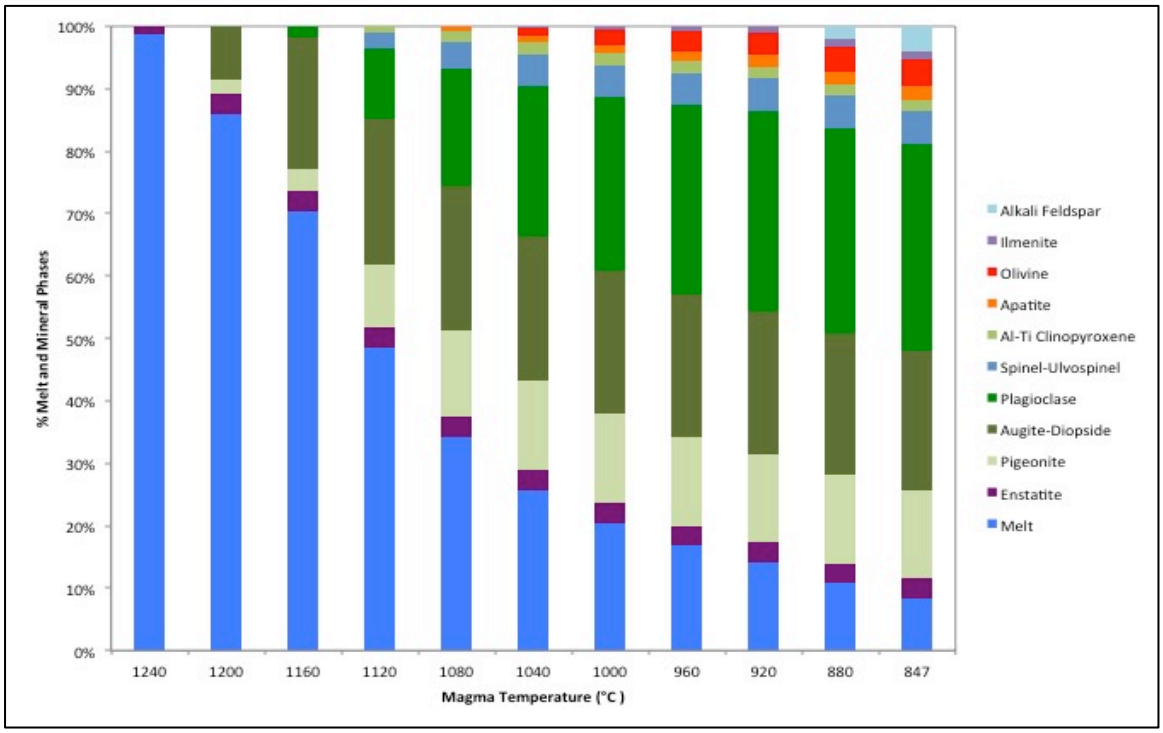

Figure 61. Chart of mineral phase precipitation vs. magma temperature for rhyolite-MELTS fractional crytallization only of KEP-004 composition of Pickett (2004). Parameters are pressure = 4730 bars and 0.5 wt.% H_2O magma content. Temperature increments are every 40°C.

Chapter 4

DISCUSSION

This chapter focuses on the paragenetic interpretation of the phenocryst cargo of the CHDF and the robustness of the rhyolite-MELTS modeling of the synthetic trachybasalt of Whitaker et al. (2008) compared to the Cedar Butte-Craters of the Moon trend and MCS modeling of the Blackfoot Volcanic Field bimodal basalt and rhyolites.

4.1 Paragenetic Interpretation of Phenocryst Cargo

In this section I discuss the different types of phenocrysts and their textures that are observed in the CHDF. This includes an interpretation of phenocryst formation and the conditions of where they formed.

Autocrysts in the CHDF can be identified as either euhedral or boxy-cellular, meaning they are euhedral but have a skeletal outline filled in by glassy matrix. Quartz, sanidine, plagioclase, hornblende, biotite, and magnetite are observed as euhedral crystals and only sanidine and quartz are observed having either euhedral or boxy-cellular features.

Antecrysts are phenocrysts that form from coeval melt in the same magma reservoir and may have been recycled through magma replenishment events or stored as cumulates and reintroduced into the current melt prior to eruption (Jerram and Martin, 2008). Embayments along crystal faces and rounded corners are the surfaces seen as evidence of resorption. Some of the embayments may intrude into interior areas of a crystal and this is seen as rounded sections of a crystal that are in the same crystallographic orientation.

In the CHDF, antecrysts are identified as subhedral crystals with either flat

surfaces with embayments, rounded corners due to resorption, or extremely embayed crystals. The mineral phases identified as antecrysts are: sanidine, plagioclase, quartz, hornblende, biotite, and opaque mineral phases (magnetite and ilmenite). The most strongly embayed crystals are quartz and sanidine (Figs. 15 and 18).

Xenocrysts are crystals that are foreign to the magma reservoir but have been incorporated into the reservoir by physical processes (Jerram and Martin, 2008). Such processes include wallrock assimilation and magma replenishment by more mafic melts. Xenocrysts are identified by mineral phases that do not form in the current melt or have reaction rims around them. Xenocrysts are also identified by being in MMEs that are surrounded by dense microlite aggregates or in glomerocrysts that have crystals that are larger than the surrounding population of autocrysts and antecrysts.

In the CHDF, xenocrysts are identified as olivine, plagioclase, and in one case, pyroxene in MMEs. Olivine is observed with reaction rims of biotite and can be embayed on all surfaces. Plagioclase xenocrysts are larger than most of the felsic plagioclase and are usually in MMEs as glomerocrysts with other plagioclase and/or olivine or in glomerocrysts with other large plagioclase crystals. Some plagioclase xenocrysts have spongy cellular cores with zoned and/or euhedral rims (Fig. 25). Some plagioclase xenocrysts can be found as glomerocrysts in the felsic glassy matrix with other plagioclase and smaller hornblende or biotite phases present and are not surrounded by enclave microlites.

Glomerocrysts are groupings of the same or different mineral phases that grew together by synneusis or through simultaneous resorption and new growth (Hogan, 1993). Synneusis is the process where two neighboring crystals drift together and attach along

crystal faces and new crystal growth surrounds the joined crystals. Glomerocrysts that form through resorption and new growth have crystals that may come from a variety of sources such as: xenocrysts from wallrock or magma injection; antecrysts from other parts of the magma reservoir; or autocrysts that form in proximity to where the glomerocryst forms (Hogan, 1993) (Fig. 23). The foreign phenocrysts (xenocrysts and antecrysts) may not be in equilibrium with the surrounding melt and undergo resorption. If the crystals are close enough, their mingled supersaturated melt zones may combine and precipitate new mineral phases that join the crystals together (Fig. 13). Another idea for glomerocryst formation is new crystal growth on the face on and existing crystal due to localized supersaturation condition in the melt that may or may not be due to resorption of the existing crystal (Vernon, 2004).

In the CHDF rhyolites, glomerocrysts are found in the glassy matrix and in FMEs and MMEs (Figs. 17, 25, and 34). Some of the glomerocrysts have crystals that are joined together along flat crystal faces and other glomerocrysts have crystals joined together along resorbed surfaces. In the glomerocrysts where plagioclase is mantled by sanidine, both types are observed (Figs. 13 and 23). However, some of the plagioclase- sanidine glomerocrysts may not be just sanidine mantling plagioclase. Some are observed to have plagioclase on the outside of the mantling sanidine and in the same optical plane as the mantled plagioclase (Fig. 22). This suggests that these particular glomerocrysts grew together and not as a pre-existing plagioclase with new growth of sanidine surrounding it.

Microlites are formed during degassing during magma ascent and eruption and also in magmatic enclaves where the enclave melt is rapidly cooled by the surrounding melt (Jerram and Martin, 2008). Their shapes are usually acicular due to rapid crystal

growth and increased nucleation and are in chemical equilibrium with the melt (or enclave melt) and along the rims of resorbed phenocrysts, especially in magmatic enclaves.

In the CHDF there are three types of microlites. The first are the microlites that formed during magma ascent due to degassing. These microlites are sparse in the glassy matrix and consist of mostly acicular feldspar, some with simple twins that are usually less than 10 μm long, and mafic mineral phases such as biotite, hornblende, magnetite, ilmenite, apatite, and zircon. Biotite and hornblende are not distinguishable except for their brownish high birefringence colors in cross-polarized light. In the FMEs the microlites are densely packed and consist of mainly plagioclase and hornblende and/or biotite. These microlites are of the same size as those in the glassy groundmass but have been formed as the result of sudden cooling when coming into contact with the surrounding melt or degassed when introduced into the surrounding melt due to differences in volatile content. In the MMEs microlites consist of plagioclase and biotite/hornblende. These are densely packed around the xenocrysts of the MMEs with the acicular plagioclase microlites showing evidence of twinning and some have swallowtail end. The MME microlites are larger than those in the surrounding melt and FMEs and show evidence of extinction in cross-polarized light that is not seen in microlites of the felsic melt.

Granophyric intergrowths occur in one sample (need sample number) with quartz and alkali feldspar, which is due to the melt being on the cotectic in the Or-Ab-Qz system (Vernon, 2004). The cotectic is the temperature where the melt is saturated with quartz and alkali feldspar at particular water content and both mineral phases crystallize together

(Vernon, 2004). Experiments suggest that while being consistent with cotectic crystallization, granophryic intergrowths can also form by simultaneous precipitation driven by rates of diffusion and growth in melt adjacent to the intergrowths (Vernon, 2004). Another interpretation of the intergrowths is that slow diffusion of Al in a feldspar crystal causes Si to increase, leading to local precipitation of quartz and that results in feldspar saturation and alternating precipitation of quartz and feldspar (Vernon, 2004).

The paragenetic interpretation of the phenocryst cargo in the topaz rhyolites of the CHDF separates the phenocrysts into three populations that formed in different parts of the magma reservoir and in mafic magma from magma mixing events (Fig. 62):

1. The first population is the formation of phenocrysts were in equilibrium with the melt prior to and during the eruption. These autocrysts are euhedral or boxy cellular and do not exhibit evidence of resorption after formation. Microlites in the surrounding melt formed during the degassing phase of magma ascent and do not form around the autocrysts, again signifying that no resorption occurred.
2. The second population of phenocrysts formed are antecrysts that formed in other locations of the magma reservoir and were transported to the eruptible magma location by various processes, whether by convection of the melt in the reservoir, injection of mafic magma into the reservoir, or another process. These antecrysts have embayments on flat crystal planes, rounded corners due to resorption, or have extreme embayments internal to the crystals. These last antecryst types are observed to show physically separate crystals of the same type that have the same crystallographic orientation. The antecrysts are found in the melt or in felsic magmatic enclaves where there are dense aggregates of plagioclase and mafic

microlites with either diffuse or sharp boundaries.

3. The third population of phenocrysts are xenocrysts that come from and are in mafic magmatic enclaves. These xenocrysts consist of olivine with and without reaction rims of biotite, long, tabular plagioclase with well defined albite twinning and most with resorption or spongy cellular textures, and rare pryoxene with hornblende reaction rims.

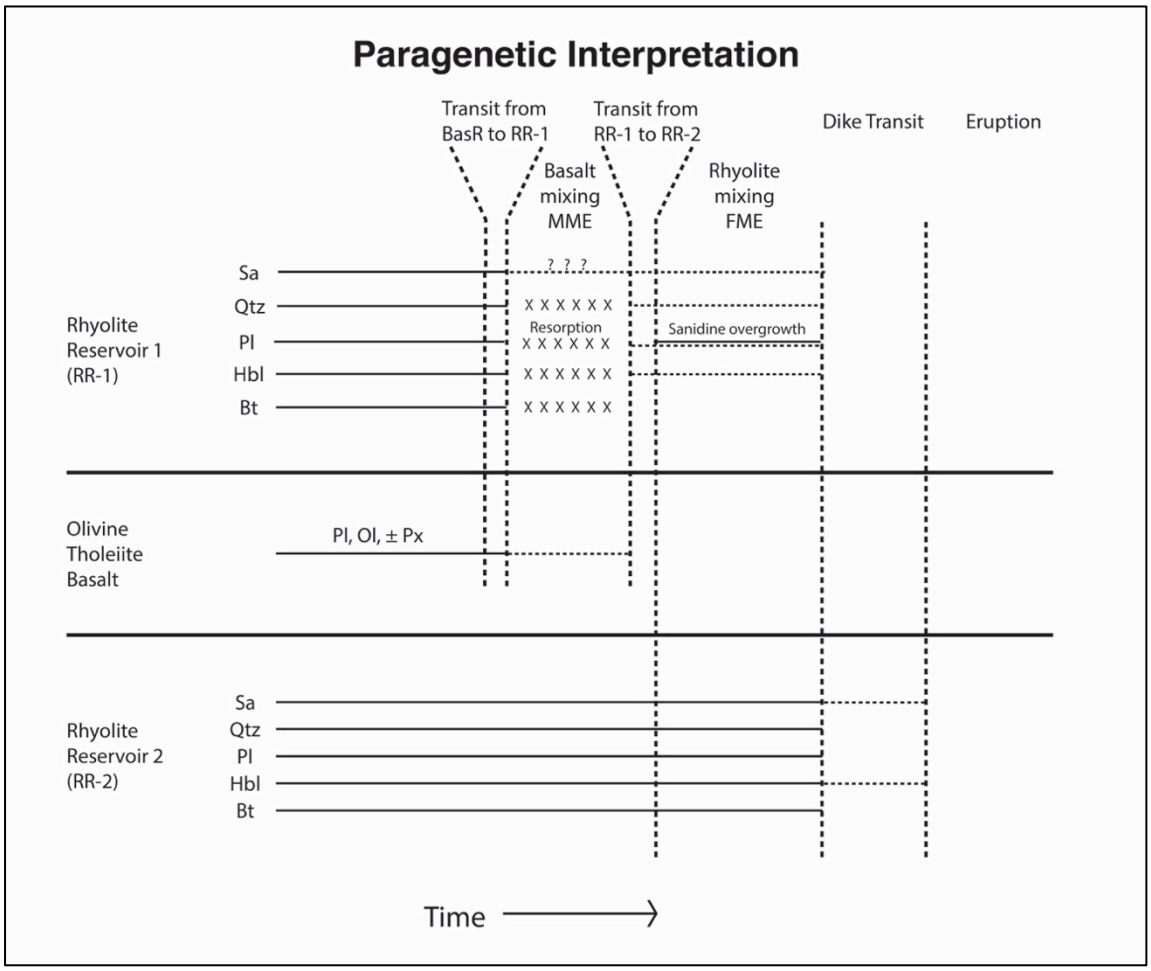

Figure 62. Paragenetic interpretation of phenocryst formation in the BVF rhyolites of the CHDF. Abbreviations: Sa – sanidine; Qtz – quartz; Pl – plagioclase; Hbl – hornblende; Bt – biotite; Ol – olivine; and Px – pyroxene. There are two high melt rhyolite reservoirs (RR-1 and RR-2) with olivine tholeiite basalt magma intrusion (BasR) into RR-1. The first rhyolite reservoir precipitates the same mineral phases as the second reservoir indicated by solid horizontal lines (Sa, Qtz, Pl, Hbl, and Bt). The basalt magma intrusion precipitates Pl, Ol, ± Px also represented by solid horizontal lines. Dotted lines represent

microlite mineral phase precipitation for RR-2 during dike transit and degassing, possible mineral phase resorption for RR-1 during rhyolite mixing into RR-2, and possible resorption of mineral phases and/or new growth for mafic magma mixing with rhyolite magma in RR-1, and **XXX**'s represent possible resorption of mineral phases during basalt-rhyolite mixing in RR-1. Felsic mineral phases are precipitated in RR-1 and RR-2. Basaltic magma intrudes into RR-1, causing MMEs to form and resorption of mafic mineral phases in BasR and felsic mineral phases within RR-1. Magma from RR-1 and BasR are transported into RR-2, forming FFEs (from RR-1 magma), further alteration events of mineral phases in RR-1 and RR-2 magmas, and sanidine to form around plagioclase phenocrysts, which may form the basis for magma from RR-2 to ascend. Degassing occurs in the ascending magma, causing microlites to form and alteration of RR-2 mineral phases may occur until eruption of the magma.

4.2 Rhyolite-MELTS Modeling to Determine Crystallization Sequences and Timing of COM-Cedar Butte Trend

Rhyolite-MELTS modeling simulates liquidus temperatures ~40°C higher than experimental liquidus temperatures, mainly due to how water affects the composition (Gardner et al., 2014 and Gualda and Ghiorso, 2012). Rhyolite-MELTS modeling also simulates mineral phases that do not precipitate in the observed order and not in the same proportions as in experimental observations (Gardner et al., 2014). Workers accept these limitations since the modeling is not intended to replicate experimental or observed conditions (need references).

In rhyolite-MELTS simulations using the 100D3 composition of Whitaker et al. (2008), liquidus temperatures are ~60°C higher than experimental temperatures. This may be because of the water content proscribed by the experimental data and how it affects the composition for the experimental pressure (Ghiorso, 2016, personal communication). Ca-Al-TI-rich clinopyroxene precipitating from the 100D3 composition is also due to higher water content (Ghiorso, 2016, personal communication). Rhyolite-MELTS modeling of the parent magma composition crystallization experiments from

Whitaker et al. (2008) (ICCP123-260) has a 1.77 wt.% H_2O that approximates the experimentally derived 1.8 wt.% H_2O. The water content was verified in the experiments by the procedure used to produce the synthetic composition and micro-FTIR measurements (Whitaker et al., 2008).

Another aspect of what mineral phases, especially clinopyroxene phases, is how fO_2 was controlled in the Whitaker et al. (2008) experiments. While I operated the rhyolite-MELTS model simulations in an unbuffered closed system, Whitaker et al. used the graphite crucibles to control fO_2 that maintained fugacity between -1.8 and -2.6 log units below FMQ (2008). I used QFM-2 in rhyolite-MELTS to perform the redox reactions to calculate Fe_2O_3 and FeO from FeO_{tot} of the 100D3 composition. This also may have affected the differing types of clinopyroxene produced by the simulation where I observed the Ca-Al-Ti-rich clinopyroxene precipitated in the model while not being produced by the experiments of Whitaker et al. (2008).

In the crystallization experiments of Whitaker et al. (2008) mineral phases precipitated between 1100°C and 1040°C, the first and second data points in their experiments (Fig. 46). Clinopyroxene was the dominant phase formed early but is quickly overtaken by plagioclase by 1000°C. Plagioclase is then the dominant phase produced in the experiments. Olivine is produced early (1040°C) and increases then decreases in content for the rest of the experiment, but is observed in all experiments. Ilmenite is precipitated early and peaks at 7.5% of the total assemblage at 940°C. In the equilibrium crystallization (EC) and fractional crystallization (FC) rhyolite-METLS simulations of the synthetic trachybasalt of Whitaker et al. (2008), ilmenite is produced early (1160°C) but not in the same amounts as in the experiments (2.31% in EC and 4.02% in FC) (Figs.

47 and 48). Ulvöspinel is produced in the simulations at 1100°C, peaks at 1020°C (3.18%) in the EC simulation and at 940°C (3.47%) in the FC simulation and is not produced at all in the experiments (Figs. 47 and 48). The amount of ulvöspinel and ilmenite in the simulations is larger than the amount of ilmenite in the experimental data explains the depletion of TiO_2 relative to SiO_2 (Fig. 38).

Apatite formation is at 1100°C in both in EC and FC simulations compared to 1000°C in the experimental data and the amounts are comparable to the Whitaker et al. (2008) data (Figs. 47 and 48). This does not explain however the enrichment in P_2O_5 in the simulations vs. SiO_2 instead of depletion in the experimental data (Fig. 45).

Orthopyroxene is not formed in the EC or FC simulations while it is observed at the end of the experimental data of Whitaker et al. (2008) (Fig. 46). Clinopyroxene is produced in all three data sets but in larger amounts in the simulations than the experimental data (Figs. 46, 47, and 48). Only one version of clinopyroxene (augite) is produced in the experimental data, but three versions of clinopyroxene are produced in the simulations. In the EC rhyolite-MELTS simulation, augite (Ca-Mg-Fe-rich) is produced at 1100°C only and then pigeonite (Mg-Fe-Ca-rich) and the Ca-Al-Ti-rich clinopyroxene are produced from 1080°C onwards (Fig. 47). This could be because of the high water content for basalt that would produce the Ca-Al-Ti-rich clinopyroxene (Ghiorso, 2016, personal communication).

Plagioclase forms relatively late at 1040°C and in lesser amounts than in the experimental data (17.37% EC and 21.27% FC vs. 44.0% at 940°C) (Figs. 47 and 48). Plagioclase in Whitaker et al. (2008) decreases from An_{55} to An_{45} from 1040°C to 940°C. In the EC rhyolite-MELTS simulation, plagioclase decreases from An_{61} to An_{47} from

1040°C to 940°C but only for 0.64% to 17.37% in the EC simulation compared to 3.2% to 44.0% in the experimental data. In the FC rhyolite-MELTS simulation, plagioclase decrease from An_{63} to An_{47} from 1040°C to 940°C and amounts from 3.27% to 21.27% in the same temperature range. This explains the enrichment of Al_2O_3, CaO, and Na_2O vs. SiO_2 compared to the experimental data of Whitaker et al. (2008) (Figs. 39, 42, and 43). Al_2O_3 does not decrease vs. SiO_2 until 55 wt.% SiO_2 with the first formation of plagioclase instead of the nearly flat linear trend of the experimental data (Fig. 39). CaO decrease in a flat linear trend vs. SiO_2 compared to the curved linear trend of the experimental data (Fig. 42). Na_2O increases at steeper rate vs. SiO_2 compared to the flatter slope of the experimental data and can be explained by the lower amounts and later precipitation temperatures of plagioclase in the rhyolite-MELTS simulations (Fig. 43).

In the FC rhyolite-MELTS simulation a similar mineral phase assemblage is produced compared to the EC simulation (Figs. 47 and 48). The temperatures and sequences of mineral phase formation is the same for the EC simulation except for the formation of olivine at 1000°C. Another difference is that ilmenite is not formed between 1100°C and 1000°C, augite forms only at 1100°C, pigeonite stops forming at 1040°C and the Ca-Al-Ti-rich clinopyroxene stops forming at 1020°C (Fig. 48).

The amounts of clinopyroxene in formed in FC simulation comes to ~35% which is more than 23.5% formed in the experimental data and less than the ~42.50% formed in the EC simulation (Figs. 46, 47, and 48). The other difference between the EC simulation and the equilibrium crystallization of the experiments of Whitaker et al. (2008) is that formation is over a shorter temperature range for the fractional crystallization simulation.

Are the rhyolite-MELTS simulations of EC and FC consistent with the

crystallization experiments of Whitaker et al. (2008)? Simulation liquidus temperatures are ~60°C higher than experimental liquidus temperatures but is consistent with work by Gardner et al. (2014). Also mineral phase formation temperatures and amounts are not the same as in Whitaker et al. (2008) but are also consistent with Gardner et al. (2014). Despite the differences using rhyolite-MELTS for modeling the evolution of a basaltic parenetal magma to produce rhyolitic magma is plausible.

4.3 Magma Chamber Simulator Modeling to Determine Crystallization Sequences and Timing of Bimodal BVF

During the modeling process with MCS, many different changes to the starting parameters were required to have a simulation proceed to equilibrium conditions. With FmZero at the default setting of 0.08, wallrock water content needed to be adjusted downward to have MCS find the wallrock solidus. An initial H_2O wt.% of 1.0 was selected because of the assumption of biotite and or hornblende present in the country rock. The felsic granodiorite composition of the Archean upper crust was selected from Rudnick and Gao (2003). A pressure range was determined by using the cross sections of Royse et al. (1975) to determine rock units and depths to the decollement of the Sevier thrust belt, densities of those rock units from Mabey and Oriel (1970) (Fig. 63) and density of the upper crust and depth to the lower crust from DeNosaquo et al. (2009) (Fig. 3).

The working model parameters for MCS were to have Archean upper crust H_2O wt.% at 0.9 for the higher pressure (4730 bars) and 1.2 wt.% for the lower pressure (3900 bars) (Table 8). The amount of wallrock melt before anatectic melt migration occurs works for FmZero between 0.08 and 0.11. The only lower pressure used for MCS

simulations was 3900 bars because of time limitations of finishing modeling prior to writing this paper.

While the thermodynamic models of MCS using the KEP-004 composition of Pickett (2004) in this paper simulate trends of fractional crystallization of COM-Cedar Butte and the crystallization experiments of Whitaker et al. (2008) with regards to wt.% TiO_2, MgO, and CaO vs. SiO_2, the models do not simulate fractional crystallization trends in whole or in part with regards to wt.% Al_2O_3, FeO_{tot}, Na_2O, K_2O, and P_2O_5 vs. SiO_2. Similarly, the rhyolite-MELTS simulation using KEP-004 in the fractional crystallization mode follows the COM-Cedar Butte trend and Whitaker et al. (2008) experiments with regards to wt.% MgO vs. SiO_2 only and does not follow the fractional crystallization trends for the rest of the major oxides vs. SiO_2. TiO_2 and CaO vs. SiO_2 parallel the fractional crystallization trends but below them while Al_2O_3 vs. SiO_2 mimics the rhyolite-MELTS trends of 100D3 of Whitaker et al. (2008) but more extreme enrichment vs. SiO_2.

MCS modeling of the "primitive" olivine tholeiite basalt of the BVF (KEP-004) show that it is possible to produce rhyolitic compositions at mid-crustal and shallow crustal depths in the Archean felsic upper crust. Using temperature gradients of 25°C/km of Brott et al. (1981) and 35°C/km of Blackwell (1989) show that 14.29-29.66% wallrock assimilation occurs until equilibrium conditions with the magma at mid-crustal pressures of 4.73 kbar (18.3 km) (Table 9). At lower pressures (3.9 kbar or 16.1 km) MCS modeling produces wallrock assimilation in the range of 19.75-21.26% with the higher temperature gradient (35°C/km) (Table 9). This is lower than the range of assimilation wallrock based on Nd- and Sr-isotopic ratios of crustal xenoliths of Ford (2005) of 30-

45% assimilation from the most primitive basalt of the BVF (KEP-004) (Fig. 7).

4.4 Conceptual Model of the China Hat Magma System

The determination of setting the location of the upper magma reservoir (Fig. 64) is based on work on the structure of the Sevier fold and thrust belt in southeast Idaho (Dixon, 1982; Mabey and Oriel, 1970; Royse et al., 1975) (Fig. 4). Combining the structure data and seismic velocity profiles from the 1980's onward (Pankratz and Ackerman, 1981; Peng and Humphreys, 1998; DeNosaquo et al., 2008), the depth, density, and pressure increments of the various rock units were calculated taking into consideration the tectonic structure in the area (Table 9).

With the Neoproterozoic rock units identified as quartzite that are denser than the upper crust it overlies and denser than the overlying Paleozoic and Mesozoic carbonates and sandtones and the determination of upper crustal Archean xenoliths present in the ESRP (Table 9 and Appendix 1), the placement of an upper magma reservoir in the upper crust is calculated to be below 12 km in depth. Any shallower, the magma would have to interact with the cold quartzite and the magma would loose too much thermal energy to retain enough energy to become eruptible. Also the Sr- and Nd-isotopic ratios of crustal xenoliths are from the Archean upper crust which coincides with the presence of the Archean Wyoming Craton in SE Idaho and not having the upper crust consisting of Proterozoic or Paleozoic miogeoclinal sediments (Fig. 6 and Table 9).

Therefore, the conceptual diagram of the probable location and structure of the magma reservior for the China Hat magma system is presented in Figure 66. The reservoir is at the base of the Neoproterozoic quartzites at ~12 km and extends at least 4-5 km deeper into the crust based on hornblende geobarometery between pressures of

3100 and 3900 bars. The reservoir is made of high melt zones (HMZ) with melt > 50% volume, low melt zones (LMZ) with melt < 50% volume, subsolidus cumulate zones, and magma recharge zones (MRZ) where magma mixing and the generation of mafic magmatic enclaves occur. Magma recharge comes from MASH/AFC reservoirs deeper in the crust or from mantle-derived magma (olivine tholeiite basaltic compositions) where magma moves via dikes and erupts on the surface or intrudes into the shallow magma reservoir (Fig. 65). In the MRZ's, more mafic magma mixes with the surrounding felsic magma and becomes hybridized or forms mafic magmatic enclaves (MME) that are suspended in the felsic magma. The MMEs if formed in a HMZ, may disturb the surrounding melt and be one cause that forces the movement of the disturbed magma to another HMZ or to erupt. The disturbed melt carries MMEs and it's own phenocryst cargo to another HMZ where, if a difference in temperature exists, cause the formation of felsic magmatic enclaves (FME) or a mixing of phenocrysts with surrounding melt and phenocrysts (Fig. 65). This disturbs the current HMZ and wether from overpressurization, oversaturation of volatiles, or some other process, causes the magma to ascend to degass and erupt (Fig. 65).

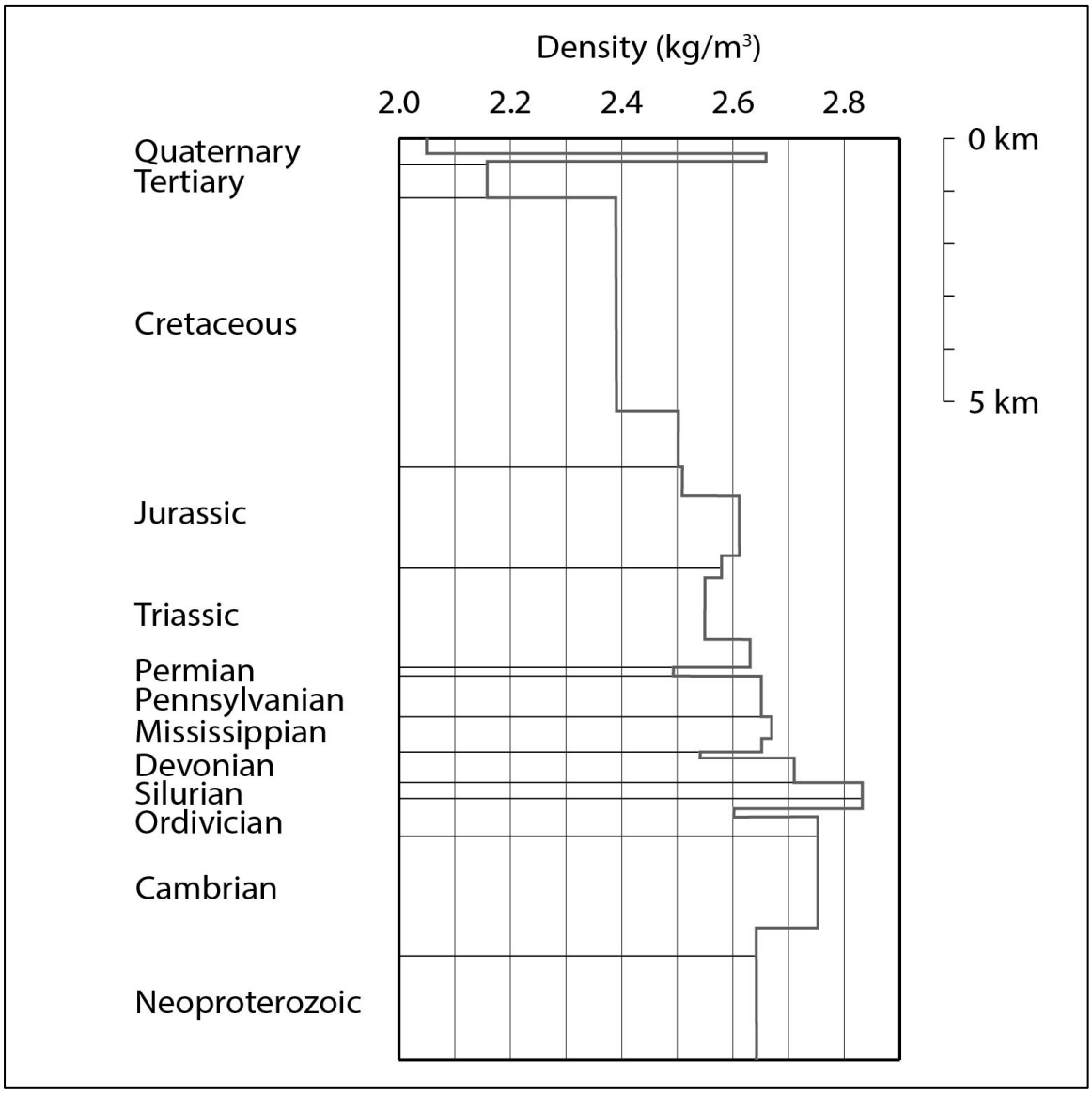

Figure 63. Density vs. depth chart of Paleozoic to Cenozoic sedimentary and volcanic rock units in the Soda Springs-China Hat graben. Approximate depths of each unit in succession are in km and densities are in kg/cm^3. Modified from Mabey and Oriel (1970) Fig. 2.

Table 9. Depths and densities of rock units in the Soda Springs-China Hat Graben. Data from DeNosaquo et al. (2008), Mabey and Oriel (1970), and Royse et al. (1975).

Rock Unit	Depth (meters)	Density (g/cm^3)	Pressure (bars)	Total Pressure (bars)	Total Depth (meters)
QTb	200	2.26	44	44	200
Ts	1350	2.16	286	330	1550
Trs	550	2.58	139	470	2100
PPs	800	2.62	206	675	2900
Ms	1050	2.66	274	949	3950
DOs	1100	2.73	295	1244	5050
~~C~~s	950	2.70	252	1495	6000
Ms	300	2.66	78	1574	6300
DOs	1050	2.73	281	1855	7350
~~C~~s	1250	2.70	331	2186	8600
Zm	2600	2.64	673	2859	11200
AFUC (from bottom of Zm)	920	2.67	241	3100	12120
	1682	2.67	441	3300	13802
	2445	2.67	640	3500	14565
	3209	2.67	841	3700	15329
	3972	2.67	1040	3900	16092
	7140	2.67	1870	4730	18340
AMLC-Moho	19660	3.00	5786	10515	38980

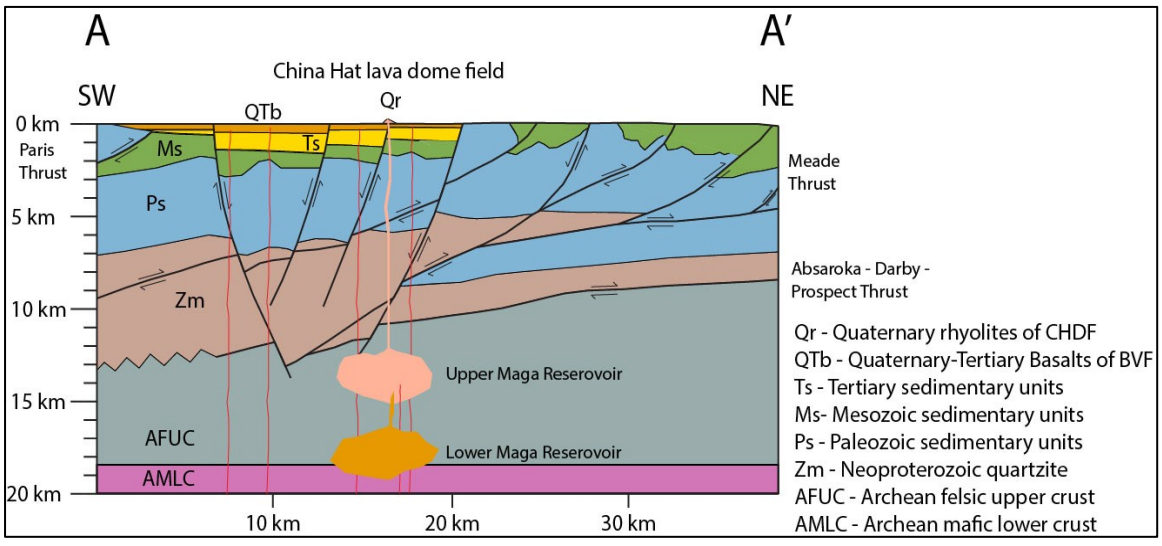

Figure 64. Cross-section of the BVF showing structure in the graben down to UC- LC boundary. Direction of cross-section is from the SW to NE going through the CHDF. Modified from Dixon (1982) and Welhan et al. (2014) Fig. 2.

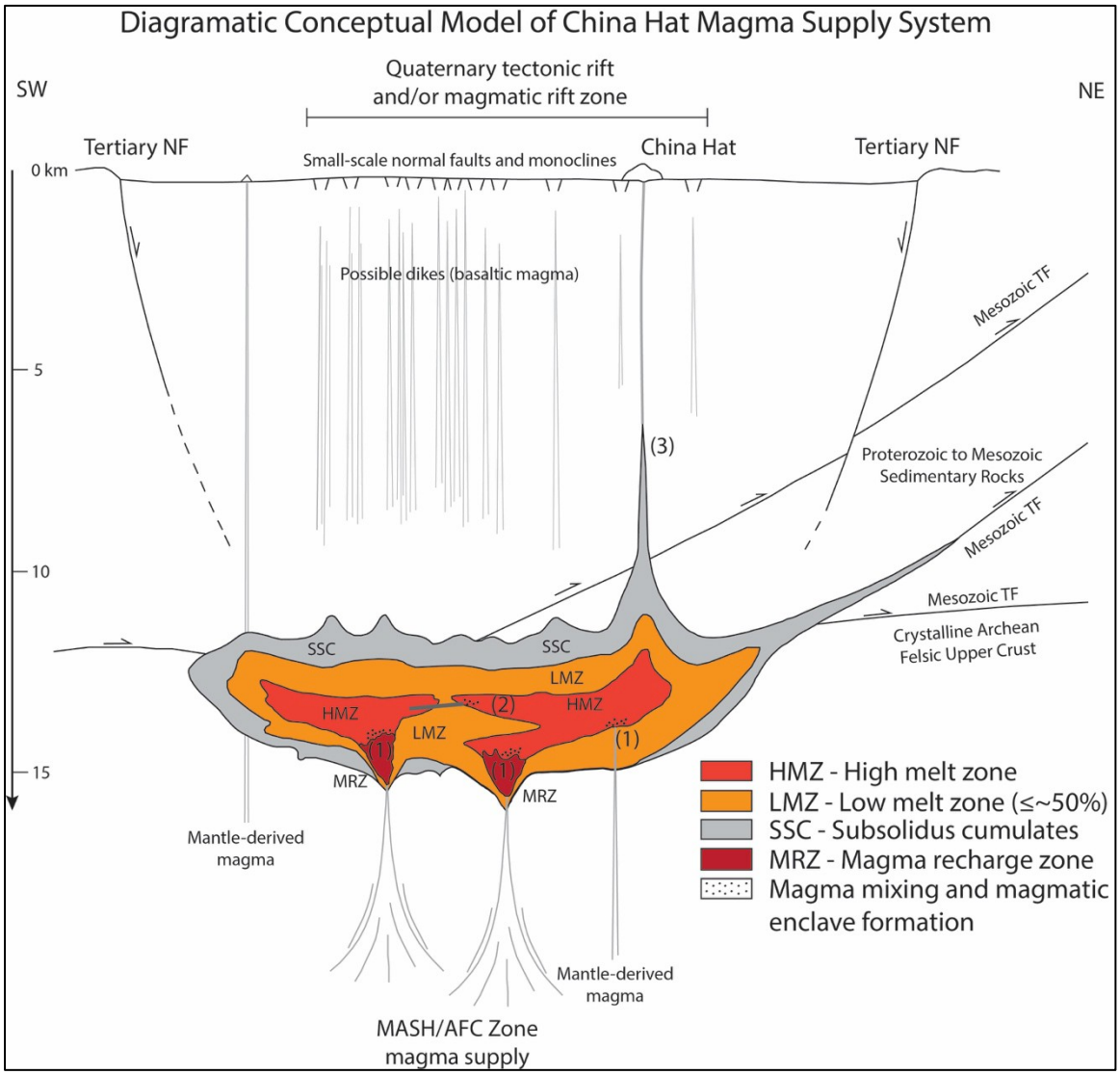

Figure 65. Conceptual model of the China Hat magma supply system. The numbers 1-3 indicate zones of generation or alteration of phenocrysts occur in the reservoir. 1) magma mixing zone with mafic magma and original rhyolitic magma. 2) magma transport of rhyolitic and mafic magma from one HMZ to another HMZ. 3) ascent and eruption of magma from a disturbed HMZ after intrusion of melt from another HMZ or mafic melt injection. From McCurry and Welhan (2014) Fig. 6.

Chapter 5

CONCLUSIONS

Various hypotheses are presented for testing. For the phenocryst cargo of the rhyolites, the phenocryst mineral phases are identified and textures are interpreted to constrain the paragenesis of the phenocrysts. Then, thermodynamic modeling of a parental magma composition simulates various evolutionary paths to further constrain plausible scenarios of how rhyolites are produced from basaltic melts without observing the intermediate compositions produced but not erupted in the China Hat lava dome field.

The hypotheses proposed in this paper are fractional crystallization (FC) of a basaltic melt, equilibrium crystallization (EC) of the same basaltic melt, fractional crystallization and wallrock assimilation (AFC) of the basaltic melt, and partial melting of the felsic Archean upper crust to produce an eruptible melt. The scenarios used in modeling in this paper are the FC and EC paths for simulating the evolution of a synthetic trachybasalt composition of Whitaker et al. (2008), FC and AFC paths for simulating the evolution of the most primitive olivine tholeiite basalt of the BVF (Pickett, 2004). The partial melting of felsic Archean upper crust hypothesis is rejected due to previous work and not considered in this paper (Ford, 2005).

The paragenesis of the phenocryst cargo of the China Hat lava dome field (CHDF) rhyolites is more complicated than previous workers hypothesized (Dayvault et al., 1984 and Ford, 2005). Previous work interpreted the phenocryst cargo as being in textural and chemical equilibrium with the surrounding melt prior to eruption and any embayments occurring because of magma ascent (Dayvault et al., 1984 and Ford, 2005). I propose that there are a number of populations of phenocrysts that consist of autocrysts

in equilibrium with surrounding melt in a high melt zone (HMZ), antecrysts of the same type of mineral phases as autocrysts that form in other high melt zones, and a population of xenocrysts from more mafic magma that is injected into the magma reservoir.

In describing and interpreting the textures of the phenocryst cargo, the magma system for the CHDF has a number of HMZs where phenocrysts are mobile within the melt. Pressure or temperature transients from the injection of magmas foreign to the reservoir disturb one or more HMZs cause the movement of melt from those zones to new HMZs that ultimately lead to the eruption of the lava domes. The evidence for this is the presence of felsic magmatic enclaves with a near identical phenocryst cargo as the surrounding melt, mafic magmatic enclaves that are evidence of mafic magma recharge into the magma reservoir, and resorption textures on felsic and mafic phenocrysts that are evidence of changes in saturation in the melt that cause alteration to phenocrysts in the melt.

The mixed textural populations of phenocryts in the melt during eruption suggests mixing from different/distinct but generally related magma sources and subsequent homogenization of the liquid phase. If there was mixing of different populations of phenocrysts without wholesale resorption where the resorbed phenocrysts were located, then mixing occurring shortly prior to eruption. Work on melt inclusions in euhedral and resorbed phenocrysts for the determination of pressure or temperature barometers at crystal formation is required to further constrain the timeline of the eruption.

Also, the presence of oviodal- or ellipsoidal-shaped magmatic enclaves is evidence of magma transport within the magma reservoir prior to eruption. The felsic magmatic enclaves (FMEs) have phenocrysts and microlites that have the same mineral

phases as those phenocrysts that are in the surrounding melt and I interpret that to mean FMEs come from other HMZs and produce microlites and resorption features on phenocrysts due to changes in P-T conditions that change the equilibrium of the FMEs.

Mafic magmatic enclaves (MMEs) are evidence of more mafic magma being introduced into HMZs in the magma reservoir. MMEs are ovoidal in shape with sharp boundaries or show evidence of hybridization with surrounding melt. I interpret MMEs as being xenocrysts with or without reaction rims with microlites surrounding them due to becoming chilled due to lower temperatures in the surrounding melt. Those MMEs that are elongate ovoidal in shape I interpret to being stretched due to magma movement during ascent and not to being angular-shaped xenoliths from surrounding wallrock because the mineral phases are the same as for the oviod-shaped MMEs.

The performance of thermodynamic modeling using MCS and rhyolite-MELTS is also tested my thesis. The MELTS family of software has been in use since the mid-1990's and has undergone multiple upgrades in capabilities (Ghiorso and Sack, 1995 and Ghiorso and Gualda, 2015). During the modeling, my interpretation is that while modeling liquidus temperatures are higher than experimental liquidus temepratures as seen by Gardner et al. (2014) and mineral phases do not precipitate at the same temperatures or in the same amounts as the experimental data of Whitaker et al. (2008), the same mineral phases are produced during the modeling and provides simulated evolutionary paths of parental magma through fractional crystallization and wallrock assimilation.

During fractional and equilibrium crystallization modeling of the synthetic trachybasalt of Whitaker et al. (2008) using rhyolite-MELTS total alkalis vs. silica and

the major oxides except for Al_2O_3, Na_2O, and P_2O_5 vs. SiO_2 follow the COM-Cedar Butte trend and the experimental data from Whitaker et al. (2008). The last of the three above oxides are different than the experimental and analyzed data because of the late precipitaiton of feldspar and the early precipitation of apatite compared to those mineral phases produced in the crystallization experiments of Whitaker et al. (2008).

Fractional crystallization (FC) and assimilation and fractional crystallization (AFC) modeling of the most primitive olivine tholeiite basalt (KEP-004) of Pickett (2004) using rhyolite-MELTS and MCS, respectively. The FC modeling using rhyolite-MELTS of the KEP-004 composition produced data that simulates the experimental data of Whitaker et al. (2008) and the COM-Cedar Butte trend only for MgO and CaO vs. SiO_2 and SiO_2, CaO, and partially TiO_2 and K_2O vs. MgO. The other oxides are either above the experimental and analytic data (total alkalis, Al_2O_3, Na_2O, and K_2O vs. SiO_2 and Al_2O_3 and Na_2O vs. MgO) or below (TiO_2 and FeO_{tot} vs. SiO_2 and FeO_{tot} vs. MgO) and P_2O_5 vs. both SiO_2 and MgO does not follow any trend of experimental or analytical data.

AFC modeling of the KEP-004 composition with 28% wallrock assimilation in the data presented produced data that simulates the experimental and analytical data more closely than FC-only modeling. The major oxides Na_2O+K_2O, TiO_2, MgO, and CaO vs. SiO_2 produced from the AFC modeling simulates the experimental and analytical data. The major oxides Al_2O_3, Na_2O, and K_2O vs. SiO_2 produced from the AFC modeling are above the experimental and anlytical data. The major oxide FeO_{tot} vs. SiO_2 produced from the AFC modeling is below the experimental and analytical data with P_2O_5 vs. SiO_2 not following any of the data. The early precipitation of apatite may explain the P_2O_5

simulation data and the late precipitation of feldspar may explain the higher Al_2O_3 simulation data. Total FeO is low vs. SiO_2 because AFC simulations of KEP-004 used the fO_2 buffer QFM that was determined using Mg/Mn concentrations in magnetite and ilmenite that track along QFM (Ford, 2005). In contrast to the FC simulation using the synthetic trachybasalt of Whitaker et al. (2008) that uses a QFM-2 and tracks with the experimental data. Further AFC simulation using an fO_2 buffer < QFM should be used for the KEP-004 composition.

Future work based on the results of this paper pertain to the phenocryst cargo and the thermodynamic modeling of parental magma compositions based on the most primitive olivine tholeiite basalts of the BVF. Further work regarding the paragenesis of the phenocryst cargo is required by analyzing melt inclusions in quartz phenocrysts and analyzing a wider range of phenocrysts with euhedral and subhedral textures to determine when such phenocrysts were precipitated with regards to bulk composition and timing during the eruptive cycle. Also, testing of a multi-source model for different textural populations with more detailed clean analysis of phenocrysts and evaluation of exchange equilibria.

Further thermodynamic modeling of parental magma compositionsis requried to constrain the intial water content of parental magma and wallrock compositions, pressures with regards to possible magma reservoir locations in the upper crust, and expanding the range of parental magma compositions to model the source of the mantle-derived melts that are presumed to be the source of the olivine tholeiite basalts observed in the BVF.

REFERENCES

Autenrieth, K. D., McCurry, M., Welhan, J., and Polun, S., 2011, Conceptual Subsurface Model of the Blackfoot Volcanic Field, Southeast Idaho: A Potential Hidden Geothermal Resource: GRC Transactions, v. 35, p. 695-698.

Blackwell, D. D., 1989, Regional implications of heat flow of the Snake River Plain, Northwestern United States: Journal of Geophysical Research, v. 164, p. 323-343.

Bohrson, W. A. and Spera, F. J., 2003, Energy-constrained open-system magmatic processes IV: Geochemical, thermal and mass consequences of energy-constrained recharge, assimilation and fractional crystallization (EC-RAFC): Geochemistry Geophysics Geosystems, v. 4, no. 2, p. 1-25.

Bohrson, W. A., Spera, F. J., Ghiorso, M. S., Brown, G. A., Creamer, J. B., and Mayfield, A., 2014, Thermodynamic Model for Energy-Constrained Open-System Evolution of Crustal Magma Bodies Undergoing Simultaneous Recharge, Assimilation and Crystallization: the Magma Chamber Simulator: Journal of Petrology, v. 55, no. 9, p. 1685-1717.

Breckenridge, R. M., Lewis, R. S., Adema, G. W., and Weisz, D. W., 2003, Miocene and Younger Faults in Idaho: Idaho Geological Survey, scale 1:1,000,000.

Brott, C. A., Blackwell, D. D., and Ziagos, J. P., 1981, Thermal and tectonic implications of heat flow in the Eastern Snake River Plain, Idaho: Journal of Geophysical Research, v. 86, p. 11709-11734.

Christiansen, E. H., Burt, D. M., Sheridan, M. F., and Wilson, R. T., 1983, The petrogenesis of topaz rhyolites from the western United States: Contributions to Mineralogy and Petrology, v. 83, p. 16-30.

Christiansen, E. H., Sheridan, M. F., and Burt, D. M., 1986, The Geology and Geochemistry of Cenozoic Topaz Rhyolites from the Western United States: Geological Society of America Special Paper, v. 205, 82p.

Christiansen, E. H. and McCurry, M., 2008, Contrasting origins of Cenozoic silicic volcanic rocks from the western Cordillera of the United States: Bulletin of Volcanology, v. 70, p. 251-267.

Colón, D. P., Bindeman, I. N., Ellis, B. S., Schmitt, A. K., and Fisher, C. M., 2015, Hydrothermal alteration and melting of the crust during the Columbia River Basalt-Snake River Plain transition and the origin of low-$\delta^{18}O$ rhyolites of the central Snake River Plain: Lithos, v. 224-225, p. 310-323.

Dayvault, R. D., Rush, S. M., and Ludlum, J. R., 1984, Evaluation of Uranium Potential in a Topaz-Bearing Rhyolite, China Hat Dome, Southeastern Idaho: in Goodknight, C. S., ed., Reports on Field Investigations of Uranium Anomalies (Report GJBS-1 (84)), Grand Junction, U. S. Department of Energy, p. 1-26.

DeNosaquo, K. R., Smith, R. B., and Lowry, A. R., 2009, Density and lithospheric strength models of the Yellowstone-Snake River Plain volcanic system from gravity and heat flow data: Journal of Volcanology and Geothermal Research, v. 188, p. 108-127.

Dixon, J. S., 1982, Regional structural synthesis, Wyoming salient of Western Overthrust belt: American Association of Petroleum Geologists Bulletin, v. 66, no. 10, p. 1560- 1580.

Fiesinger, D. W., Perkins, W. D., and Puchy, B. J., 1982, Mineralogy and Petrology of Tertiary-Quaternary Volcanic Rocks in Caribou County, Idaho: in Bonnichsen, B.

and Breckenridge, R. M., eds., Cenozoic Geology of Idaho: Idaho Bureau of Mines and Geology Bulletin, v. 26, p. 465-488.

Ford, M. T., 2005, The petrogenesis of Quaternary rhyolite domes in the bimodal Blackfoot Volcanic Field [M.S. Thesis]: Pocatello, Idaho State University, 133 p.

Ganske, R. R., 2006, The geology and petrology of the East Butte area, Bingham County, Idaho [M.S. Thesis]: Pocatello, Idaho State University, 153 p.

Ghiorso, M. S. and Sack, R. O., 1995, Chemical mass transfer in magmatic processes IV. A revised and internally consistent thermodynamic model for the interpolation and extrapolation of liquid-solid equilibria in magmatic systems at elevated temperatures and pressures: Contributions to Mineralogy and Petrology, v. 119, p. 197-212.

Ghiorso, M. S. and Gualda, G. A. R., 2015, An H_2O-CO_2 mixed fluid saturation model compatible with rhyolite-MELTS: Contributions to Mineralogy and Petrology, v. 169, no. 53, p. 1-30.

Goldsby, R. C., McCurry, M., and Lochridge, W., 2015, Preliminary Characterization of Mafic Magmatic Enclaves in 57ka Topaz Rhyolite Lava Domes in the Blackfoot Volcanic Field, SE Idaho: Geological Society of America Abstracts with Programs, v. 47, no. 6, p. 26.

Gualda, G. A. R., Ghiorso, M. S., Lemons, R. V., and Carley, T. L., 2012, Rhyolite-MELTS: A modified calibration of MELTS optimized for silica-rich, fluid-bearing magmatic systems: Journal of Petrology, v. 53, no. 5, p. 875-890.

Hayden, K. P., 1992, The geology and petrology of Cedar Butte, Bingham County, Idaho [M.S. Thesis]: Pocatello, Idaho State University, 104 p.

Heumann, A., 1999, Timescales of processes within silicic magma chambers [Ph.D. Thesis]: Amsterdam, Vrije University, 200 p.

Jerram, D. A. and Martin, V., 2008, Understanding crystal populations and their significance through the magma plumbing system: in Annen, C. and Zellmer, G.F. eds., Dynamics of Crustal Magma Transfer, Storage and Differentiation, London, Geological Society, Special Publications, v. 304, p. 133-148.

Kuntz, M. A., Covington, H. R., and Schorr, L. J., 1992, An overview of basaltic volcanism of the eastern Snake River Plain, Idaho: Geological Soceity of America Memoir, v. 179, p. 227-267.

Leeman, W. P., 1982b, Evolved and Hybrid Lavas from the Snake River Plain, Idaho, in Bonnichsen, B. and Breckenridge, R.M. eds., Cenezoic Geology of Idaho: Moscow, Idaho, Idaho Bureau of Mines and Geology Bulletin, v. 26, p. 193-202.

Leeman, W. P. and Harry, D.L., 1993, A Binary Source Model for Extension-Related Magmatism in the Great Basin, Western North America: Science, v. 262, no. 5139, p. 1550-1554.

Mansfield, G. R., 1927, Geography, geology, and mineral resources of part of southeastern Idaho: U. S. Geological Survey Professional Paper, v. 152, 453 p.

Mabey, D. and Oriel, S., 1970, Gravity and Magnetic Anomalies in the Soda Springs Region, Southeastern Idaho: U. S. Geological Survey Professional Paper, v. 646-E, p. 1-15.

McCurry, M., Hayden, K. P., Morse, L. H., and Mertzman, S., 2008, Genesis of post-hotspot, A-type rhyolite of the Eastern Snake River Plain volcanic field by extreme fractional crystallization of olivine tholeiite: Bulletin of Volcanology, v.

70, p. 361- 383.

McCurry, M. and Rodgers, D.W., 2009, Mass transfer along the Yellowstone hotspot track I: Petrologic constraints on the volume of mantle-derived magma: Journal of Volcanology and Geothermal Research, v. 188, p. 86-98.

McCurry, M., Welhan, J., Polun, S., and Autenrieth, K., 2011, Geothermal Potential of the Blackfoot Reservoir-Soda Springs Volcanic Field: A Hidden Geothermal Resource and Natural Laboratory in SE Idaho: GRC Transactions, v. 35, p. 917-924.

McCurry, M. and Welhan, J., 2014, Do Magmatic-Related Geothermal Energy Resources Exist in Southeast Idaho?: GRC Transactions, v. 36, p. 699-707.

McCurry, M., Pearson, D., Welhan, J., Natwotniak, S. K., and Fisher, M., 2015, Origin and potential geothermal significance of China Hat and other late Pleistocene topaz rhyolite lava domes of the Blackfoot volcanic field, SE Idaho: GRC Transactions. v. 39, p. 35-48.

Morse, L. H., 2002, Basalt alteration and authigenic mineralization near the effective base of the Snake River Plain Aquifer at the Idaho National Engineering and Environmental Laboratory, Idaho [M.S. Thesis]: Pocatello, Idaho State University, 182 p.

Oriel, S. S. and Platt, L. B., 1980, Geologic Map of the Preston 1x2 Quadrangle, Southeastern Idaho and Western Wyoming: U. S. Geological Survey, Miscellaneous Investigations Series, Map I-1127, scale 1:250,000.

Pankratz, L. W. and Ackermann, H. D., 1982, Structure Along the Northwest Edge of the Snake River Plain Interpreted From Seismic Refraction: Journal of Geophysical

Research, v. 87, no. B4, p. 2676-2682.

Peng, X., and Humphreys, E. D., 1998, Crustal velocity structure across the eastern Snake River Plain and Yellowstone swell: J. of Geophysical Research, v. 103, no. B4, p. 7171-7186.

Pickett, K. E., 2004, Physical Volcanology, Petrography, and Geochemistry of Basalts in the Bimodal Blackfoot Volcanic Field, Southeastern Idaho [M.S. Thesis]: Pocatello, Idaho State University, 91 p.

Pierce, K. L. and Morgan, L. A., 2009, Is the track of the Yellowstone hotspot driven by a deep mantle plume? - Review of volcanism, faulting, and uplift in light of new data: Journal of Volcanology and Geothermal Research, v. 188, p. 1-25.

Reed, M. F., Bartholomay, R. C., and Hughes, S. S., 1997, Geochemistry and stratigraphic correlation of basalt lavas beneath the Idaho Chemical Processing Plant, Idaho National Engineering Laboratory: Environmental Geology, v. 30, no. 1/2, p. 108-118.

Royse, F., Warner, M., and Reese, D., 1975, Thrust Belt Structural Geometry and Related Stratigraphic Problems Wyoming-Idaho-Northern Utah, in Rocky Mountain Association of Geologists - 1975 Symposium, v. 1, p. 41-54.

Rudnick, R. L., and Gao, S., 2003, Composition of the Continental Crust, in Rudnick, R.L. ed., The Crust. Treatise on Geochemistry: Oxford, Elsevier-Pergamon, p. 1-64.

Smith, P. M. and Asimow, P. D., 2005, Adiabat_1ph: A new public front-end to the MELTS, pMELTS, and pHMELTS models: Geochemistry Geophysics Geosystems, v. 6, no. 1, p. 1-8.

Spear, D. B., 1979, The geology and volcanic history of the Big Southern Butte – East Butte area, Eastern Snake River Plain, Idaho [Ph.D. Thesis]: Buffalo, University of New York, 136 p.

Spera, F. J. and Bohrson, W. A., 2001, Energy-Constrained Open-System Magmatic Processes I: General Model and Energy-Constrained Assimilation and Fractional Crystallization (EC-AFC) Formulation: Journal of Petrology, v. 42, no. 5, p. 999-1018.

Van der Plas, L. and Tobi, A. C., 1965, A Chart for judging the reliability of point counting results: American Journal of Science, v. 263, p. 87-90.

Vernon, R. H., 2004, A practical guide to rock microstructure: New York, Cambridge University Press, 594 p.

Welhan, J., Gwynn, M., Payne, S., McCurry, M., Plummer, M., and Wood, T., 2014, The Blackfoot Volcanic Field, Southeast Idaho: A Hidden High-Temperature Geothermal Resource in the Idaho Thrust Belt: in Proceedings Thirty-Ninth Workshop on Geothermal Reservoir Engineering, Stanford, CA, Stanford University, Feb. 2014, p. 1-13.

Whitaker, M. L., Nekvasil, H., Lindsley, D. H., and McCurry, M., 2008, Can crystallization of olivine tholeiite give rise to potassic rhyolites? - An experimental investigation: Bulletin of Volcanology, v. 70, p. 417-434.

Appendix 1

This section contains data from previous workers that relate to current work.

Location	Sample	Sr (ppm)	$^{87}Sr/^{86}Sr$	Nd (ppm)	$^{143}Nd/^{144}Nd$	sigma
SK	73-68X	175	0.72550	22.3	0.510895	-34.0
COM	CKI-1	211	0.73359	13.5	0.510499	-41.8
COM	70-40	324	0.71525	9.8	0.510454	-42.6
COM	SI-1	70	0.71795	85.0	0.510590	-40.0
COM	COM-1	97	0.81728	9.2	0.510228	-47.1
SM	SM-2G	559	0.72092	7.1	0.509973	-52.0
SM	DM-103	310	0.73878	25.7	0.510853	-34.9
ALB	YAG-799	115	0.8060	19.0	0.511278	-26.6
ALB	YAG-800	181	0.89260	59.0	0.510675	-38.3

Table A1.1. Nd- and Sr-isotopic ratios for selected crustal xenoliths from the Snake River Plain and Albion Range. Abbreviations are: SK – Spencer-Kilgore; COM – Craters of the Moon; SM – Square Mountain; and ALB – Albion Range. All listed xenoliths are proposed to be from the Archean upper crust based on age and evolved Sr-isotopic signatures. From Ford (2005).

Sample	Rhyolites	Sr (ppm)	$^{87}Sr/^{86}Sr$ initial	±	Nd (ppm)	$^{145}Nd/^{144}Nd$ initial	±	Sigma Nd
7160101	CDF	2.2	0.710591	6	22.4	0.512080	6	-10.9
8220101	CDF	2.02	0.709523	25	21	0.512083	7	-10.8
G1	CDF	2.23	0.7097306	7	25.7	0.512130	40	-9.9
G2	CDF	2.2	0.709595	8	21.3	0.512074	5	-11
China Cap MM	CDF		0.710341	10		0.512075	5	-11
9010104	NDF	4.86	0.709354	12	26.4	0.512023	4	-12
	Basalts		(measured)			(measured)		
KEP 004	"primitive"	350	0.706646	5	26.8	0.512358	30	-5.5
KEP 027	"evolved"	350	0.708905	4	81	0.512241	17	-7.7
KEP 029	Willow Cr	375	0.707929	5	16.8	0.512374	26	-5.1

Table A1.2 Nd- and Sr-isotopic ratios for rhyolites and basalts in the BVF. Abbreviations are: CDF – Central Dome Field (China Hat Lava Dome Field) and NDF – North Dome Field. The rhyolite data are initial concentrations corrected using the given Sr and Nd concentrations except for China Cap MM sample for which average Sr and Nd concentrations were used. The basalt values listed are the measured values. Plus or minus values are X 10^{-6}. Time corrections used: 50 ka for CDF and 1.41 Ma for NDF. From Ford (2005).

Appendix 2

This section contains variation diagrams of the synthetic trachybasalt composition of Whitaker et al. (2008) for major oxides vs. wt.% MgO and other variation and mineral phase diagrams with a fO_2 buffers of QFM-2, QFM-1, and QFM to show how they affect mineral phase generation vs. magma temperature and wt.% MgO.

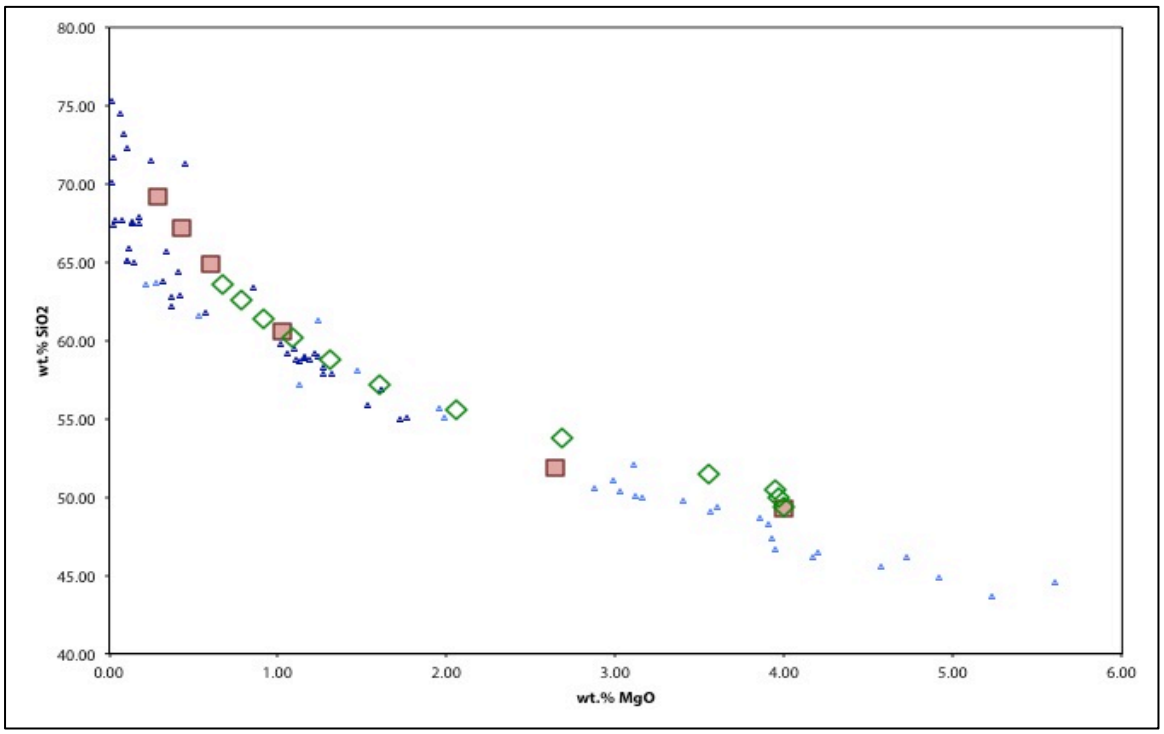

Figure A2.1. Variation diagram of SiO_2 vs. MgO. Symbols are: light blue triangles are COM trend (Kuntz et al., 1992 and Leeman, 1982b); dark blue triangles are Cedar Butte trend (Hayden, 1992 and Spear, 1979); red squares are synthetic trachybasalt experiments (Whitaker et al., 2008); and green diamonds are rhyolite-MELTS equilibrium crystallization (EC) simulation of synthetic trachybasalt experiments of Whitaker et al. (2008). EC simulation tracks with both experimental and analytical data.

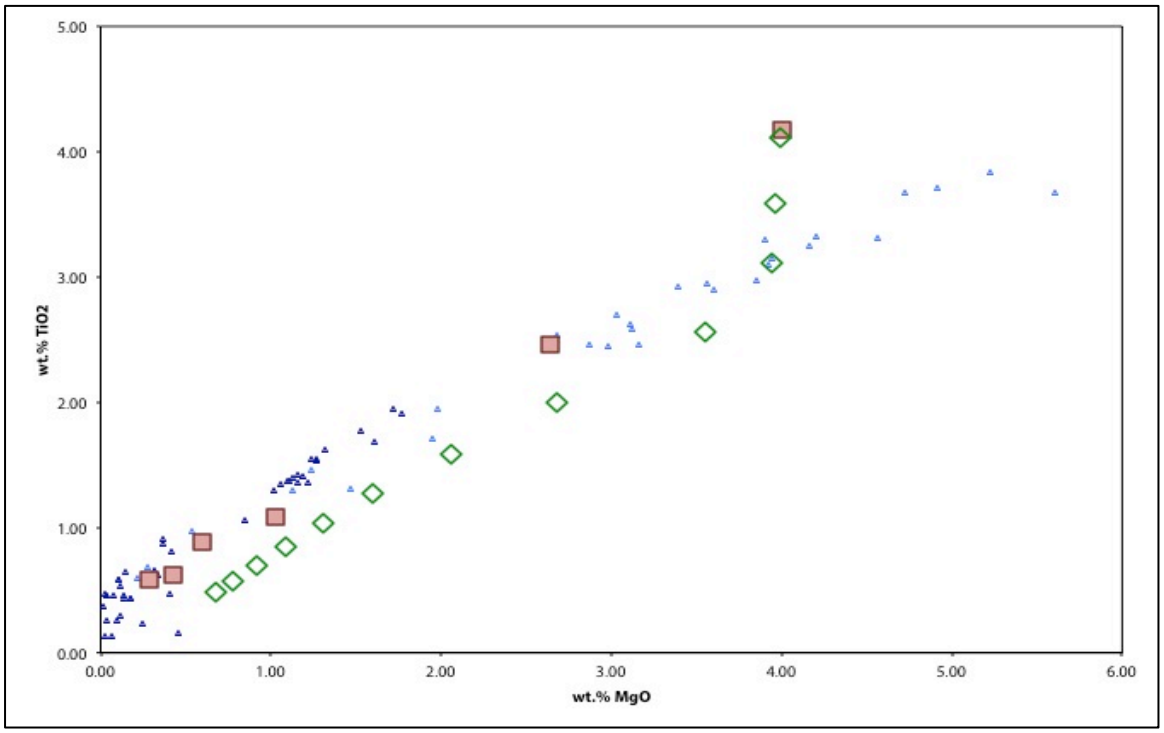

Figure A2.2. Variation diagram of TiO_2 vs. MgO. Symbols are the same as Figure A2.1. EC simulation data is below and parallels experimental and analytical data.

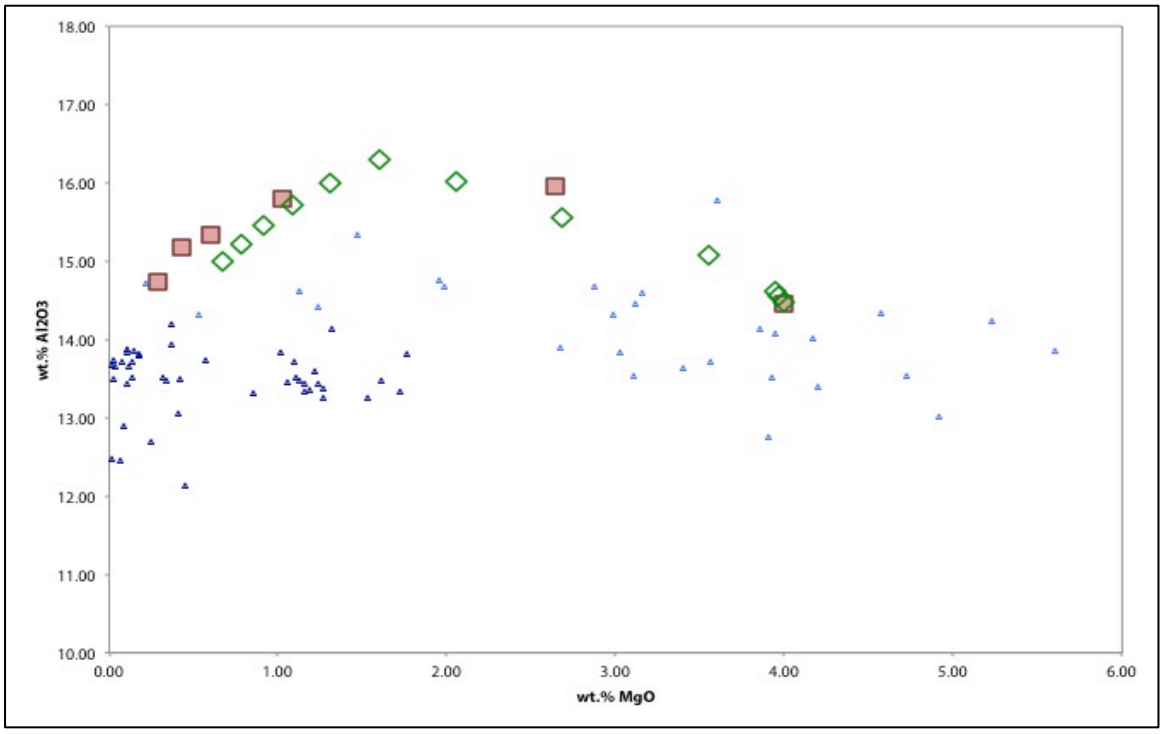

Figure A2.3. Variation diagram of Al_2O_3 vs. MgO. Symbols are the same as Figure A2.1. EC simulation data track experimental data and does not follow analytical data.

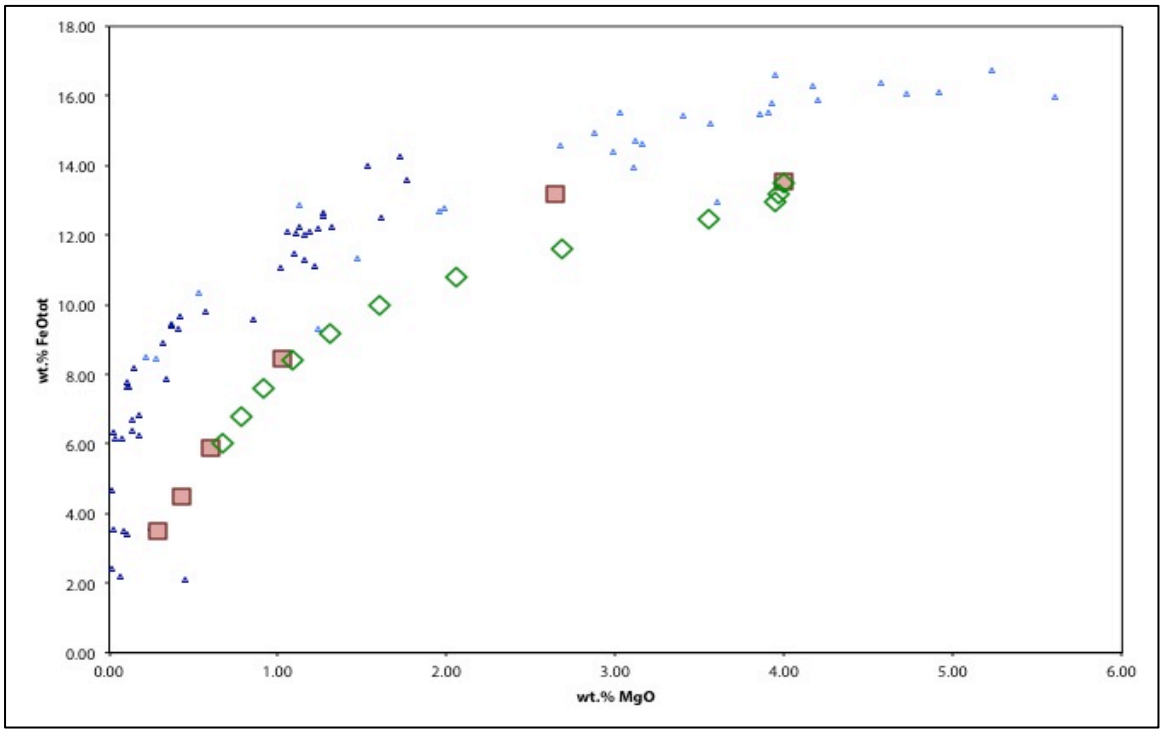

Figure A2.4. Variation diagram of FeO_{tot} vs. MgO. Symbols are the same as Figure A2.1. EC simulation data partially follows experimental data (only when MgO and FeO_{tot} are at low wt.% and is below and parallel to analytical data.

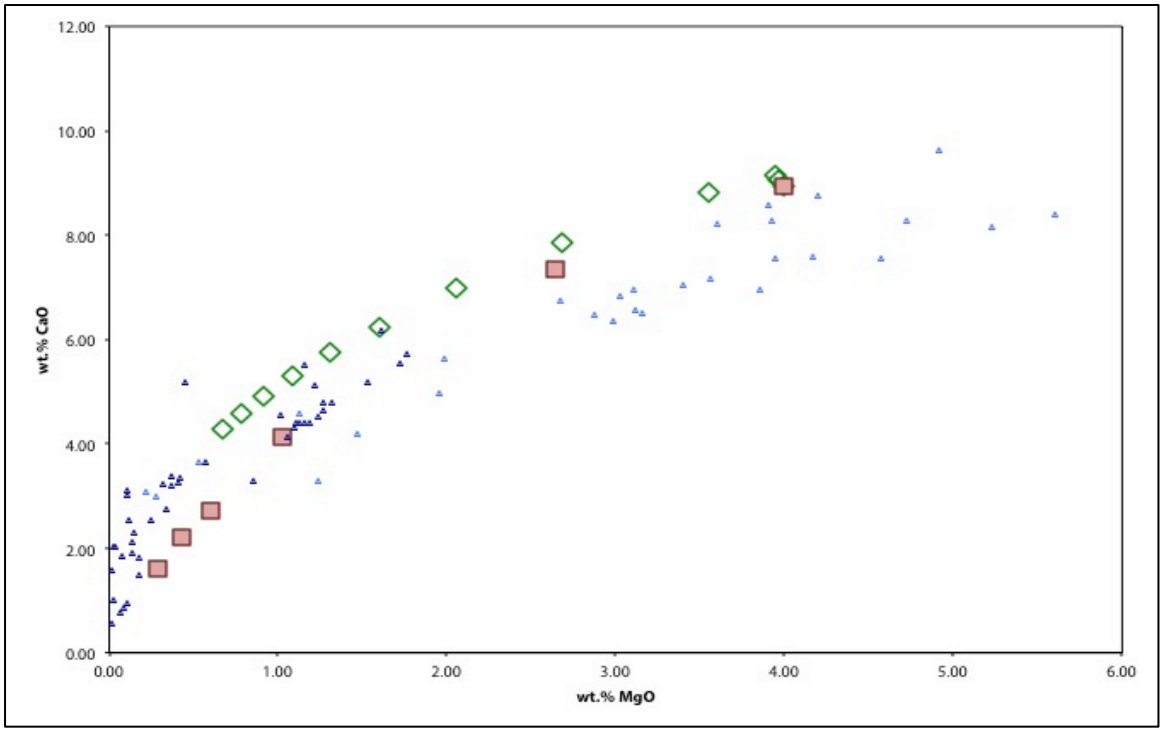

Figure A2.5. Variation diagram of CaO vs. MgO. Symbols are the same as Figure A2.1. EC simulation data is above and parallels experimental and analytical data.

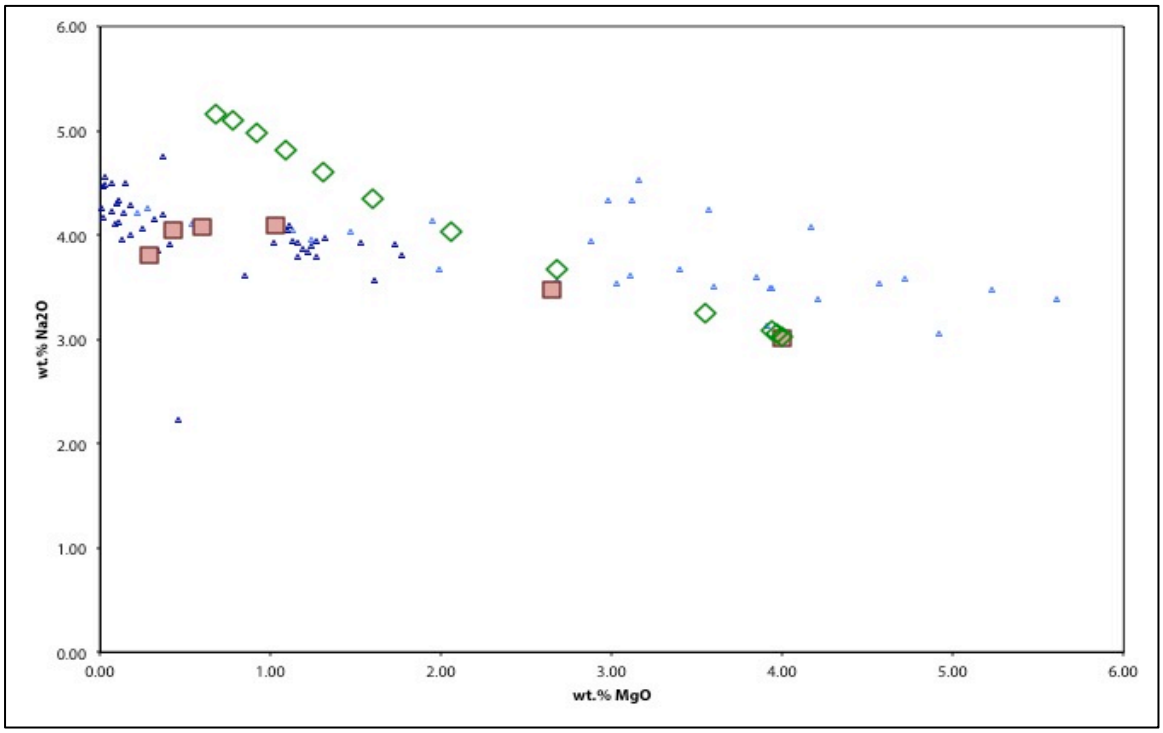

Figure A2.6. Variation diagram of Na_2O vs. MgO. Symbols are the same as Figure A2.1. EC simulation data does not follow experimental or analytical data.

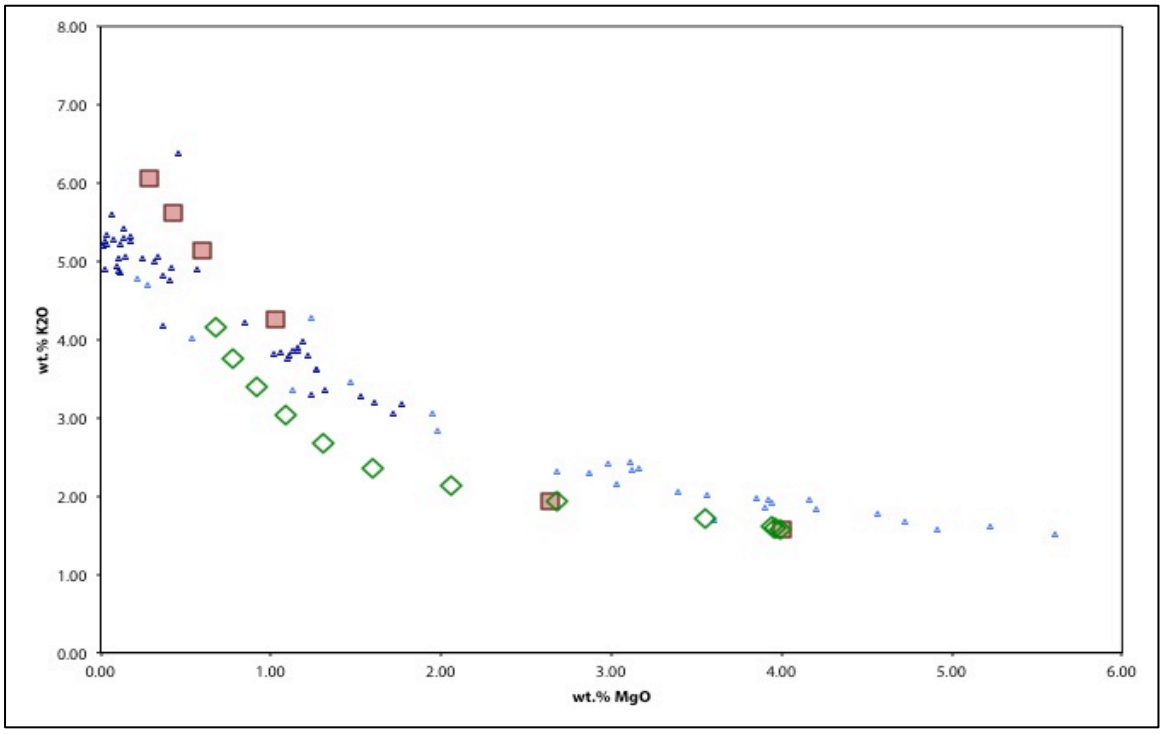

Figure A2.7. Variation diagram of K_2O vs. MgO. Symbols are the same as Figure A2.1. EC simulation data is below and parallel to experimental and analytical data.

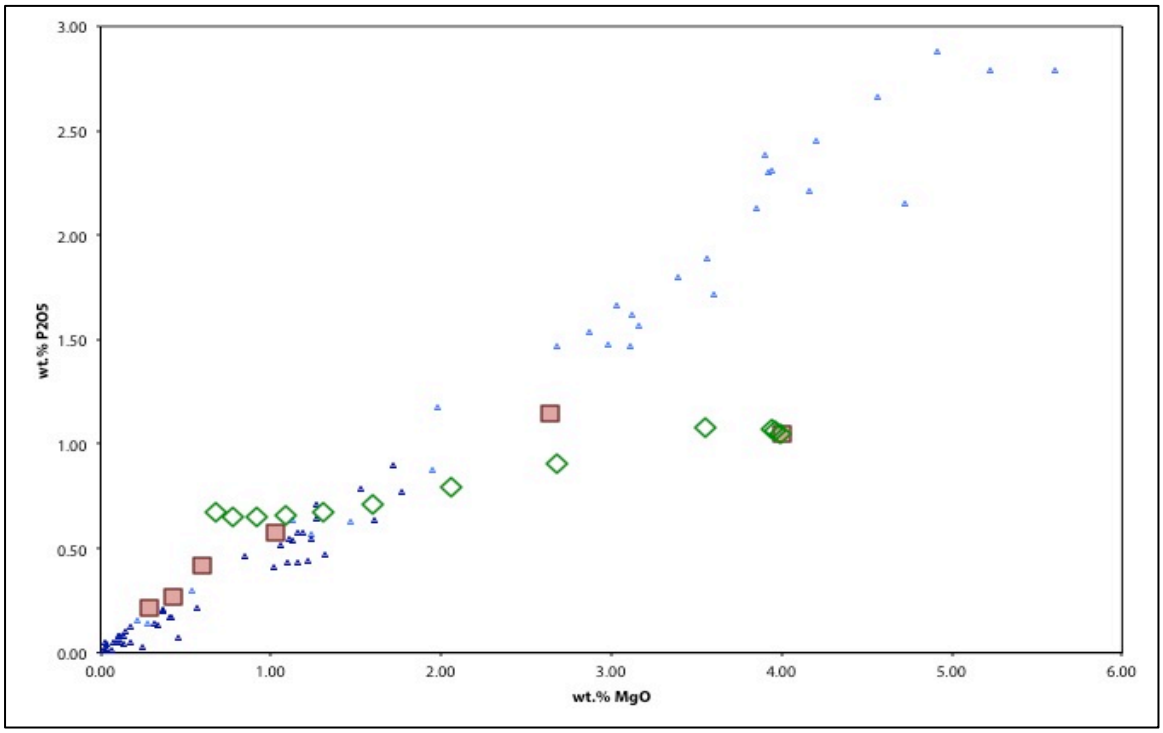

Figure A2.8. Variation diagram of P_2O_5 vs. MgO. Symbols are the same as Figure A2.1. EC simulation data does not follow experimental or analytical data.

Appendix 3

This section contains variation diagrams of the most primitive olivine tholeiite basalt of the Blackfoot Volcanic Field (Pickett, 2004) for major oxides vs. wt.% MgO and other variation and mineral phase diagrams with a fO_2 buffers of QFM only.

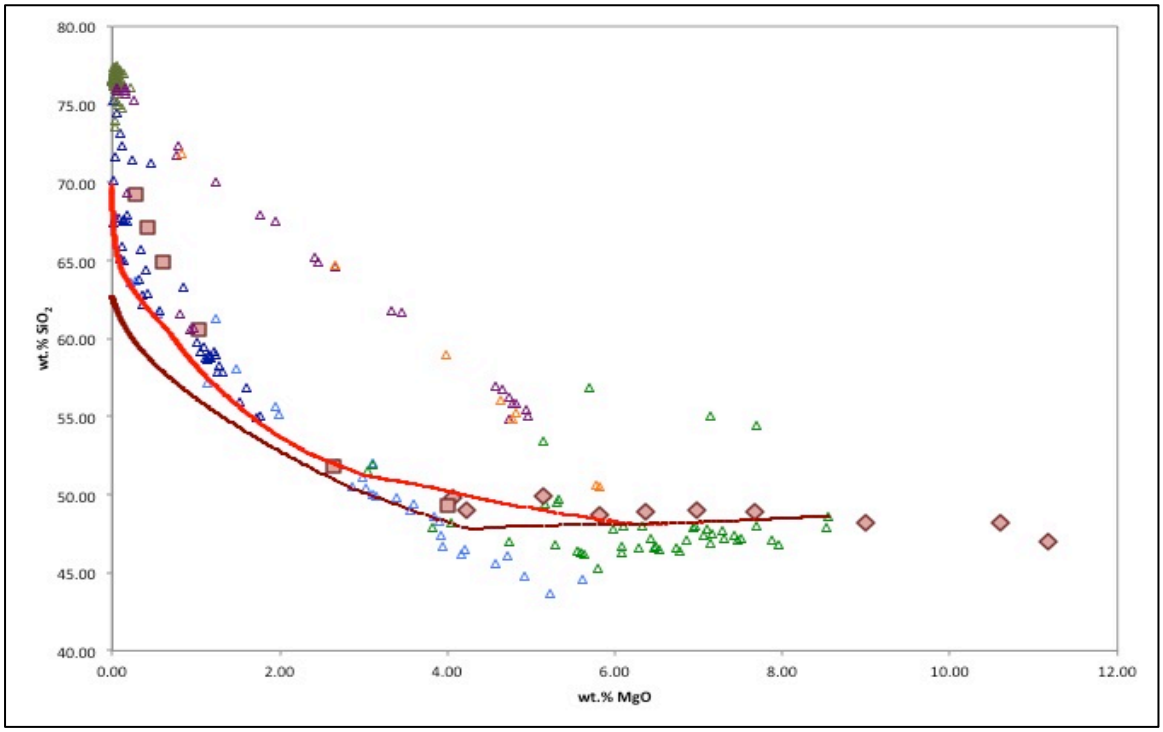

Figure A3.1. Variation diagram of SiO_2 vs. MgO. Symbols are as follows: light blue triangles are COM trend (Kuntz et al., 1992 and Leeman, 1982b); dark blue triangles are Cedar Butte trend (Hayden, 1992 and Spear, 1979); purple triangles are Unnamed Butte trend (Morse, 2002); green triangles are BVF basalts (Pickett, 2004); olive green triangles are BVF rhyolites (Ford, 2005); orange triangles are enclaves in BVF rhyolites (Goldsby et al., 2015); Red diamonds are most primitive olivine tholeiite crystallization experiments of the ESRP (Whitaker et al., 2008); red squares are synthetic trachybasalt crystallization experiments (Whitaker et al., 2008); dark red line is rhyolite-METLS fractional crystallization (FC) simulation of most primitive olivine tholeiite basalt of BVF (Pickett, 2004); and red line is MCS-rhyolite-MELTS assimilation-fractional crystallization (AFC) of the most primitive olivine tholeiite basalt of BVF (Pickett, 2004). FC simulation data is below and parallel to experimental and analytical data. AFC simulation data follows experimental and analytical data.

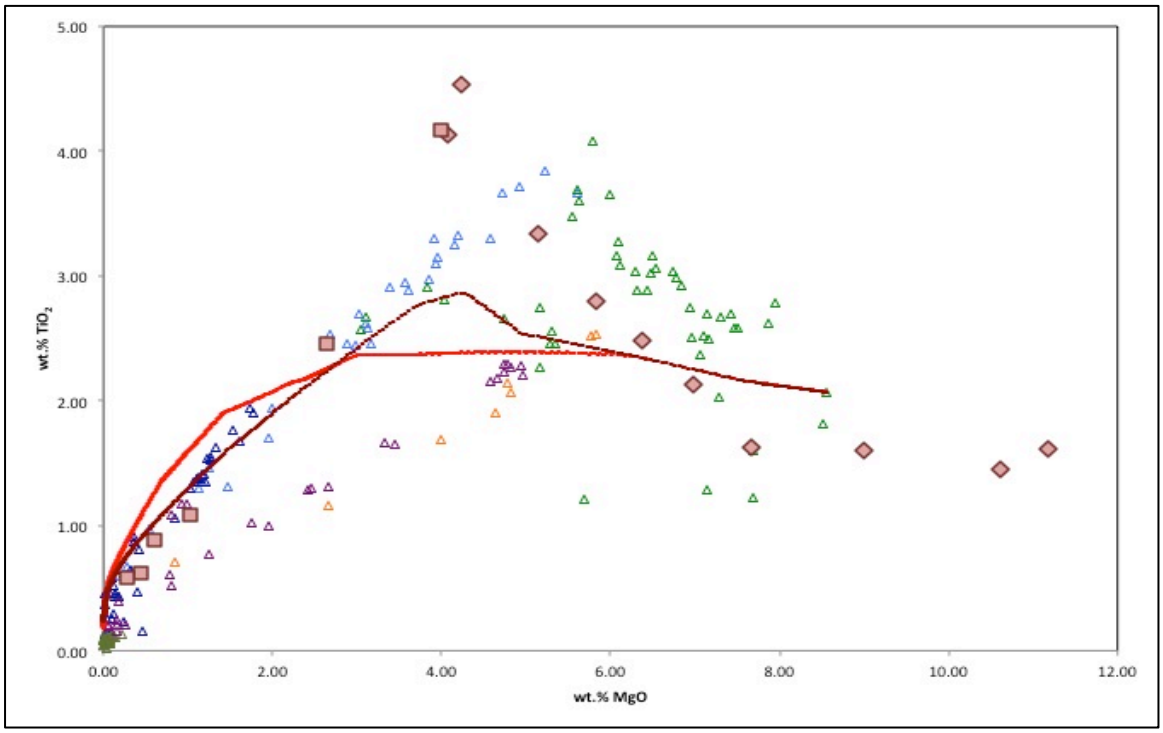

Figure A3.2. Variation diagram of TiO_2 vs. MgO. Symbols are as for Fig. A3.1. FC and AFC simulation data do not follow experimental or analytical data above 4.00 wt.% MgO. FC simulation data and does follow below 4.00 wt.% MgO. AFC simulation data does follow both below ~ 3.00 wt.% MgO.

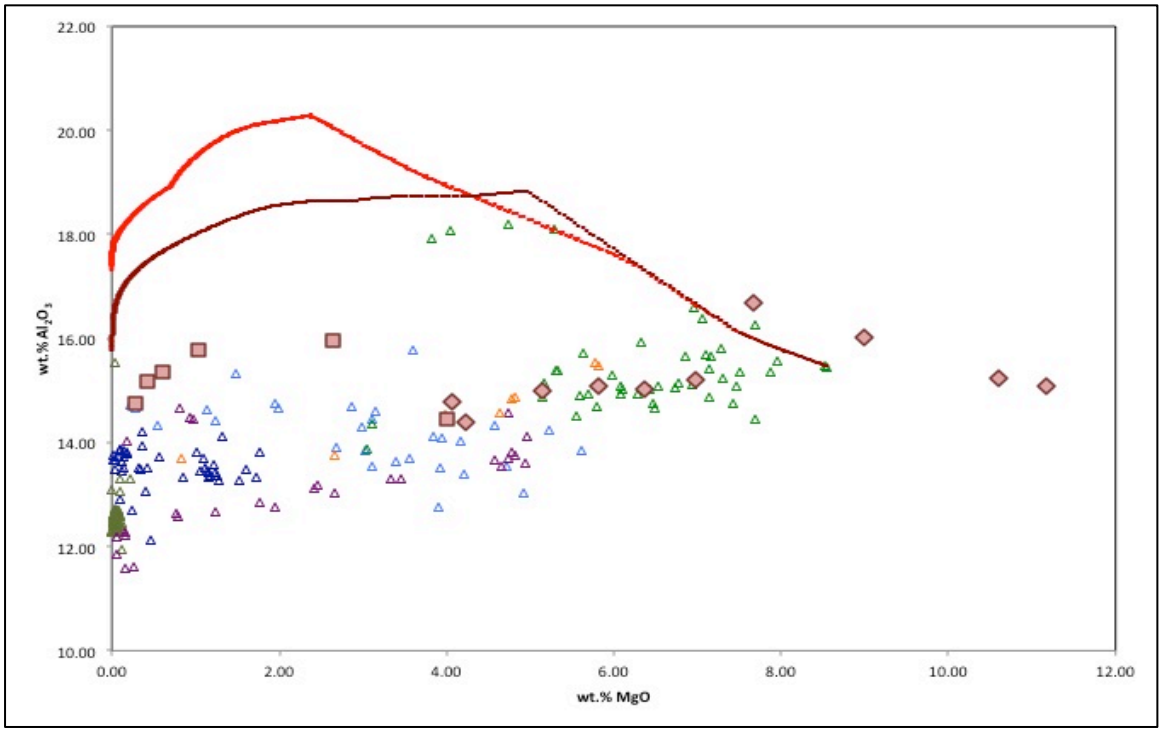

Figure A3.3. Variation diagram of Al_2O_3. Symbols are as for Fig. A3.1. FC and AFC simulation data do not follow experimental or analytical data.

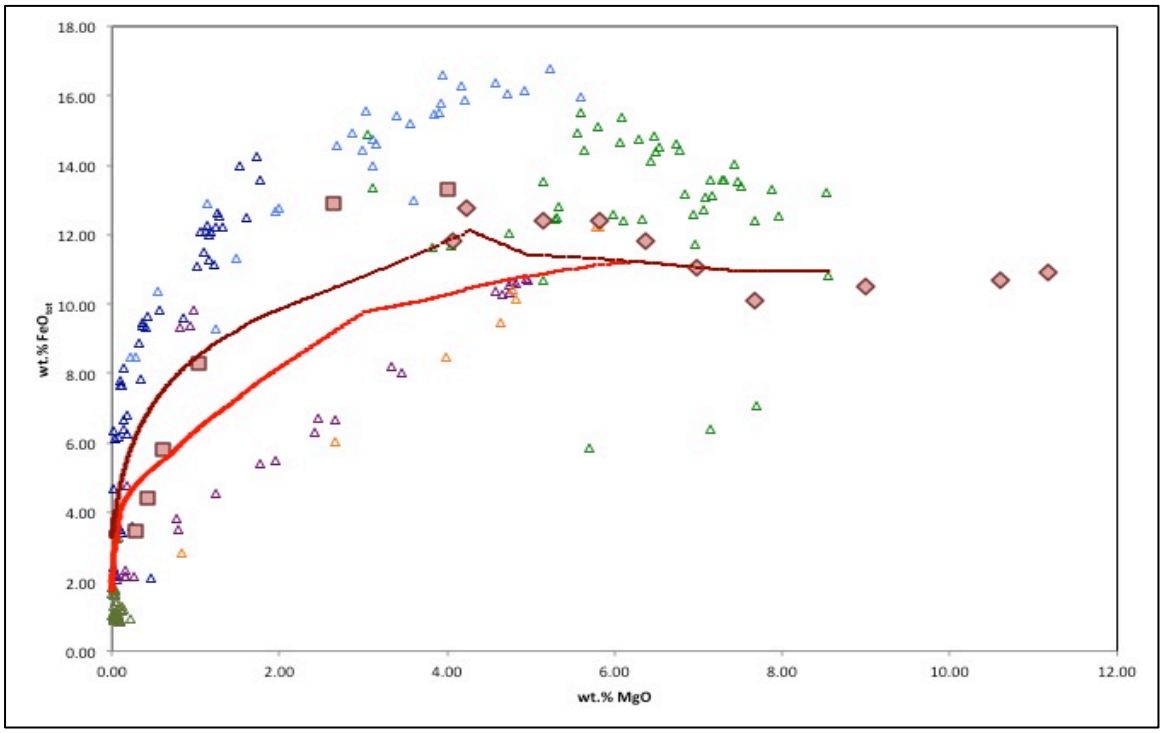

Figure A3.4. Variation diagram of FeO_{tot} vs, MgO. Symbols are as for Fig. A3.1. FC simulation data does not follow experimental and analytical data above ~ 1.00 wt.% MgO bit it does follow experimental and analytical data below ~ 1.00 wt.% MgO. AFC simulation data does not follow experimental or analytical data.

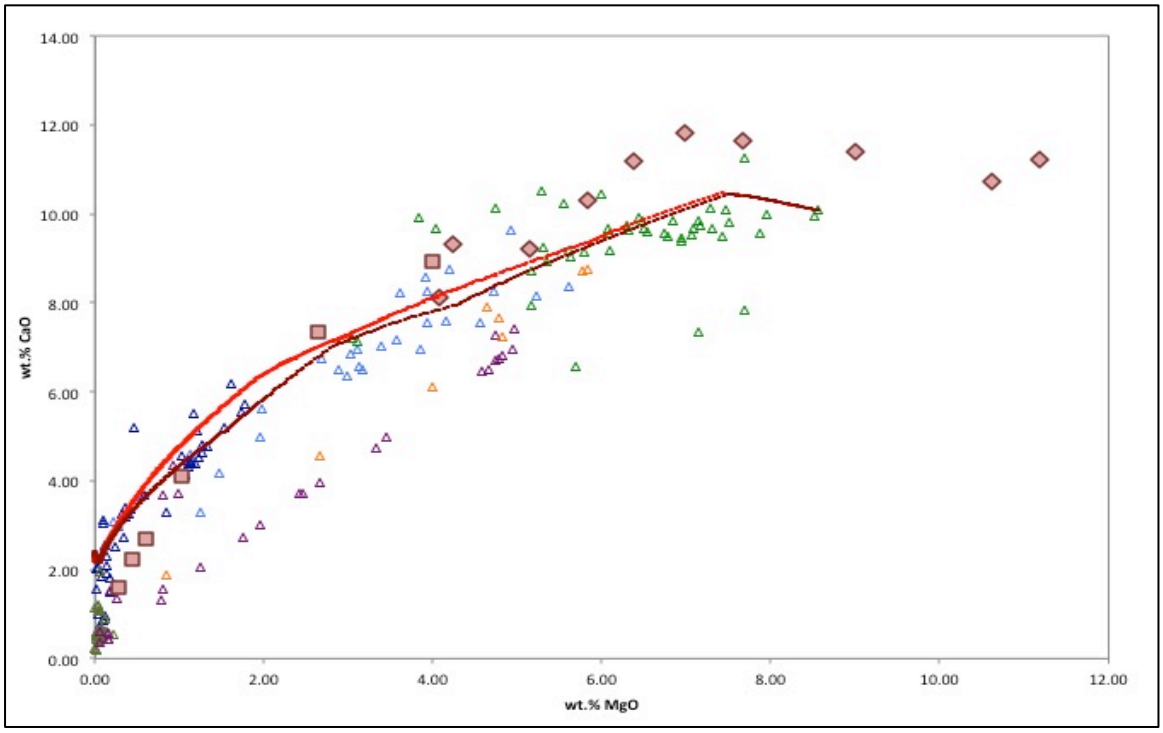

Figure A3.5. Variation diagram of CaO vs. MgO. Symbols are as for Fig. A3.1. FC and AFC simulation data follows experimental and analytical data.

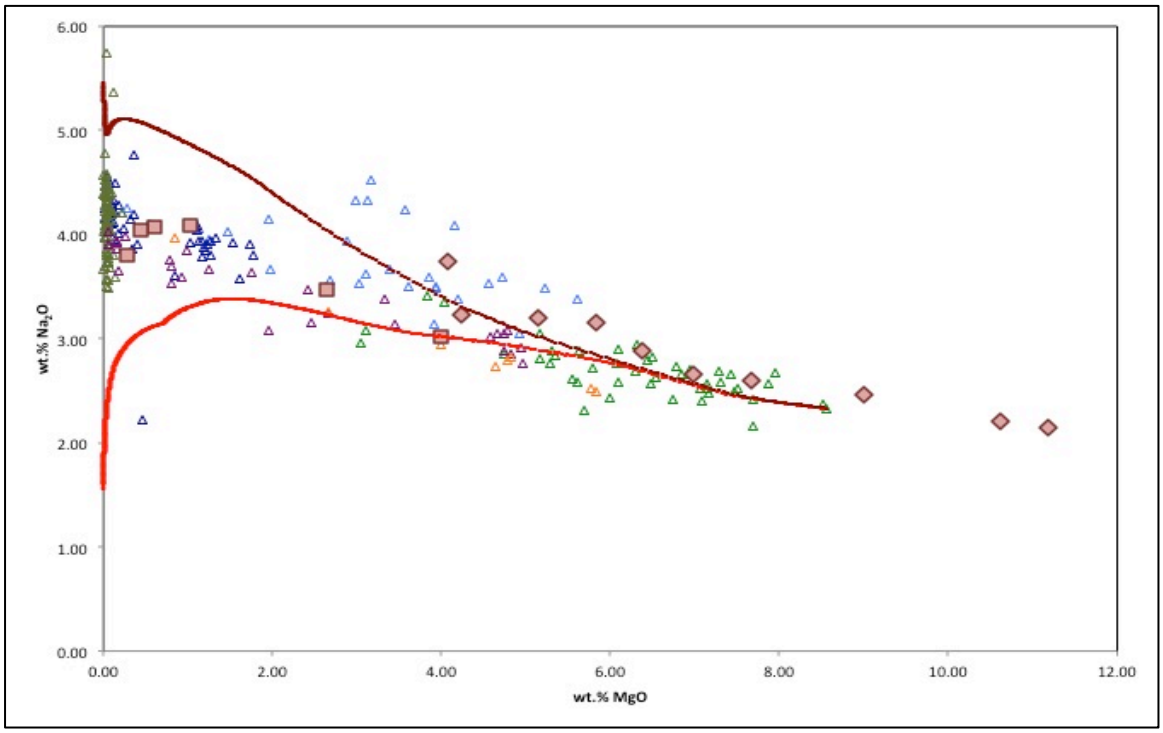

Figure A3.6. Variation diagram of Na_2O vs. MgO. Symbols are as for Fig. A3.1. FC simulation data follows experimental and analytical data above ~ 3.00 wt.% MgO and then tracks above. AFC simulation data follows experimental and analytical data above ~ 2.00 wt.% MgO and then tracks below.

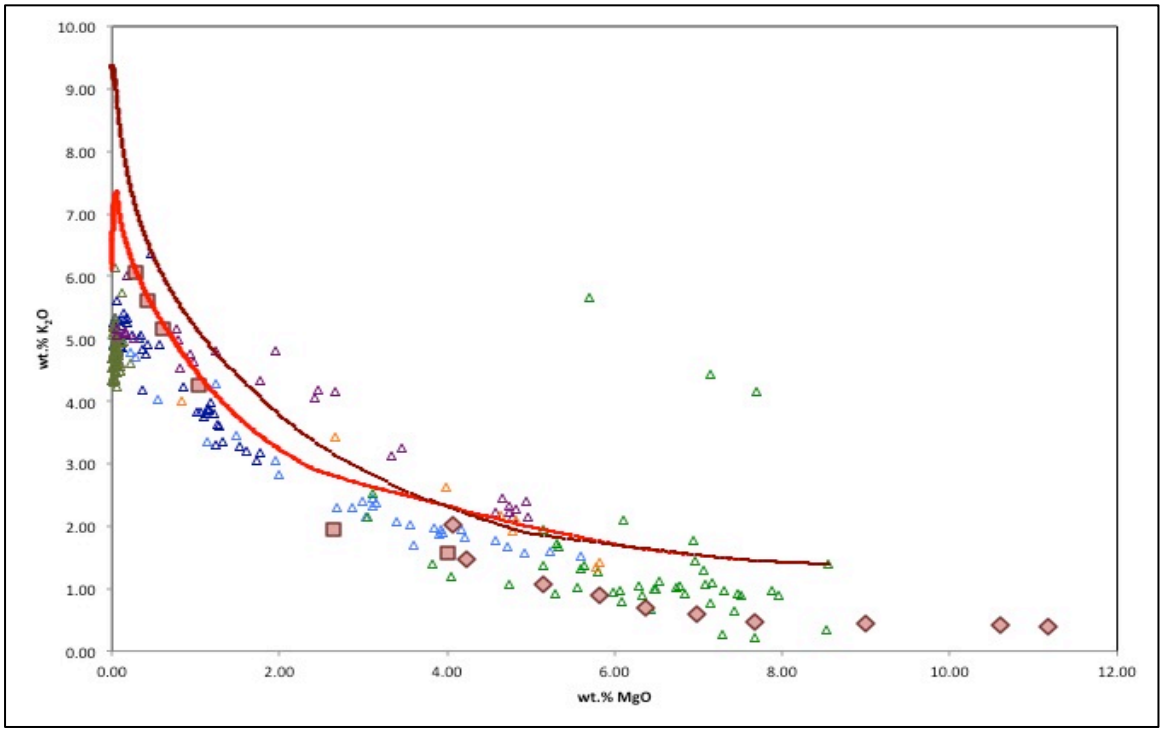

Figure A3.7. Variation diagram of K_2O vs. MgO. Symbols are as for Fig. A3.1. FC and AFC simulation data tracks above experimental and analytical data with AFC data following experimental and analytical data below ~ 1.00 wt.% MgO.

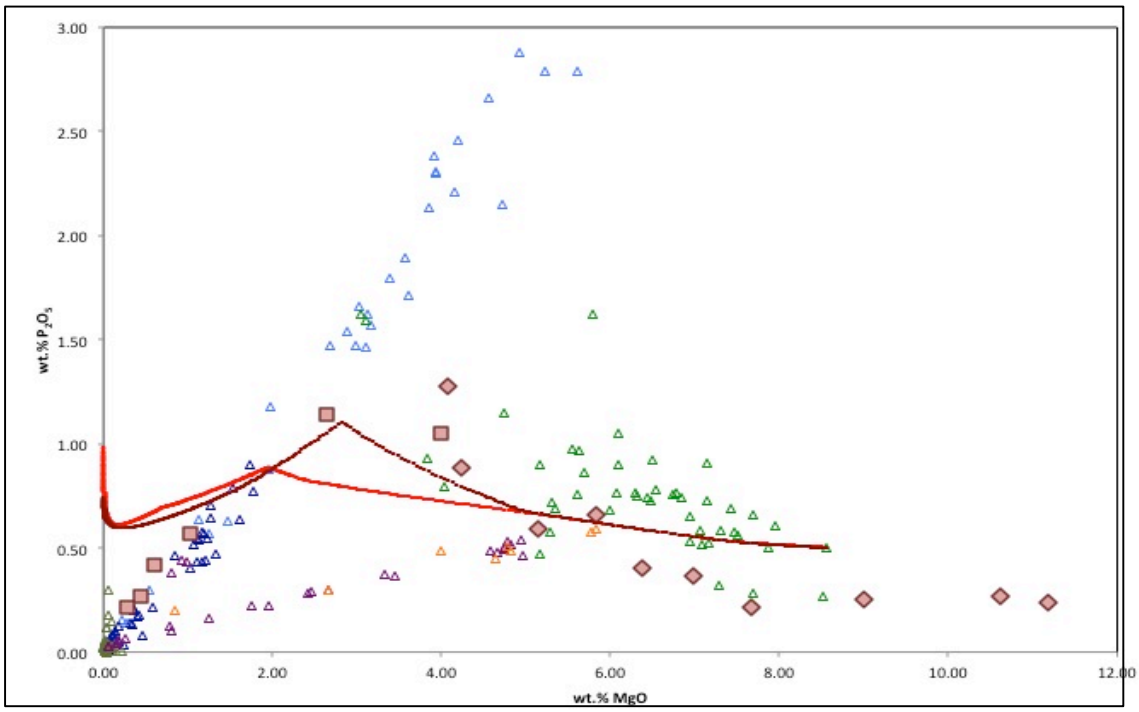

Figure A3.8 Variation diagram of P_2O_5. Symbols are as for Fig. A3.1. FC and AFC simulation data do not follow experimental and analytical data.